Structural insights into sodium-rich silicate - carbonate glasses and melts: A combined study of trace element *in-situ* XAFS and Molecular Dynamics

Julia Pohlenz, M.Sc. Geotechnologie

Dissertation

Universität Potsdam, Mathematisch-Naturwissenschaftlichen Fakultät

Anfertigung der Arbeit:

Helmholtz-Zentrum Potsdam Deutsches GeoForschungsZentrum - GFZ

Wissenschaftsdisziplin Mineralogie

Datum der Disputation: 15.01.2019

Betreuer:
Prof. Dr. M. Wilke, Universität Potsdam

Gutachter:
Prof. Dr. M. Wilke, Universität Potsdam
Prof. Dr. G. Franz, Technische Universität Berlin
Prof. Dr. S. Rossano, Université Paris-Est Marne-la-Vallée

Published online at the
Institutional Repository of the University of Potsdam:
https://doi.org/10.25932/publishup-42382
https://nbn-resolving.org/urn:nbn:de:kobv:517-opus4-423826

Eidesstattliche Erklärung

Hiermit erkläre ich, dass ich die beigefügte Dissertation selbstständig verfasst und keine anderen als die angegebenen Hilfsmittel genutzt habe. Alle wörtlich oder inhaltlich übernommenen Stellen habe ich als solche gekennzeichnet. Ich versichere außerdem, dass ich die beigefügte Dissertation nur in diesem und keinem anderen Promotionsverfahren eingereicht habe und dass diesem Promotionsverfahren kein endgültig gescheitertes Promotionsverfahren vorausgegangen ist.

Berlin, den 28.04.2018
Julia Pohlenz

Daraus hervorgegangene Veröffentlichungen

Pohlenz, J., Pascarelli, S., Mathon, O., Belin, S., Shiryaev, A., Safonov, O., Veligzhanin, A., Murzin, V., Irifune, T., Wilke, M., 2016. Structural properties of sodium-rich carbonate-silicate melts: An *in-situ* high-pressure EXAFS study on Y and Sr. *J. Phys.: Conf. Ser*. 712, 012083.

Pohlenz J., Rosa A.D., Mathon O., Pascarelli S., Belin S., Landrot G., Murzin V., Veligzhanin A., Shiryaev A., Irifune T. & Wilke M., 2018. Structural controls of CO_2 on Y, La and Sr incorporation in sodium-rich silicate – carbonate melts by *in-situ* high P-T EXAFS, *Chemical Geology*, 486, 1-15.

Förderungen

Die vorliegende Studie wurde finanziert durch den Helmholtz Impuls- und Vernetzungsfonds: HRJRG – 404 ("S*tructural properties of carbonate-silicate melts and their effects on partitioning processes in the deep Earth investigated by synchrotron radiation, spectroscopic and ion probe methods"*). Sie wurde weiterhin unterstützt durch ein Kurzstipendiums des Deutschen Akademischen Austauschdienstes DAAD.

Danksagung

Für die Vollendung meiner Promotion möchte ich mich auf das Herzlichste bei Allen bedanken, die mich in der gesamten Zeit tatkräftig und mit gutem Rat unterstützt haben.

Ein besonderes Wort des Dankes möchte ich an meinen Doktorvater richten. Prof. Dr. Max Wilke ermöglichte mir nicht nur die Erarbeitung dieses spannenden Themas, sondern stand mir fortwährend mit Rat und Tat zur Seite und gab mir mit vielen Ideen immer wieder neuen Aufschwung.

Meinen Kollegen am GFZ gilt ein großer Dank, da sie immer ein offenes Ohr für mich hatten und ohne die eine erfolgreiche Durchführung der Arbeit nicht möglich gewesen wäre: Hans Peter Nabein für die wertvolle Hilfe im Chemielabor, Reiner Schulz, Winfried Steiner, Reik Sünkel, Michael Vogt und Andreas Ebert, ohne die niemals die Proben mit der Intern beheizten Gasdruckanlage hergestellt hätten werden können, Dr. Bernd Wunder für die Piston-Zylinder Experimente, Dr. Dieter Rhede und Oona Appelt für die Mikrosondenanalysen, Dr. Sandro Jahn, Dr. Daniela Künzel und Dr. Johannes Wagner, für die Durchführung der Molekular Simulationen und wertevolle Hilfestellungen für deren Auswertung. Letzterem möchte ich besonders für die vielen investierten Stunden des Gegenlesens und fortwährenden Verbesserns des Textes danken.

Danken möchte ich weiterhin Dr. Sakura Pascarelli, Dr. Olivier Mathon, Dr. Angelika Rosa, Dr. Innokenty Kantor, Dr. Mohamed Mezouar, Florian Perrin, Sebastian Pasternak, Dr. Guillaume Morard, Dr. Sylvain Petitgirard, Dr. Stéphanie Belin, Dr. Gautier Landrot, Dr. Vadim Murzin, Dr. Alexey Veligzhanin, Dr. Andrei Shiryaev für die Unterstützung der Röntgenabsorptionsmessungen an der European Radiation Synchrotron Facility, Frankreich und des Synchrotron Soleil, Frankreich sowie Prof. Dr. Harald Behrens und Dr. Stephan Schuth für die ermöglichten Volatilmessungen an der Leibniz Universität Hannover.

Mein ganz besonderer Dank gilt Prof. Dr. Monika Koch-Müller sowie Prof. Dr. Gerhard Franz, die mich bereits während des Bachelorstudiums intensiv förderten und mir die Welt der Mineralogie eröffneten.

Tief verbunden bin ich meiner Familie und lieben Freunden, die während der gesamten Arbeit an meiner Seite standen. Insbesondere möchte ich meinem Großvater Manfred Liebscher danken, der mir mit seiner Begeisterung für die Geowissenschaften immer einen besonderen Ansporn verlieh und dem ich diese Arbeit widme.

Kurzfassung

Karbonatische und karbonatreiche silikatische Schmelzen spielen eine entscheidende Rolle in den magmatischen Prozessen der Erde. Die interne Schmelzstruktur bestimmt dabei maßgeblich ihre physikalischen und chemischen Eigenschaften. Karbonatreiche Schmelzen können sehr stark mit geochemisch wichtigen Spurenelementen angereichert sein. Die strukturellen Einbaumechanismen sind jedoch kaum verstanden, da diese Schmelzen nicht zu homogenen Gläsern abgeschreckt werden können, welche üblicherweise für strukturelle Untersuchungen genutzt werden. Die vorliegende Arbeit widmet sich dem Einfluss von CO_2 auf die lokale Umgebung von ausgewählten Spurenelementen in karbonathaltigen silikatischen Gläsern sowie silikatisch bis karbonatischen Schmelzen. Untersucht werden natriumreiche, stark bis extrem peralkaline silikatische und karbonatische Zusammensetzungen, wie sie vom Vulkan Oldoinyo Lengai, Tansania, bekannt sind.

Zum einen werden die lokale Umgebungen von Yttrium (Y), Lanthan (La) und Strontium (Sr) in synthetisierten Gläsern und Schmelzen mit Röntgen-Absorption-Feinstruktur-Spektroskopie (engl. X-ray absorption fine structure (XAFS) spectroscopy) untersucht. Insbesondere extended X-ray absorption fine structure (EXAFS) spectroscopy liefert elementspezifisch strukturelle Informationen über Bindungslängen, Koordinationszahlen und Ordnungsgrad. Dem hohen Grad struktureller Unordnung in Gläsern und Schmelzen wird in den vorliegenden EXAFS-Analysen mit der Verwendung einer asymmetrischen Verteilungsfunktion und eines Korrelationsmodells, basierend auf der Bindungsvalenztheorie, Rechnung getragen. Für silikatische Gläser mit steigendem CO_2-Gehalt zwischen 0 und bis zu 7,6 Gew.-% ist festzustellen: (1) Konstante Bindungslängen für Sr-O (~ 2,55 Å) und La-O (~ 2,54 Å) in extrem peralkaliner Zusammensetzung, sowie für Y-O (~ 2,29 Å) in stark und extrem peralkaliner Zusammensetzung. (2) Zunehmende Bindungslängen für Sr-O (~ von 2,53 auf 2,57 Å) und La-O in stark peralkaliner Zusammensetzung (~ von 2,52 auf 2,54 Å). Weiterhin werden silikatische sowie nicht-abschreckbare karbonatische Schmelzen *in-situ* unter hohem Druck und hoher Temperatur (2,2 bis 2,6 GPa, 1200 bis 1500 °C, untersucht in einer Paris-Edinburgh-Presse) analysiert. Ein neu entwickelter Aufbau des Druckübertragungsmediums garantiert eine hohe mechanische Festigkeit und ermöglicht aufgrund hervorragender Transmissivität im relevanten Energiebereich Transmissions-EXAFS an niedrigkonzentrierten Elementen. Im Vergleich zu den Gläsern zeigen die Schmelzen generell ~ 3 % höhere Y-O-, La-O-, und Sr-O-Bindungslängen und

eine erhöhte Asymmetrie in der Paarverteilung. In silikatischen Schmelzen sind Y-O-Bindungs-längen konstant (~ 2,37 Å), wohingegen sie in karbonatischen Schmelzen zunehmen (bis zu 2,41 Å). La-O-Abstände vergrößern sich systematisch von silikatischen zu karbonatischen Schmelzen (von 2,55 auf 2,60 Å). Sr-O-Abstände steigen von 2,60 auf 2,64 Å in silikatischen Zusammensetzungen mit steigendem CO_2-Gehalt und sind für alle karbonatischen Zusammensetzungen konstant.

Zum Vergleich und besserem Verständnis wurden Y- und Sr-haltige, silikatische und karbonatische Glas- und Schmelzstrukturen in einer explorativen *ab initio* Molekular Dynamik (MD) Studie simuliert. Die MD-Studie bestätigt die CO_2-abhängigen lokalen Veränderungen um Y und Sr und liefert zusätzliche Einblicke in silikatische und karbonatische Glas- und Schmelzstrukturen. In natrium-reicher silikatischer Zusammensetzung wird CO_2 hauptsächlich als freie Karbonatgruppe eingebaut oder teilt sich als nicht-brückenbildendes Karbonat genau ein Sauerstoffatom mit einem Netzwerkbildner (Si oder $^{[4]}$Al). Seltener tritt es als brückenbildendes Karbonat zwischen zwei Netzwerkbildnern auf; dabei allerdings mit einer gegenüber der statistischen Verteilung deutlich erhöhten Präferenz für zwei $^{[4]}$Al als anliegende Netzwerkbildner. C-haltige Schmelzen weisen geringe Mengen an molekularem CO_2 auf, welches in den abgeschreckten Gläsern fast vollständig als Karbonat gelöst ist.

Die Kombination aus Experiment und Simulation gewährt außerordentliche Einblicke in nur schwierig zu untersuchende Glas- und Schmelzstrukturen. Die gewonnenen Daten werden auf Grundlage der Bindungsvalenztheorie gedeutet und hinsichtlich potentieller Mechanismen des strukturellen Spurenelementeinbaus sowie dem daraus ableitbaren Fraktionierungsverhalten in natürlichen Schmelzen diskutiert. Neue Erkenntnisse über den strukturellen CO_2-Einbau werden genutzt, um ein Strukturmodell für karbonatische Schmelzen abzuleiten. Dieses basiert auf der Verknüpfung von 7- bis 9-fach koordinierten Kationenpolyedern durch die planaren Karbonat-Gruppen, ähnlich wie es im Na-Ca-Karbonat Nyerereite zu beobachten ist. Letztendlich leisten die Erkenntnisse der Arbeit somit ihren Beitrag, das Verständnis um die einzigartigen physikalischen Eigenschaften und geologischen Phänomene dieser Schmelzen zu vertiefen.

Abstract

Carbonate-rich silicate and carbonate melts play a crucial role in deep Earth magmatic processes and their melt structure is a key parameter, as it controls physical and chemical properties. Carbonate-rich melts can be strongly enriched in geochemically important trace elements. The structural incorporation mechanisms of these elements are difficult to study because such melts generally cannot be quenched to glasses, which are usually employed for structural investigations. This thesis investigates the influence of CO_2 on the local environments of trace elements contained in silicate glasses with variable CO_2 concentrations as well as in silicate and carbonate melts. The compositions studied include sodium-rich peralkaline silicate melts and glasses and carbonate melts similar to those occurring naturally at Oldoinyo Lengai volcano, Tanzania.

The local environments of the three elements yttrium (Y), lanthanum (La) and strontium (Sr) were investigated in synthesized glasses and melts using X-ray absorption fine structure (XAFS) spectroscopy. Especially extended X-ray absorption fine structure spectroscopy (EXAFS) provides element specific information on local structure, such as bond lengths, coordination numbers and the degree of disorder. To cope with the enhanced structural disorder present in glasses and melts, EXAFS analysis was based on fitting approaches using an asymmetric distribution function as well as a correlation model according to bond valence theory. Firstly, silicate glasses quenched from high pressure/temperature melts with up to 7.6 wt % CO_2 were investigated. In strongly and extremely peralkaline glasses the local structure of Y is unaffected by the CO_2 content (with oxygen bond lengths of ~ 2.29 Å). Contrary, the bond lengths for Sr-O and La-O increase with increasing CO_2 content in the strongly peralkaline glasses from ~ 2.53 to ~ 2.57 Å and from ~ 2.52 to ~ 2.54 Å, respectively, while they remain constant in extremely peralkaline glasses (at ~ 2.55 Å and 2.54 Å, respectively). Furthermore, silicate and unquenchable carbonate melts were investigated *in-situ* at high pressure/temperature conditions (2.2 to 2.6 GPa, 1200 to 1500 °C) using a Paris-Edinburgh press. A novel design of the pressure medium assembly for this press was developed, which features increased mechanical stability as well as enhanced transmittance at relevant energies to allow for low content element EXAFS in transmission. Compared to glasses the bond lengths of Y-O, La-O and Sr-O are elongated by up to + 3 % in the melt and exhibit higher asymmetric pair distributions. For all investigated silicate melt compositions Y-O bond lengths were found constant at ~ 2.37 Å,

while in the carbonate melt the Y-O length increases slightly to 2.41 Å. The La-O bond lengths in turn, increase systematically over the whole silicate – carbonate melt joint from 2.55 to 2.60 Å. Sr-O bond lengths in melts increase from ~ 2.60 to 2.64 Å from pure silicate to silicate-bearing carbonate composition with constant elevated bond length within the carbonate region.

For comparison and deeper insight, glass and melt structures of Y and Sr bearing sodium-rich silicate to carbonate compositions were simulated in an explorative *ab initio* molecular dynamics (MD) study. The simulations confirm observed patterns of CO_2-dependent local changes around Y and Sr and additionally provide further insights into detailed incorporation mechanisms of the trace elements and CO_2. Principle findings include that in sodium-rich silicate compositions carbon either is mainly incorporated as a free carbonate-group or shares one oxygen with a network former (Si or $^{[4]}$Al) to form a non-bridging carbonate. Of minor importance are bridging carbonates between two network formers. Here, a clear preference for two $^{[4]}$Al as adjacent network formers occurs, compared to what a statistical distribution would suggest. In C-bearing silicate melts minor amounts of molecular CO_2 are present, which is almost totally dissolved as carbonate in the quenched glasses.

The combination of experiment and simulation provides extraordinary insights into glass and melt structures. The new data is interpreted on the basis of bond valence theory and is used to deduce potential mechanisms for structural incorporation of investigated elements, which allow for prediction on their partitioning behavior in natural melts. Furthermore, it provides unique insights into the dissolution mechanisms of CO_2 in silicate melts and into the carbonate melt structure. For the latter, a structural model is suggested, which is based on planar CO_3-groups linking 7- to 9-fold cation polyhedra, in accordance to structural units as found in the Na-Ca carbonate nyerereite. Ultimately, the outcome of this study contributes to rationalize the unique physical properties and geological phenomena related to carbonated silicate-carbonate melts.

List of Content

List of Figures

List of Tables

List of Abbreviations

$^{[4]}Al–CO_3$	non-bridging carbonate associated with $^{[4]}Al$
$^{[4]}Al–CO_3–^{[4]}Al$	bridging carbonate between two $^{[4]}Al$ cations
ASI	aluminum saturation index
BE	boron epoxy
BO	bridging oxygen
BO_{Al-Al}	bridging oxygen between two $^{[4]}Al$ cations
BO_{Si-Al}	bridging oxygen between one Si and one $^{[4]}Al$ cation
BO_{Si-Si}	bridging oxygen between two Si cations
CAR	carbonate sample composition
E	energy
EMPA	electron microprobe analysis
ESRF	European synchrotron radiation facility
EXAFS	extended X-ray absorption fine structure
FC	free carbonate
FO	free oxygen, not bound to any network former
FT	Fourier transform
FWHM	full width half maximum
g(R)	pair distribution function (normalized)
hBN	hexagonal boron nitride
h	asymmetry parameter
HP	high pressure
HPHT	high pressure, high temperature
HT	high temperature
k	wave number
μ(E)	X-ray absorption signal
M	Metal cation
MD	molecular dynamic
N	coordination number
NBO	non-bridging oxygen
NBO_{Al}	non-bridging oxygen associated with $^{[4]}Al$
NBO_{Si}	non-bridging oxygen associated with Si
NMR	nuclear magnetic resonance

p(R)	pair distribution function
$\mathbb{P}_{heat}$	heating Power
P_{oil}	oil pressure
P_{sample}	sample pressure
PDF	pair distribution function
PEEK	polyether ether ketone
R	mean bond length (determined in EXAFS)
$\bar{r}$	average bond length derived from molecular dynamic simulations
$\hat{r}$	most probable bond length derived from molecular dynamic simulations
s	bond strength, bond valence
s_f	field strength
σ^2	Debye-Waller factor
Si–CO_3	non-bridging carbonate associated with Si
Si–CO_3–$^{[4]}$Al	bridging carbonate between one Si and one $^{[4]}$Al
Si–CO_3–Si	bridging carbonate between two Si cations
sNC	Na-Ca-rich silicate composition, extremely peralkaline
sSA	Si-Al-rich silicate composition, strongly peralkaline
T	tetrahedra
T_{sample}	sample temperature
T–CO_3	non-bridging carbonate associated with a bridging oxygen
T–CO_3–T	bridging carbonate
$^{T}_{T}\!-\!CO_3$	non-bridging carbonate associated with a bridging oxygen
$^{T}_{T}\!=\!CO_3$	non-bridging carbonate sharing 2 oxygens with one Si or $^{[4]}$Al, of which one is an BO and one an NBO
$^{T}_{T}\!-\!CO_3^{-T}$	tri-cluster carbonate group (bridging 3 network formers)
TO	tri-cluster oxygen
WC	tungsten carbide
χ(E)	EXAFS fine-structure function
XAFS	X-ray absorption fine structure
XANES	X-ray absorption near edge structure
XRD	X-ray diffraction

1 Introduction

1.1 Motivation and aim of the study

Carbon (C) is of extraordinary significance for human life on Earth: besides its numerous technological applications (Pierson, 2012), its compounds build the basis for all known life forms (Pace, 2001) and it plays a major role in creating a habitable environment on Earth (Kasting and Catling, 2003). Thus, carbon has attracted much attention from the scientific community and the global carbon cycle has been intensively investigated regarding the element's interaction between atmosphere, hydrosphere, biosphere and near surface reservoirs (e.g. Barker et al., 2003; Post et al., 1990; Schimel, 1995). In recent years, the focus also shifted towards carbon in the deep Earth (Dasgupta and Hirschmann, 2010; Hazen et al., 2012; Zhang and Zindler, 1993). While carbon-bearing seafloor sediments are subducted at continental margins (Seto et al., 2008), magmas generated in the upper mantle likewise transport deep-Earth carbon back to the surface. In the form of CO_2 or carbonate, it is the second most abundant volatile component in magmatic systems after water (Carroll and Holloway, 1994). Enrichment in carbon gives rise to carbonatite melts and will produce carbonatite rocks, which bear more than 50 mol % of carbonate minerals (Le Maitre et al., 2005). Carbonatite melts show extremely low densities and viscosities, are highly mobile in mantle and crust and are able to incorporate a wide range of trace elements and other volatiles in unusually high concentrations (Dobson et al., 1996). This makes them excellent metasomatizing agents (Grégoire et al., 2000; Kamenetsky et al., 2004) and carbonate metasomatism has been proposed to play a crucial role in diamond formation (Pal'yanov et al., 1999). By lowering liquidus temperatures of silicate melts (Sifré et al., 2014), carbon also plays a key role in deep magma generation (Dasgupta et al., 2007). Carbonatite melts possess the lowest melting temperatures known in geological systems. In the case of the volcano Oldoinyo Lengai in Tanzania (Jones et al., 2013) the melting temperature decreases down to 600 °C due to the hydrous nature of the melt (De Moor et al., 2013). It is the only active carbonatite volcano on Earth (Bell and Keller, 1995). Its sodium-rich lavas are unique and crystallize to silicate rocks (phonolites and nephelinites) or natrocarbonatites. Generally, carbonatites have the potential to be strongly enriched in certain trace elements, such as the tech-

nologically important rare earth elements (Mariano, 1989). To understand carbonate-related deep Earth processes (Hazen et al., 2013) as well as the macroscopic properties of carbonate-rich silicate and carbonate melts, a thorough understanding of the molecular structure of such melts is essential (Mysen, 1990).

Due to their fundamentally different structural characteristics, silicate and carbonate melts are immiscible at low pressure conditions (< 3 GPa), but may form homogeneous liquids at higher pressures (e.g. Brooker and Kjarsgaard, 2011; Lee and Wyllie, 1996). Thus, the role of liquid immiscibility as a consequence of decompression during magma ascent has been intensively discussed in the context of natrocarbonatite genesis, next to fractional crystallization or partial melting (Jones et al., 2013). The conjugate silicate and carbonate liquids show a strong fractionation of trace elements (Jones et al., 1995; Martin et al., 2013, 2012; Wendlandt and Harrison, 1979). Veksler et al. (1998, 2012) investigated the partitioning of several important trace elements in sodium-rich melts, representing a simplified bulk compositions of the sodium-rich silicate (Klaudius and Keller, 2006; Peterson, 1989) and carbonate rocks (Peterson, 1990) from the Oldoinyo Lengai. Of all investigated elements, Veksler et al. (1998) found only three that were enriched in the carbonate melt: Ba, Sr and La (in decreasing compatibility). The remaining rare earth elements as well as all high-field strength elements partitioned into the peralkaline silicate melt.

To further our understanding of the role carbonate and carbonatite melt structure play in element fractionation, a more systematic approach is necessary. The present study aims to unravel the structural incorporation of Y, La and Sr (representing heavy and light rare earth elements and alkaline earths, respectively) into glasses and melts of various compositions in the system SiO_2-Al_2O_3-Na_2O-CaO-CO_2, addressing particularly the role of increasing CO_2-content. To track down CO_2-dependent structural changes in these systems, a combination of laboratory and computer based experiments is chosen. X-ray absorption fine structure (XAFS) spectroscopy allows to element-specifically analyze the local structure in disordered materials; even at high pressure (*HP*) and high temperature (*HT*), if combined with a large volume press (Paris-Edinburgh-press). Results are interpreted taking into account complementary insights from computational molecular dynamics (MD) simulations. Ultimately, derived information

about the local structure of trace elements will help developing models of trace element partitioning, which is used as a versatile tool to enlighten geological processes (Green, 1994; Irving, 1978; McIntire, 1963). Local structural information will eventually build the basis for a comprehensive model of the structure of carbonate-silicate melts.

On that account, chapter 1.2 provides an overview about general structural models of silicate and carbonate melts and glasses. Detailed information on the applied experimental procedures is found in chapter 2: Firstly, the large volume Paris-Edinburgh press is presented in chapter 2.1. Secondly, methods used for sample preparation and chemical characterization are outlined in chapter 2.2. The structure sensitive methods of XAFS analysis, focusing on extended X-ray absorption fine structure (EXAFS) spectroscopy, and MD simulations are explained and their application explicated in chapters 2.3 and 2.4, respectively. Chapter 3 presents the derived results, which are discussed in chapter 4. Ultimately, chapter 5 summarizes the study's outcome in the context of the current geoscientific debate and provides an outlook of future research potential building up onto results drawn from this study.

1.2 Structure of silicate and carbonate glasses and melts

Unlike crystals, which are defined by long-range structural periodicity and symmetry, melts only possess short-range to medium-range order (Brown et al., 1995). Short-range order can be defined as structural order within ~ 1.6 to 3 Å radius around a central atom and is manifested as cation-oxygen polyhedra. Such polyhedra are defined by specific coordination numbers (N) and atomic distances (R). In crystalline materials, the lattice dynamics are generally treated according to a harmonic approximation, inducing a Gaussian distribution of atoms' displacement. The effect of thermal and structural disorder is expressed in the Debye-Waller factor (σ^2). In glasses and even more so in liquids, an enhanced anharmonicity dominates, leading to an asymmetric distribution of the atomic displacements (Hardacre, 2005). These have to be described using an asymmetric distribution function instead of a Gaussian. Medium range order on the other hand can be found in the form of repetitive arrangements of linked

polyhedral, usually within a radial distance of up to 6 Å. Extended medium-range order may be present up to > 10 Å around a central atom, manifested in a specific network topology. However, with increasing distance from the reference atom, structural order diminishes (Calas et al., 2006).

Main constituents of silicate melts are the oxides of silicon (Si), aluminum (Al), alkalis, such as sodium (Na) and potassium (K), alkali earths, such as calcium (Ca) and magnesium (Mg), as well as iron (Fe). Silicate glass and melt structures are commonly described as polymeric networks with SiO_4^{4-} tetrahedra as the basic structural unit (Stebbins et al., 1995), as depicted in Figure 1 a. Oxygen atoms that link two tetrahedra (T) are referred to as bridging oxygen (BO), whereas oxygen atoms that only connect to one tetrahedron are referred to as non-bridging oxygen (NBO). An additional oxygen species is given by the so called free oxygen (FO), which do not interact with a network former (e.g. Guillot and Sator, 2011; Mysen, 1983; Nesbitt et al., 2011). Network modifying cations (e.g. Ca^{2+} or Na^{+}) can be incorporated at interstitial positions of the random network. Y, La and Sr are also known to act as network modifiers in silicate glasses and melts (e.g. Clayden et al., 1999; Florian et al., 2007; Henderson et al., 1985; Jaworski et al., 2012). Depending on bulk composition and respective local charge balance needs, bonds between two tetrahedra can be ruptured or cations such as Al^{3+} may replace Si^{4+} on the tetrahedral position. Experimental evidence from EXAFS (e.g. Greaves, 1985; Henderson, 1995) and molecular dynamics (e.g. Huang and Cormack, 1990; Smith et al., 1995; Vessal et al., 1992) on alkali-rich silicate compositions suggest a modified random network. This is characterized by domains or channels enriched in alkali cations and confined by NBOs percolating the silicate framework (Figure 1 b). These structural features are dedicated to serve as excellent diffusion pathways (Jund et al., 2001).

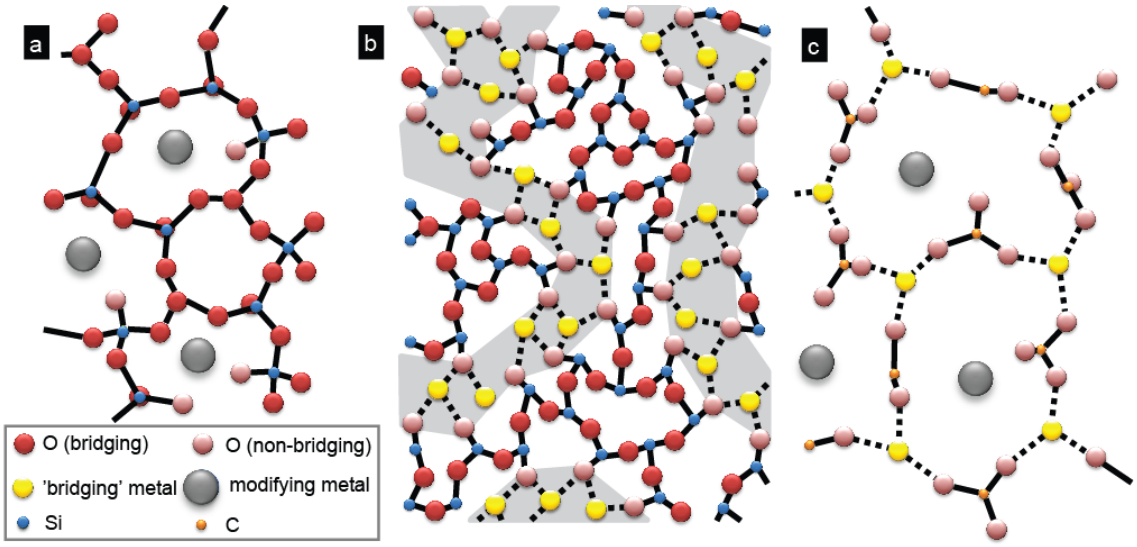

Figure 1: Structural models of silicate and carbonate melts.
Silicate melts described by (a) a random model (after Genge et al., 1995) and (b) a modified random network structure, suggested for alkali-rich compositions (after Greaves, 1985). The percolation channels of the latter are indicated in grey. (c) Carbonate melt structure as suggested by Genge (1995). In the models, oxygen can be bridging (BO in red) or non-bridging (NBO in pink). Solid lines represent covalent bonds, dotted lines ionic bonds.

One of the most important properties of these polymeric melts is the degree of polymerization. A common approach to quantify this is the ratio NBO/T (number of non-bridging oxygens per tetrahedron), which may be directly calculated from the melts chemical composition following a procedure by Mysen (1983). However, because the structural role of individual cations in the melt structure is not always unique (e.g. Al may act as network modifier or former, Henderson, 2005), the NBO/T-parameter can be ambiguous and therefore of limited use. An alternative approach is given by the aluminum saturation index (ASI, defined as the molar ratio of $Al_2O_3/(Na_2O+K_2O+CaO)$), which distinguishes between peralkaline, metaluminous and peraluminous silicate compositions. An increase in ASI at a constant Si/Al ratio up to 1 usually indicates a higher degree of polymerization (Zen, 1988).

The structural properties of a given melt strongly influence volatile solubility. In silicate melts, CO_2 solubilities are one to two orders of magnitude below that of H_2O (Ni and Keppler, 2013a). They may range between ~ 0.1 wt %, e.g. in basalt and rhyolite melts at 0.025 to 1.0 GPa (Botcharnikov et al., 2005; Fogel and Rutherford, 1990; Jendrzejewski et al., 1997), and 8 wt % or 15 wt %, e.g. in synthetic calcium sodium silicate systems at 0.2 GPa or 1.5 GPa, respectively (Brooker et al., 2001a). Mainly depending on chemical composition, silicate melts may contain molecular CO_2 or carbonate groups (CO_3). Generally, the latter can be incorporated in three potential configurations (De Jong and Brown, 1980; Eggler and Rosenhauer, 1978; Fine and Stolper, 1985; Kohn et al., 1991; Kubicki and Stolper, 1995; Mysen and Virgo, 1980a, 1980b):

(I) as an isolated and thus free metal-carbonate complex (FC), preferentially associated with alkali earth cations;

(II) by the attachment to network tetrahedra, preferentially via a non-bridging oxygen (T–CO_3), or even via a bridging oxygen ($^{T}_{T}-CO_3$);

(III) as a bridging element between two tetrahedra (T–CO_3–T).

In contrast to silicate melts, carbonate melts are ionic liquids consisting of carbonate groups (CO_3^{2-}) and metal cations, such as calcium, magnesium, iron and/or sodium. Their interaction is mainly controlled by electrostatic forces (Treiman, 1989). Recent studies suggest that carbonate liquids contain structural units considerably larger than individual CO_3^{2-} groups (Jones et al., 2013). Using vibrational spectroscopy at least two structural sites of CO_3^{2-} were identified by Williams and Knittle (2003) in a synthetic Na_2CO_3-$CaCO_3$-CaF_2 melt and by Genge et al. (1995) in synthetic glasses in the systems Mg-K-C-O and La-Ca-Ba-S-F-C-O-H. The investigated glasses are exceptional because carbonate liquids usually do not quench to glass. Based on their observations, the authors suggest that a flexible metal-carbonate framework is constructed by a strong interaction of the carbonate with two-valent metal cations, which serve as bridging elements between the carbonate molecules (Figure 1 c).

A common approach to investigate melt structures is to retrieve a glass by rapidly cooling the melt. This assumes that the glass provides an image of the melt structure frozen at the glass transition temperature[1] (Brown et al., 1995; Henderson, 2005; Seifert et al., 1981). While this approach is applicable for silicate melts within certain limitations (e.g. Brooker et al., 1999), carbonate melts are generally non-quenchable (Genge et al., 1995). Therefore, they need to be investigated at temperatures above the liquidus. Useful techniques to study molecular arrangements of liquids and glasses are provided by infrared or Raman spectroscopy (McMillan and Wolf, 1995), nuclear magnetic resonance (NMR) spectroscopy (Stebbins, 1995), X-ray scattering/diffraction (Brown et al., 1995; Warren, 1937) or neutron scattering (Wilding and Benmore, 2006). An outstanding method to investigate short to medium-range structural environments of specific elements, particularly at dilute concentrations, is X-ray absorption fine structure (XAFS) spectroscopy (Newville, 2014). It is based on element-specific excitation of core electrons and especially extended X-ray absorption fine structure (EXAFS) spectroscopy is a highly sensitive technique for elucidating bond lengths, coordination numbers and the degree of disorder. EXAFS has been successfully applied to investigate the local structure of major and trace elements in silicate glasses and melts (Brown et al., 1995; Peters and Houde-Walter, 1997; Simon et al., 2013). Additionally, molecular dynamics (MD) simulation proofed to be very useful to study glass and melt properties at conditions not easily accessible by laboratory experiments. MD simulations found wide applications in geoscience (Cygan and Kubicki, 2001), particularly for the investigation of silicate glasses and melts (e.g. Cormack et al., 2001).

[1] At the glass transition the melt's deformation changes from viscous, as in a liquid, to elastic, as in a solid (Dingwell and Webb, 1990). Below the glass transition temperature T_g the cooling melt structure is no longer able to adjust quickly enough to the change in temperature and falls out of equilibrium (Seifert et al., 1981). Generally, this holds true when the viscosity reaches 10^{12} Pa*s (Varshneya, 2013).

2 Methods

This chapter presents the methodological approach for investigating carbonate – silicate glasses and melts. Glass samples are relatively easy to treat in XAFS measurements. On the contrary, *in-situ* experiments on liquid materials require sophisticated technical equipment. The large volume press called Paris-Edinburgh press allows to apply high temperature and pressure onto the sample material. Its application will be introduced in chapter 2.1. Chapter 2.2 will outline how samples were prepared and characterized. Subsequently, chapter 2.3 and 2.4 will provide insights into the proceedings used in XAFS measurements and the accompanying molecular dynamics simulations, respectively.

2.1 Paris-Edinburgh press

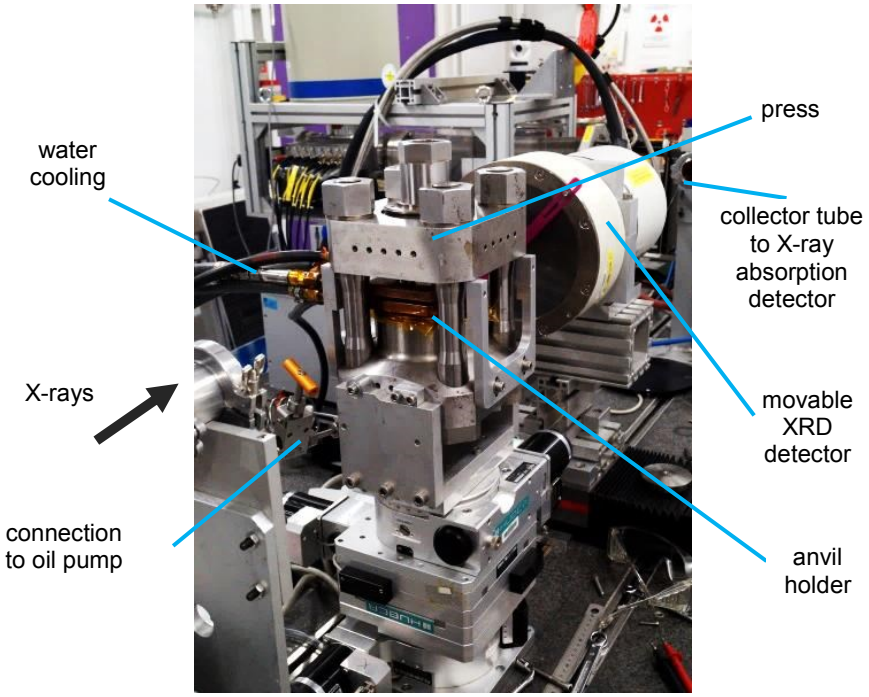

Figure 2: Photograph of the Paris-Edinburgh press.
The press is installed at beam line BM23, ESRF. X-rays arrive from the left hand side of the picture (black arrow) and pass through the sample mounted in the press. On the right hand side of the picture is the movable XRD detector, used for pressure/temperature-determination of the sample.

Originally, the Paris-Edinburgh press (Figure 2) was developed for *HP* experiments on neutron sources (Besson et al., 1992), but was progressively adapted to X-ray diffraction (XRD) and X-ray absorption experiments (e.g. Morard et al., 2007). The press is operated with oil pressure, which is transmitted to the pressure assembly containing the sample through a set of anvils with tungsten-carbide cores. The set-up is heated by applying a high current at low voltage through the anvils to the graphite heater inside the assembly. To avoid high temperature induced damage, the anvils are connected to a water cooling system.

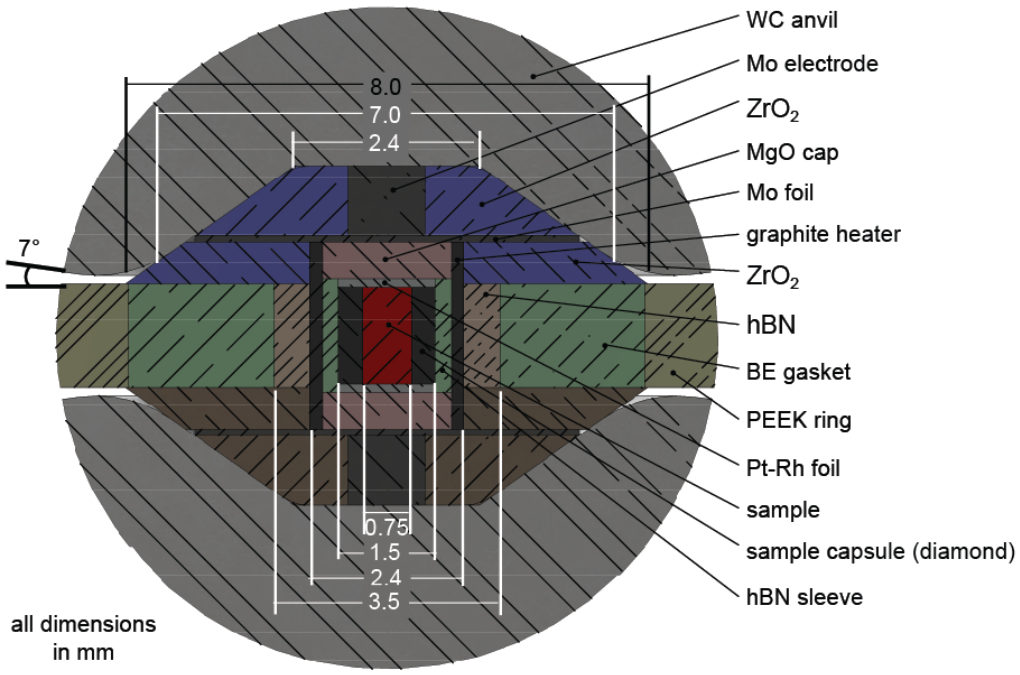

Figure 3: Sketch of the modified pressure assembly design of the Paris-Edinburgh press. The pressure assembly is based on zircon dioxide (ZrO_2), boron epoxy (BE) and hexagonal boron nitride (hBN) as pressure media. In order to heat, the molybdenum (Mo) parts transfer a current from the tungsten carbide (WC) core of the anvil to the graphite heater. The outer ring is made of polyether ether ketone (PEEK) and ensures the stability of the setup.

This study employed the 2.4 mm pressure assembly design by Morard et al. (2007) as well as a refined design of the 2.4 mm pressure assembly used by Yamada et al. (2011) for XRD experiments (Figure 3). In the modified set-up, the

MgO ring between the graphite heater and the amorphous boron epoxy was substituted by hexagonal boron nitride. This modified design showed a much better stability compared to the assembly by Morard et al. (2007), due to robust and low heat-conducting zircon dioxide parts at the top and the bottom of the layered assembly. Secondly, it allows for sufficient X-ray transmittance at the relevant energies as the radiation penetrated parts consist of the light materials boron nitride (as thermal insulator), boron-epoxy (as pressure medium), and polyether ether ketone (for mechanical stabilization). Figure 4 demonstrates the extraordinary X-ray transmittance properties as shown by comparative calculations of Rosa et al. (2016). The center of the pressure assembly contains a graphite heater around a nano-polycrystalline diamond (Irifune et al., 2003), which serves as an inert pressure capsule. The sample inside is confined by Pt-10%Rh foils at top and bottom.

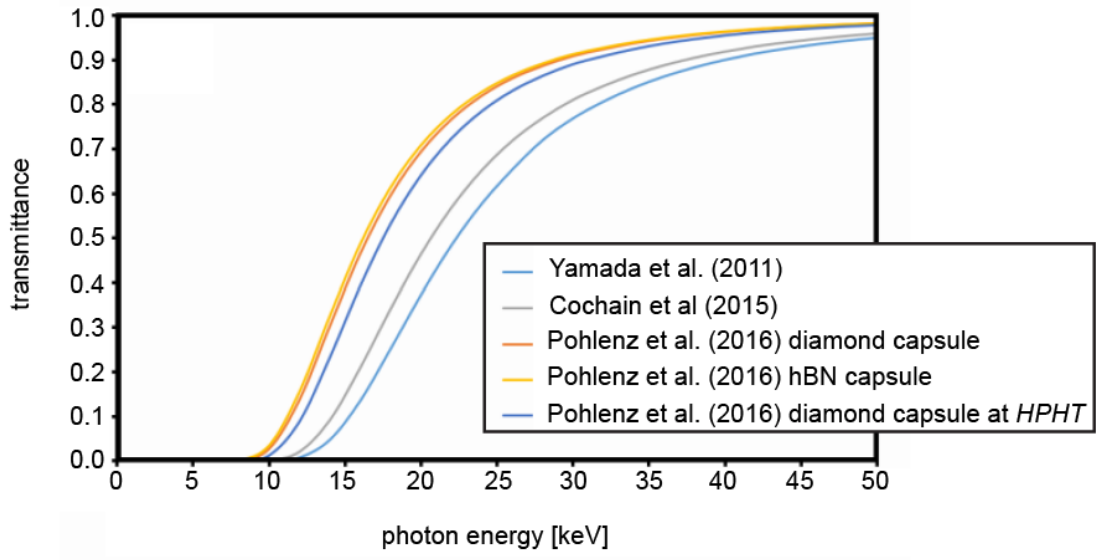

Figure 4: Calculated transmittances of different designs of pressure assemblies.
Transmittance calculation, assuming empty 2.4 mm cell assemblies, and graphic according to Rosa et al. (2016). Cell assemblies as used in EXAFS experiments by Yamada et al. (2011), Cochain et al. (2015) and Pohlenz et al. (2016). The *HPHT* calculation considers the deformation of the pressure assembly and thus the change in penetrated material volume as mechanically and thermally induced by the press.

Pressure and temperature conditions inside the sample capsule are determined by the double isochore technique (Crichton and Mezouar, 2002; Zhao et al., 1997). Therefore, calibration runs on reference materials (e.g. hexagonal boron nitride (hBN), magnesium oxide (MgO), Au, Pt) with known equations of states are conducted. XRD is used to probe their volumetric properties at distinct oil pressures and heating powers. The equation of state of each reference material can be used to describe possible combinations of pressure and temperature conditions for a given reference material volume. The intersection of at least two equations of states of different reference materials thus indicates the prevalent pressure and temperature inside the sample capsule at a given oil pressure and heating power. Uncertainties of this method are in the order of 0.2 GPa for the pressure and about 13 % for the temperature (Crichton and Mezouar, 2002).

2.2 Preparation and characterization of materials

2.2.1 Preparation of model compounds

Model compounds for Y, La and Sr XAFS analysis were Y_2O_3, La_2O_3 and $SrCO_3$. Table 1 lists the local structural data documented in the literature (derived by XRD). In the case of Y_2O_3, there are two different Y positions. Three-fourths of the positions are made up by Y1, which is coordinated by three sets of two oxygens of specific bond length (R). Y2 is symmetrically coordinated with six oxygens at a common distance. Both environments have a coordination number (N) of 6 and an average distance of $R_{Y\text{-}O}$ at 2.28 Å. The La site in La_2O_3 has 7 oxygen neighbors of three individual distances at an average distance $R_{La\text{-}O}$ of 2.53 Å. Sr in $SrCO_3$ has 9 oxygen neighbors of five different distances at an average distance $R_{Sr\text{-}O}$ of 2.64 Å.

Each model compound was ground and mixed with cellulose in an agate mortar to reach an optimum dilution level and pressed to a pellet of adequate thickness for EXAFS measurements.

Table 1: XRD structural first shell data of Y, La, and Sr in model compounds. Indicated are the coordination number N, individual cation-oxygen bond lengths $R_{M\text{-}O}$ and the respective average. The standard deviation is given in parentheses and refers to the last printed digit.

	N	$R_{M\text{-}O}$ [Å]	average $R_{M\text{-}O}$ [Å]
Y-O in Y_2O_3 (Kevorkov et al., 1995)			
Y1-O	2	2.243 (4)	
(24 x Y1 in a unit cell)	2	2.272 (3)	
	2	2.331 (3)	2.28
Y2-O	6	2.280 (3)	2.28
(8 x Y2 in a unit cell)			
La-O In La_2O_3 (Schiller, 1986)			
	3	2.365 (1)	
	1	2.457 (4)	
	3	2.727 (1)	2.53
Sr-O in $SrCO_3$ (De Villiers, 1971)			
	1	2.552 (9)	
	2	2.561 (6)	
	2	2.634 (5)	
	2	2.666 (5)	
	2	2.725 (4)	2.64

2.2.2 Sample preparation of silicate – carbonate glasses and melts

Glasses and melts ranging from silicate to carbonate compositions were synthesized in the system Na_2O-CaO-Al_2O_3-SiO_2-CO_2 at constant Si/Al (~ 4.8) and Ca/Na (~ 0.35) ratios (Figure 5, Table 4). Two compositional ranges were in focus on the silicate side, each with increasing CO_2 contents: one Si-Al-rich (*sSA*), strongly peralkaline, and one Na-Ca-rich (*sNC*), of even higher peralkalinity (cf. Table 4). *sSA* represents a simplified version of the bulk composition of nephelinitic rocks found at the Oldoinyo Lengai and is similar to the silicate melt of the trace element partitioning experiments by Veksler et al. (1998). *sNC* represents a simplified composition of silicate glasses found in nepheline melt inclusions and as matrix glass in silicate rocks of the Oldoinyo Lengai (De Moor et al., 2013). On the carbonate side, three compositions with SiO_2 contents

between 0 and 6 wt % were investigated, similar to natural melts of Oldoinyo Lengai carbonatites (Petibon et al., 1998).

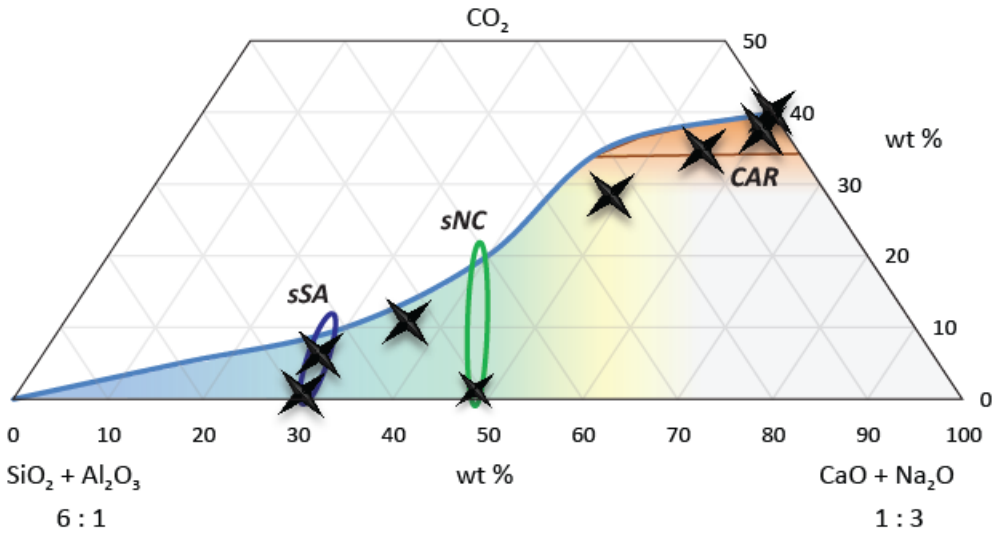

Figure 5: Chemical composition of glass and *in-situ* melt samples.
Chemical composition in wt % of investigated silicate glass samples for strongly peralkaline (*sSA,* blue oval) and extremely peralkaline (*sNC,* green oval) compositions. Both series with ~ 0.5 wt % Y_2O_3 and SrO or La_2O_3. All investigated *in-situ* melt samples for *sSA, sNC* and *CAR* compositions are marked with stars and contain ~ 2 wt % Y_2O_3 and SrO or 6 or 3 wt % La_2O_3.

All syntheses were performed with powders of SiO_2, Al_2O_3 (both dried at 400 °C), Na_2CO_3, $CaCO_3$, SrO, Rb_2CO_3, Nb_2O_5, Y_2O_3 and La_2O_3 (all dried at 200 °C). The reagents were ground with ethanol in an agate mortar for homogenization. Trace-element free glasses of *sSA* and *sNC* were prepared by mixing the powders in respective proportions. They were decarbonated and further homogenized during melting at 1200 °C for at least 24 h. The melts were quenched to glasses by placing the crucible in a water bath right after retrieving it from the furnace. The glasses were finely ground and dried at 200 °C. In a first series they were mixed with ~ 0.5 wt % Y_2O_3, SrO and Rb_2CO_3 each and in a second series with ~ 0.5 wt % La_2O_3 and Nb_2O_5 each. These mixes were fused again at 1200 °C for at least 24 h, quenched to glass and finely ground. Oxide-carbonate mixes from the first step (containing the same Si-Al-Na-Ca ratios) were added to achieve varying CO_2 content without changing the ratios of the remaining elements. The final mixtures were dried at 200 °C, prepared in a plat-

inum capsule and run for 48 h at 1200 °C and 0.7 GPa in an internally heated pressure vessel (for more details on the vessel refer to Roux et al., 1994). Additionally, CO_2-free and low CO_2-bearing samples of *sSA* and *sNC* composition were prepared with ~ 2 wt % H_2O. One further synthesis of Y and Sr bearing *sSA* composition with a final CO_2 content of 6 wt % was prepared using a piston cylinder apparatus at 1200 °C and 1.5 GPa. Glass samples for *ex-situ* XAFS at ambient conditions were prepared by cutting pieces of the synthesized glasses to an appropriate thickness. Y- and Sr-doped glasses were prepared for measurements in fluorescence mode and cut to thin plates of a thickness of ~ 0.6 mm. La-doped glass samples for measurements in transmission mode were prepared as cylinders of lengths between 5 and 10 mm.

Melts for *in-situ* XAFS, were prepared to allow for full investigation along the silicate-carbonate join. Silicate compositions were prepared as described above, whereas carbonate (*CAR*) compositions were prepared as follows: CO_2-free glasses (same starting material as for the *ex-situ* glasses) were mixed with oxide-carbonate or Na_2CO_3-$CaCO_3$ mixtures (of same Si/Al or Na/Ca ratios) to reach varying CO_2 contents in the final compositions. Adequate proportions of Y_2O_3, SrO and La_2O_3 were added to obtain 2 wt % Y and Sr or 3 or 6 wt % La. These mixtures were dried and filled into cylinders of nano-polycrystalline diamonds (Irifune et al., 2003), used as a pressure capsule in *in-situ* XAFS experiments.

2.2.3 Chemical sample composition

All synthesized glasses used for *ex-situ* XAFS were analyzed by electron microprobe (Table 4). Run products of *in-situ* XAFS experiments, i.e. quenched *in-situ* samples, were recovered from the nano-crystalline diamond capsule, mounted in epoxy, ground and polished. Quenched *in-situ* samples of *CAR* compositions were dry ground and polished to avoid dissolution of the microcrystalline carbonate quench products. Only La-bearing *CAR* compositions were retrievable. In addition to elements given by the starting composition, quenched *in-situ* samples were also analyzed for boron. This is necessary because of a potential boron contamination originating from the boron nitride pressure assembly of the Paris-Edinburgh press (Seifert, 2013). Analysis was conducted by a JEOL

Hyperprobe JXA-8500F with field emission electron source or a JEOL SUPER-PROBE JXA-8230 with a LaB_6 cathode. An acceleration voltage of 10 to 15 kV, a beam current of 5 to 10 nA and an enlarged beam diameter of at least 20 µm was employed. To impede analytical artifacts by Na migration due to the electron beam, Na was analyzed first and measurement conditions were chosen to create a low beam current density of 0.01 to 0.03 nA/µm². Counting times were 5 s for the major elements, 20 s for Rb, 30 s for Y and Sr, 50 s for La and Nb and 80 s for B on the peaks and 5 s on the background. The standards used were plagioclase for SiO_2 and Al_2O_3, diopside for CaO, tugtupite for Na_2O, yttrium phosphate for Y_2O_3, $SrSiO_3$ for SrO, $RbAlSi_3O_8$ for Rb_2O, lanthanum phosphate for La_2O_3, niobium metal for Nb_2O_5 and schorl for B_2O_3. Counting errors of X-ray intensities were between 2 % (major elements) and 4 % (trace elements). Each sample was scanned in two lines with 20 to 50 points each.

CO_2 contents of all glasses were determined with an Eltra CS800 analyzer and H_2O contents of water bearing samples were determined by a Karl Fischer titrator CA100 at Leibniz University, Hannover, Germany. Sample volumes from piston cylinder syntheses and sample volumes of quenched *in-situ* samples were too small to be analyzed for CO_2 content.

2.3 X-ray absorption fine structure (XAFS) experiments

2.3.1 Theoretical introduction to XAFS

A direct method to investigate the short- to medium-range structural environment of specific elements is given by X-ray absorption fine structure (XAFS) spectroscopy (Newville, 2014). It is based on the absorption of X-rays of distinct energies (E) by electrons in tightly bound quantum core levels of the atom, such as in the K or L shells. If the energy of the incoming X-ray is equal to the binding energy of an electron, the electron may be removed from its quantum level, leaves a core hole and the corresponding X-ray is absorbed (Figure 6, indicated in blue).

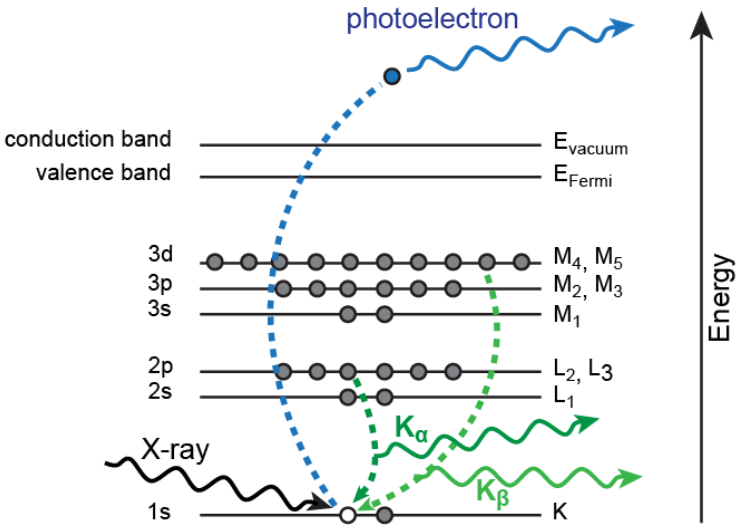

Figure 6: Scheme of the photoelectric effect and relaxation by fluorescence.
An incoming X-ray is absorbed by the atom and promotes a core level electron (in this example from the K shell) to the continuum. This creates a photoelectron and a hole in the core electron level (in blue). The excited state may decay by electron movement from a less tightly bound orbital to the empty core level (in green) with the emission of X-rays (K_α and K_β). The X-ray energy is equal to the energy difference between the two levels. Graphic modified after Newville (2014).

Electrons, which are excited to the continuum as photoelectrons travel as spherical wave and may be backscattered by neighboring atoms. Interference of outgoing and backscattered photoelectrons creates modulations of the absorption coefficient of the absorbing atom which are detected in the extended X-ray absorption fine structures (EXAFS). EXAFS provides information about interatomic distances, bond angles, coordination numbers and the degree of order (Rehr and Albers, 2000) as illustrated in Figure 7. The X-ray absorption near edge structures (XANES) are generated by more complex processes, involving transitions of the excited electron to localized unoccupied electronic levels (pre-edge features) as well as multiple scattering events. XANES is a particularly sensitive probe of the coordination symmetry and the oxidation state of the absorbing species (Behrens, 1992).

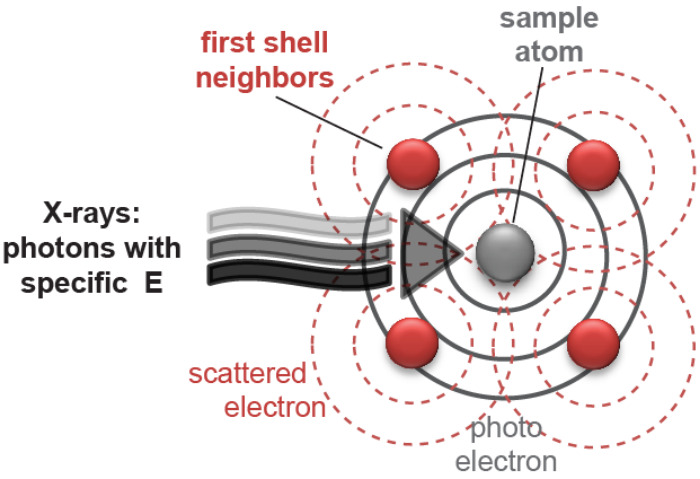

Figure 7: Scheme of the creation of photoelectron interferences.
The photoelectron waves generated in the sampled atom by an incoming X-ray propagates to neighboring atoms. The outgoing and backscattered waves (solid, respectively, dashed red lines) create interferences. These depend on the type of neighboring atoms, their distance, number and disorder and give rise to the EXAFS oscillations. Graphic modified after Rehr and Albers (2000).

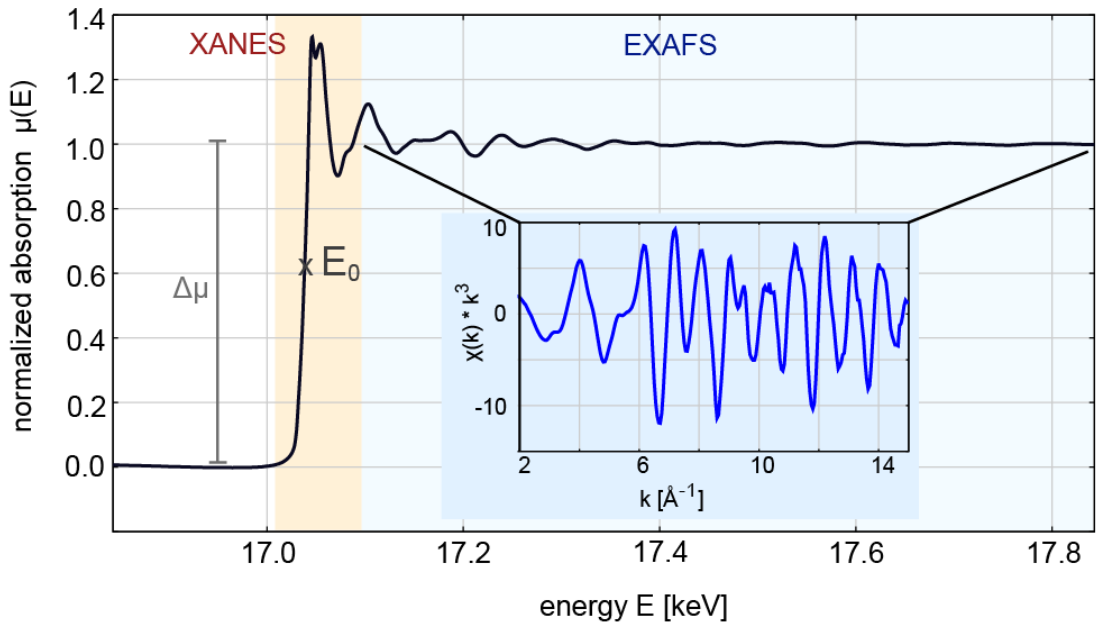

Figure 8: X-ray absorption fine structures of the Y K-edge of Y_2O_3.
Shown are the near-edge region (XANES) and the extended fine structures (EXAFS) as a function of energy μ(E). The inlet shows the fine structure function χ(k).

Figure 8 shows a typical XAFS spectrum of the Y K-edge of Y_2O_3. At the ionization energy of the core electron E_0, a sharp rise in absorption is observed, called the absorption edge (Newville, 2014). Its intensity can be described by the edge jump $\Delta\mu$, which is the difference of absorption below and above the edge energy and is proportional to the element concentration. The XANES region typically ranges from below the edge to ~ 30 eV above the edge (orange area in Figure 8). The EXAFS region reaches from beyond the edge up to several hundred eV (blue area in Figure 8). For high-quality measurements, samples are ideally prepared to reach a total absorption of 1 and an edge-jump of 1 (Brown et al., 1995; Bunker, 1983).

In XAFS analysis, the X-ray absorption signal $\mu(E)$ is composed of two parts (eq. 1): (1) The absorption energy due to the excitation of a core level electron of an isolated atom $\mu_0(E)$. (2) The X-ray absorption due to interferences of the photoelectron's interactions with neighboring atoms (Figure 7), known as the EXAFS fine-structure function $\chi(E)$.

$$\mu(E) = \mu_0(E)[1 + \chi(E)] \tag{1}$$

As EXAFS analysis only regards the fine structure function, $\chi(E)$ can be isolated from eq. 1 by employing the edge jump $\Delta\mu$ as follows:

$$\chi(E) = \frac{\mu(E) - \mu_0(E)}{\Delta\mu} \tag{2}$$

From a quantum mechanical point of view, the X-ray absorption $\mu(E)$ represents the transition from the initial quantum state, $\langle i|$, with an X-ray and a core electron to the final quantum state, $|f\rangle$, with a core hole and a photo electron. As such it can be described with Fermi's Golden Rule, with the transition represented by the interaction term H:

$$\mu(E) \propto |\langle i|H|f\rangle|^2 \tag{3}$$

Eq. 3 can be adopted to describe Fermi's Golden Rule for the isolated EXAFS signal $\chi(E)$. The final quantum state $|f\rangle$ consists of two contributions: the portion related to the isolated atom, $|f_0\rangle$, and the portion that is evoked by the

neighboring atoms $|\Delta f\rangle$. Thus, the fine structure $\chi(E)$ can be expressed by only focusing on the latter part:

$$\chi(E) \propto \langle i|H|\Delta f\rangle \tag{4}$$

Since EXAFS is interpreted in terms of waves created by the photoelectrons, it is convenient to convert the X-ray energy E into the kinetic energy of the photoelectron and convert it to the wave number k. the kinetic energy of the photoelectron is measured with respect to the absorption edge E_0:

$$k = \sqrt{\frac{2m_e(E - E_0)}{\hbar^2}} \tag{5}$$

Here, $\hbar$ the reduced Planck constant and m_e the electron mass. A common solution of eq. 4 in wave space is derived by applying a range of assumptions (Newville, 2014) and results in eq. 6:

$$\chi(k) = \sum_j \frac{S_0^2 N_j f_j(k) e^{-2R_j/\lambda(k)} e^{-2k^2\mu_j^2}}{kR_j^2} \sin[2kR_j + \delta_j(k)] \tag{6}$$

Here, j refers to the atom type coordinating the central atom, N is the coordination number of the central atom in regard to atoms of j, R is the average bond length between the central atom and the atoms of j and σ^2 the corresponding Debye-Waller factor. f(k) and $\delta(k)$ describe scattering properties of atoms of j, i.e. its amplitude and phase-shift function, respectively. $\lambda(k)$ represents the mean free path of the photoelectron, i.e. the distance it can travel before scattering inelastically (or the core hole is filled). S_0 is referred to as the amplitude reduction factor and accounts for intrinsic losses due to relaxation of the other electrons in the excited atom.

XAFS can be measured in two ways (Newville, 2014). In transmission XAFS the absorption is derived by sampling the intensity of an X-ray beam before (I_0) and after (I) being transmitted through a sample of thickness t. This is based on the Beer-Lambert law, which describes the absorption coefficient μ as the probability that an X-ray will be absorbed passing through a material:

$$I = I_0 e^{-\mu t} \tag{7}$$

By normalizing over the sample thickness the X-ray absorption can be measured as:

$$\mu(E) = \ln \frac{I_0}{I} \tag{8}$$

A second way to measure XAFS takes into account that the excited states will eventually decay, usually within a few fs. This most likely happens by one of two main mechanisms. An electron of a less tightly bound orbital fills the deeper core hole and simultaneously ejects either an X-ray (X-ray fluorescence, indicated in green in Figure 6) or a second electron (Auger effect). In both cases, all core holes will be gradually filled with less tightly bound electrons until the atom is fully relaxed. The emitted particles (X-ray photon or electrons) have characteristic energies, which are shell and atom specific. The probability of emission is directly proportional to the absorption probability. Thus, a second possibility to measure X-ray absorption is in fluorescence mode as given by:

$$\mu(E) \propto \frac{I_f}{I_0} \tag{9}$$

With I_f as the measured intensity of the fluorescence line (or electron emission) associated with the absorption process.

As the core-level electrons of every atom have distinct binding energies, XAFS measurements can be element-specifically conducted by tuning the X-ray energy to the appropriate absorption edge. XAFS techniques rely on brilliant X-ray radiation with a continuous spectrum. Thus, more than 99 % of all EXAFS studies are conducted at synchrotron light sources (Gurman, 1995), such as the European Synchrotron Radiation Facility (ESRF) in Grenoble, France or Soleil Synchrotron, Gif-sur-Yvette, France.

2.3.2 XAFS measurements

Y K-edge (17.038 keV) and Sr K-edge (16.105 keV) fluorescence XAFS as well as La K-edge (38.925 keV) transmission XAFS measurements on glass samples were performed at SAMBA beamline at SOLEIL Synchrotron, France (Briois et al., 2011) using a Si 220 double-crystal monochromator. Two mirrors at a grazing angle of 3 mrad were employed. The beam was focused and had a size of 500 x 500 μm^2 FWHM. The energy of the monochromator was calibrated at the Zr K-edge using a metallic Zr-foil. In fluorescence mode the sample was turned to 45 ° to the beam with a detector angle of 90 ° to the incident beam. The fluorescence signal was collected with a 35-pixel Ge detector (Canberra) and dead-time corrected.

All experiments on *in-situ* melt samples at high pressure and temperature (*HPHT)* and on the quenched *in-situ* samples, still at high pressure (*HP*), were conducted in transmission mode using a Paris-Edinburgh press (Morard et al., 2007; Rosa et al., 2016) installed at beam line BM23, ESRF (Mathon et al., 2015). One series of runs employed the 2.4 mm pressure assembly design after Morard et al. (2007). Subsequent runs used a design that was modified after Yamada et al. (2011) as presented in chapter 2.1. The liquid state of the *in-situ* experiments was determined by the absence of crystalline phases in the sample volume as indicated by *in-situ* XRD. Pressure and temperature conditions applied by the Paris-Edinburgh press were chosen to stabilize one homogenous melt, avoiding potential liquid immiscibility. Silicate compositions were investigated as melts *in-situ* at 2.2 GPa and 1500 °C and afterwards as quenched glasses (quenched *in-situ* samples). The quench was accomplished by cutting the power supply to the graphite heater. During the quenching process the pressure dropped to 1.8 GPa. Carbonate melts do not quench to a glass and were investigated only *in-situ* at 2.6 GPa and 1200 °C. The XAFS measurements were carried out using a Si(111) double-crystal monochromator. Harmonic rejection down to a level of 10^{-5} was achieved by using a vertical deflecting double mirror system. For Y and Sr measurements, Rh-coated mirror strips were used and inclined to a grazing angle of 3 mrad. For La measurements, Pt-coated mirror stripes were used and inclined to a grazing angle of 2 mrad. The beam was vertically focused down to

50 μm FWHM using the bender mounted on the second mirror of the double mirror system and horizontally collimated to 0.1 mm using slits.

All model compound pellets were measured in transmission mode at both synchrotron facilities. Spectra of each sample were recorded starting from at least 150 eV below the edge. Glass and *in-situ* measurements of Sr reached up to 650 eV (k of 13 $Å^{-1}$), of Y and La up to 750 eV (k of 14 $Å^{-1}$) above the edge. Model compound spectra were collected up to 965 eV (k of 16 $Å^{-1}$) above the edge. For each sample, two to four spectra were measured until sufficient counting statistics and adequate signal to noise ratios were reached.

2.3.2.1 Data Processing

XAFS spectra of each individual sample were summed and averaged using the Athena software (Ravel and Newville, 2005). Further analysis was conducted using the XAFS package (Winterer, 1997). All spectra were background corrected by subtracting a polynomial function fitted to the spectral region below the edge. The edge position E_0 was identified by fitting an error function. Additional step height correction was needed for Y and Sr spectra, which show a strong peak at the main edge. This was done by adjusting the edge-jump to an isosbestic point (for Y at ~ 60 eV, for Sr at ~ 90 eV after the edge). EXAFS oscillations were background-subtracted and normalized using a natural cubic spline function. The normalized EXAFS signal $\chi(E)$ was transformed into k space using eq. 5. To enhance features at higher energies the spectra were k^3- or k^2-weighted. While crystalline materials can be adequately fitted with a k-weighting of 3, the EXAFS of glasses and melts are usually only fittable using a k-weighting of 2.

2.3.2.2 EXAFS Fit Model

Glasses and melts are highly disordered systems, thus the EXAFS basically contain contributions from the first coordination shell (cation-oxygen pairs). To account for the enhanced anharmonicity of the lattice dynamics in glasses and

melts (cf. chapter 1.2) various methods for data analysis have been suggested (Daryl Crozier, 1995; Filipponi, 2001; Simon et al., 2013; Yang et al., 1997). In this study, an EXAFS fit model as given in eq. 10 and 11 was applied (analytical distribution fit as in Winterer, 1997). The model is based on an asymmetric distribution function to describe the first coordination shell of the metal cations in glasses and melts. The model is applied at constant values for S_0.

$$\chi(k) = f * \frac{R_s^2}{N_s} * \frac{\mathbf{N}}{\mathbf{R^2}} * e^{\{2k^2 * (\sigma_s^2 - \boldsymbol{\sigma^2})\}} * (1 + z(k)^2)^{-\frac{m+1}{2}} * \sin\{\delta(k) + 2k * (\mathbf{R} - R_s) - \frac{f_c \, \boldsymbol{\Delta E_0} \mathbf{R}}{k} + (m+1)(-z(k) + \arctan(z(k)))\} \quad (10)$$

where

$$z(k) = 2k * |\mathbf{h}| \quad (11)$$

Where f is the amplitude of the reference, δ the phase of the reference, N_s the path degeneracy of the reference, R_s the path length of the reference, σ^2_s the Debye-Waller factor of the reference, f_c the conversion factor of 0.262467 $V^{-1}Å^{-2}$, and m the power of the weighing function. Parameters to fit are in bold: **N** as number of neighbors, **R** as average bond length, $\boldsymbol{\sigma^2}$ as Debye-Waller factor, $\boldsymbol{\Delta E_0}$ as inner potential shift (deviation from the theoretical Fermi level) and **h** as asymmetry parameter. The resulting distribution function p(r) of atoms around the X-ray absorbing atom as a function of distance r is given by eq. 12 (Winterer, 1997; Yang et al., 1997).

$$p(r) = g(r) * N = \frac{N}{m!} * \left(\frac{1}{|h|}\right)^{(m+1)} * (r - R)^m * e^{\left\{-\frac{r-R}{|h|}\right\}} \quad (12)$$

Reference material fits

As references served phase and amplitude functions derived from the model compounds (Y_2O_3, La_2O_3, $SrCO_3$) using the FEFF9 package (Rehr et al., 2010). The measured model compound EXAFS were Fourier filtered (using a Kaiser

Bessel window with a weighing of 4) to extract their first shell contribution. The FEFF calculation was optimized to obtain best one-shell fit results for each model compound (with variable N, R, σ^2, h, ΔE_0 and iterating through fixed values of S_0). Best fits were determined by derived structural parameters (especially N and R) being consistent with XRD structural data (Table 1), statistical parameters (standard deviation of fit parameters, reduced χ^2 of fits) and obtained results being independent of k-weighing (2 or 3). The potential was optimized with a self-consistent potential radius (SCF) of 4 Å and a maximum effective (half-path) distance (RPATH) of 7 Å. In all model compounds, the absorbing element is surrounded by first shell oxygens O_r at different distances r (in Å), which lead to individual paths in the FEFF calculation. The fit quality proved to depend on the chosen path as well as on the used cut-off radius. Best fits were obtained for Y_2O_3 using the path of Y1-$O_{2.272}$ and a cut-off at 4 Å, for La_2O_3 using the path of La-$O_{2.365}$ and a cut-off of 3 Å and for $SrCO_3$ using the path of Sr-$O_{2.2724}$ and a cut-off of 6 Å. Respective phase and amplitude functions as well as associated values of ΔE_0 and S_0 were used in subsequent fitting of melt and glass samples. The parameter m is not a fit parameter and has to be chosen prior a given fit. It substantially influences the shape of the fitted distribution function at higher distances. Tests showed that best results were obtained with an m of 2.

Coordination number – bond length correlation

To mitigate the often considerable uncertainty in fitting the coordination number N (e.g. Brown et al., 1995), N was correlated to R according to bond valence theory (Bickmore et al., 2017; Brown, 2009), which employs the parameter of bond valence or bond strength s (Brese and O'Keeffe, 1991). s is defined by dividing the formal charge z_c of a cation by its coordination number N (eq. 13). It also can be derived from the relationship between a measured bond length R and an empirically determined ideal bond length R_0 for a given material (eq. 14).

$$s = \frac{z_c}{N} \quad \text{or} \quad s = e^{\frac{R_0 - R}{0.37}} \qquad (13) \quad \text{and} \quad (14)$$

Due to thermal expansion at higher temperatures, R_0 has to be corrected by adding the product of the temperature and the thermal expansion coefficient α (Hazen et al., 2000):

$$\alpha = 4.0(4) * \frac{N}{i^2 z_c z_a} * 10^{-6} K^{-1} \quad (15)$$

Where i^2 is an empirical ionicity factor (of 0.5 for silicates and oxides) and z_c and z_a are cation and anion valences. It is reasonable to assume that the range of pressures investigated in this study has only minor impact and thus does not require correction.

Table 2: Parameters of linear approximation of N-R correlation.
Indicated are the element-specific parameters m_{Nr} and n_{NR} as coefficients of the linear regression $N(R)= m_{NR} * R + n_{NR}$ for each studied cation-oxygen pair and temperature condition[a]. Respectively determined N deviate at most 1 % from N calculated directly applying eq. 13 and 14 according to bond valence theory.

		Y-O	La-O	Sr-O
ambient temperature	m_{NR}	20.20	23.88	18.42
	n_{NR}	-39.96	-52.51	-40.51
1500 °C	m_{NR}	19.55	22.87	17.27
	n_{NR}	-38.69	-50.29	-37.96
1200 °C	m_{NR}	19.45	23.07	17.49
	n_{NR}	-38.48	-50.72	-38.46

[a] N: coordination number, R: average bond length

Element specific values of R_0 as given by Brese and O'Keeffe (1991) and Hazen et al. (2000) were employed in eq. 13 to 15 to derive N-R correlations for Y, Sr and La at the prevalent temperatures. According to input requirements of the software package XAFS the correlation was fitted linearly over the region of experimentally observed bond lengths in this study in the form of $N(R) = m_{NR} * R + n_{NR}$. The determined model parameters m_{NR} and n_{NR} for differ-

ent temperatures are used to correlate N to R in the EXAFS fits and are given in Table 2.

2.3.2.3 EXAFS Sample fits of melts and glasses

Glass and *in-situ* EXAFS $\chi(k)$ were fitted in unfiltered k space, with k^3-weighing for Y and k^2-weighing for Sr and La. Values of S_0 and ΔE_0 were taken from the model compound fits and N was correlated to R as explained above. Thus, fitted parameters for glass and melt samples were reduced to R, σ^2 and h. The latter two are closely correlated parameters describing the structural disorder of the local arrangement and they are particularly sensitive to the amplitude of the EXAFS. In combination with relatively short EXAFS signals, a simultaneous fit of all three parameters is unfortunately not feasible. Starting values of σ^2 and h were derived by a preliminary fit approach, under the assumption that glass- or melt-state dependent and element specific values of σ^2 and h can be applied. This procedure involved running through different combinations of fixed values for σ^2 and h at different sets of variable and fixed parameters (out of R, N, σ^2, h and ΔE_0). Optimal values for σ^2 and h were chosen according to fit consistency (e.g. physical meaning, resemblance of results in k^2- and k^3-weighted fits) and statistical parameters. In a second step, derived values of σ^2 and h were refined by an iterative fit procedure, letting R run free and alternatingly setting one amplitude parameter constant to values as derived from the previous iteration. Tested fit models of: (I) variable σ^2 and R; or (II) variable h and R showed that σ^2 and h can be treated as constant for a given element in the suite of melts or glasses (independent of ΔE_0 being fixed or variable). This is closely linked to the fact that these parameters are strongly correlated. They therefore show large standard deviations (0.005 - 0.010 $Å^{-2}$ for σ^2, 0.01 - 0.06 $Å^{-1}$ for h). During the fit procedure, initial values for ΔE_0 were refined to a minor degree (max. 2 eV).

2.4 *Ab initio* molecular dynamics simulations

2.4.1 Theoretical fundamentals on molecular dynamics

Molecular dynamics (MD) refers to computer simulations, which model the interactions of Lagrangian particles (e.g. atoms, molecules, granules) over time. The method was first implemented using a hard sphere model to represent atoms (Alder and Wainwright, 1959). They are widely used in chemistry, physics and biology at many different types of systems, such as glasses, liquids, solids, surfaces or proteins. They are particularly advantageous in modeling systems which are often difficult to access experimentally, such as disordered systems and/or systems at elevated pressure/temperature conditions (Allen and Tildesley, 1989). MD provides a window into the dynamical behavior of a system of particles by iteratively calculating its total energy and acting forces for each simulation time step. From the resulting trajectory it is possible to calculate dynamical properties such as absorption spectra, rate constants or transport properties as well as equilibrium properties such as pressure, temperature, volume and structure (Tuckerman and Martyna, 2000).

There are many approaches to solve the equations of motion of an assembly of atoms in MD simulations. In the so-called classical approach, the force field responsible for atomic interaction can be derived from element specific interaction potentials, which are empirically determined. On the other hand, in *ab initio* (or first-principle) MD the energy of a system is calculated from quantum mechanics, often within the density functional theory framework (Hohenberg and Kohn, 1964; Kohn and Sham, 1965). *Ab initio* MD can be a powerful and highly predictive tool, also for highly elaborated systems, where classical interaction potentials may not sufficiently describe behavior of involved atoms. However, its high computational demand currently restricts *ab initio* simulations to time spans of 10 – 100 ps and system sizes to a few hundred atoms[2]. To overcome the thereon based large surface effect on the cell boundaries, the sim-

[2] In contrast to classical MD, which are applicable for several thousands of particles over time spans of ~ 10 ns.

ulation cell is duplicated in all three dimensions as exemplary shown for two dimensions in Figure 9.

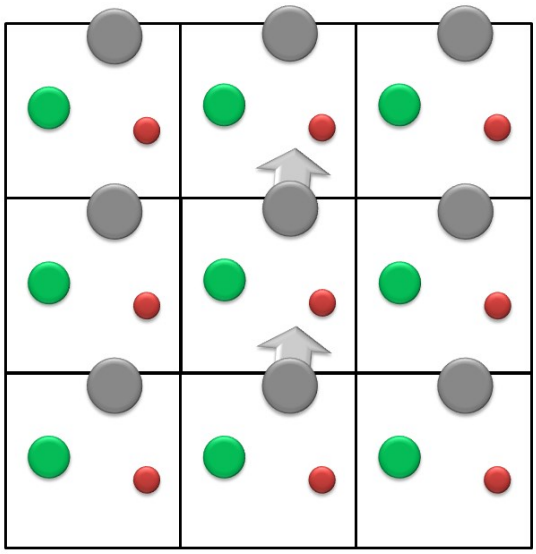

Figure 9: Schematic illustration of two-dimensional periodic boundaries in MD simulations. The simulation cell (in the middle) contains three atoms (red, green and grey) and is surrounded by periodic duplicates (after Hoover and Rossj, 1971). This set-up enables to also realistically reproduce the behavior of particles close to the boundaries. Here, the grey atom is about to leave the simulation cell to the top. The periodic boundaries ensure that it is immediately replaced by its periodic image entering from the bottom. This ensures constant numbers of atoms in the simulation cell at all times.

2.4.2 Procedure of MD simulations

All MD simulations in this thesis are *ab initio* simulations of Born-Oppenheimer-type and were performed using the QUICKSTEP module (VandeVondele et al., 2005) of the CP2K software package (Hutter et al., 2014). The Perdew-Burke-Ernzerhof exchange correlation functional (Perdew et al., 1996) and Goedecker-Teter-Hutter (Goedecker et al., 1996) norm-conserving pseudopotentials were employed. As basis sets served double-zeta valence plus polarization basis sets (VandeVondele and Hutter, 2007). A plane wave cutoff of 120 Ry was chosen as a compromise between accuracy and efficiency. The simulations were run in a canonical ensemble.

Table 3: Simulations cell parameters for Y-bearing melts.
Indicated are the number of atoms (n), the box lengths and the respective densities for each Y-bearing composition. Corresponding Sr cells were designed by substituting a set of Y, Na and O for one Sr (on former Y position). Box lengths were chosen to create densities estimated for ~ 2 GPa and 3000 K.

		sSA00	*sSA03*	*sNC10*	*CAR40/41*
Number of atoms	$\mathbf{n_O}$	115	118	106	106
	$\mathbf{n_{Si}}$	40	40	24	-
	$\mathbf{n_{Al}}$	8	8	5	-
	$\mathbf{n_{Na}}$	31	29	38	49
	$\mathbf{n_{Ca}}$	6	6	8	10
	$\mathbf{n_C}$	-	2	11	35
	$\mathbf{n_Y}$	1	1	1	1
	$\mathbf{n_{total}}$	201	204	193	201
Box length [Å]		14.2	14.3	14.5	14.3
density [g/cm³]		2.44	2.41	2.17	2.13

Two series of explorative MD simulations were conducted: one focusing on Y and one on Sr bearing melts. Each series comprises four different compositions corresponding to *sSA* with 0 and 3 wt % CO_2 (*sSA00* and *sSA03*), *sNC* with 10 wt % CO_2 (*sNC10*) and silicate free carbonate (*CAR41*). To reach low elemental concentration of Y and Sr analogue to the chemical composition of XAFS samples, only one single atom of Y or Sr was introduced into the simulation cell. The cubic simulation cells contained ~ 200 atoms (Table 3). Periodic boundary conditions are applied at all times. Lengths of the cell box were chosen to represent densities corresponding to conditions of ~ 2 GPa (see Appendix 1 for calculations).

Initial configurations for Y-bearing melts were derived from a random distribution of atoms, taking into account typical interatomic distances. Such initial configurations are usually unrealistic and firstly need to be equilibrated until the systems properties do not change significantly. Especially in silicate networks, reaching equilibrium is a sluggish process that is circumvented by elevated temperatures (e.g. Cormack et al., 2001). Thus, each cell was equilibrated

at 3000 K for at least 50 ps. The simulations were performed with 1 fs time step and data were collected for every second time step. The temperature was controlled by a Nosé-Hoover thermostat (Hoover, 1985; Nosé, 1984). Starting configurations for Sr melt simulations were derived from equilibrated Y-bearing melts by substituting Sr for Y, while eliminating one Na and one O to maintain charge balance. As cell box lengths remained constant, densities in the Sr-bearing melts represent conditions of ~ 1.8 GPa. The new cells were equilibrated for at least 50 ps. Additionally, Y melts were quenched in order to obtain corresponding glass structures. For this, the last step of each Y melt served as starting configuration for the quench and was cooled down to ambient temperatures (300 K) by 100 K every 2 ps (i.e. with a quench rate of $5 * 10^3$ K/s). The final quench products were run at 300 K for 20 ps and sampled every second time step.

2.4.3 Evaluation of molecular dynamics simulations

Basic structural information is derived by statistically evaluating all atomic configurations within the last 20 ps of each simulation. A very descriptive approach to characterize structural properties is given by partial radial distribution functions. They represent the likelihood g_{ij} to find a specific pair of atoms i and j at a distance r for each step:

$$g_{ij}(r)=\frac{1}{c_i c_j \varrho_0 N}\left(\sum_{a=1}^{N_i}\sum_{b=1}^{N_j}\delta\left(r-(r_a-r_b)\right)\right) \qquad (16)$$

In this equation, N is the total number of atoms, ϱ_0 the atomic number density, c_i the concentration of atom type I, and N_i the number of atom type i. r_a and r_b are atomic position vectors of atoms a and b, r is a distance vector of a specific length and δ is the Kronecker delta. Mean structural information can be obtained by averaging the partial radial distribution functions over the relevant time span. The average coordination number of atom type i by j is determined by integrating $g_{ij}(r)$ in between 0 and a cut-off, conventionally the first minimum r_{min}. The most probable bond length $\hat{r}$ is given by the first maximum

of $g_{ij}(r)$. The mean bond length $\bar{r}$, as also is referred to as R in EXAFS analysis, is defined by:

$$\int_0^{\bar{r}} g_{ij}(r)dr = \int_{\bar{r}}^{r_{min}} g_{ij}(r)dr \qquad (17)$$

Due to the asymmetric character of the distribution with tailing out to long distances, $\hat{r}$ is smaller than the average bond distance $\bar{r}$.

For each simulation run, the partial pair distribution functions $g_{X1X2}(r)$, with $X_{1/2}$ = Y, Sr, Si, Al, Na, Ca, C, or O, were extracted. They are given in Appendix 2 to 4. Appendix 5 presents the corresponding cut-off values as defined by the first minimum r_{min}. Additional structural information can be derived by evaluating the second shell around a cation, i.e. their closest cation neighbors (Appendix 6). They are defined by a distance to the central cation, which is below the sum of the element specific cut-off values of the central atom and the cation in question. In an additional approach, an algorithm was developed to investigate the coordination environment of Y, Sr and C in detail. The method distinguishes between different oxygen species in the vicinity of specific elements: bridging oxygen (between Si-Si, Si-$^{[4]}$Al, $^{[4]}$Al-$^{[4]}$Al as $BO_{Si\text{-}Si}$, $BO_{Si\text{-}Al}$ or $BO_{Al\text{-}Al}$), non-bridging oxygen (adjacent to Si or $^{[4]}$Al as NBO_{Si} or NBO_{Al}), free oxygen (FO) or oxygen tri-clusters (TO). For computational reasons, the trajectories had to be sampled down to contain only 2000 steps, still covering the whole time period.

3 Results

3.1 Application of the novel pressure assembly design

A modified design of the pressure medium assembly used in the Paris-Edinburgh press allows for low content element transmission EXAFS at energies > 12500 eV (e.g. with 2 wt % Y_2O_3 or SrO and 3 wt % La_2O_3). Although an ideal absorption of 1 and edge-jump of 1 are not feasible using this set-up, sufficient edge-jumps of ~ 0.2 and total absorptions between 2 and 3 can be realized.

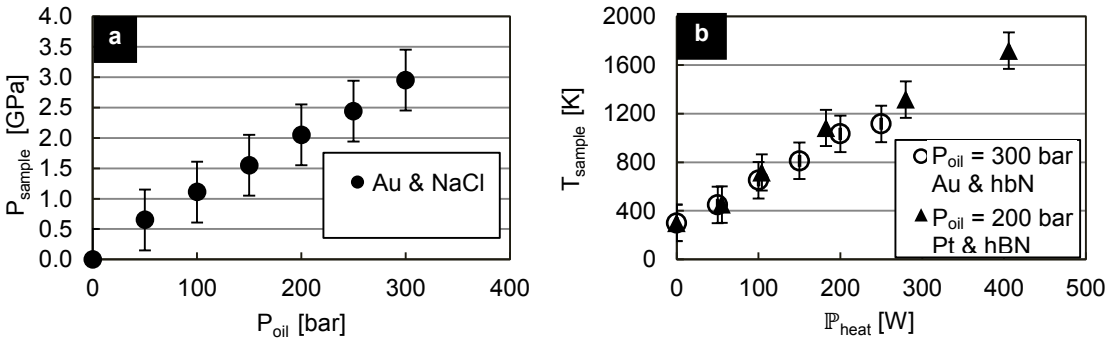

Figure 10: Pressure and temperature calibration of the modified pressure assembly design in the Paris-Edinburgh press.
(a) Pressure and (b) temperature calibration is based on XRD determined volumetric changes of reference materials (gold (Au), NaCl, hexagonal boron nitrite (hBN), and platinum (Pt), cf. chapter 2.1) at *HPHT* and solving their equation of states. Temperature calibration was conducted at a P_{oil} of 200 and 300 bar (P_{sample} of ~ 2 GPa and ~ 3 GPa).

The sample pressure P_{sample} is generated by the oil pressure P_{oil}, which is applied to the press. The new set-up was calibrated to sample pressures up to 3 GPa (corresponding to P_{oil} of 300 bar, Figure 10 a) at ambient temperature:

$$P_{sample}[GPa] \approx 0.01\ P_{oil}\ [bar] \qquad (18)$$

The sample temperature T_{sample} depends on the applied heating power $\mathbb{P}_{heat}$ and was calibrated up to ~ 1800 K (corresponding to $\mathbb{P}_{heat}$ ~ 400 watt, Figure 10 b). The temperature correlation is independent of the applied pressure of P_{sample} of 2 or 3 GPa (corresponding to P_{oil} of 200 or 300 bar, respectively):

$$T_{sample}[K] \approx 3.72 + 273 * \mathbb{P}_{heat}[W] \quad (19)$$

The set-up was successfully tested up to ~ 2000 K at 2.5 GPa as extrapolated from the calibration in eq. 19 (Pohlenz et al., 2016).

3.2 Chemical composition of glass and melt samples

Details on the chemical composition of all investigated samples can be found in Table 4. These data are derived from electron microprobe analysis, except for carbonate samples that were not quenchable to a homogeneous glass. Nominal compositions are given in these cases. Silicate glass samples (*sSA* and *sNC*) contain trace element contents of Y_2O_3, SrO and La_2O_3 around 0.5 wt %, while silicate and carbonate *in-situ* melt samples contain 1.2 to 2 wt % Y_2O_3 or SrO or 3 to 6 wt % La_2O_3. Additionally, B_2O_3 contaminations (cf. chapters 2.1 and 2.2.3) were detected of around 2 wt % in all *in-situ* melt samples, exceptionally exceeding 10 wt % (cf. samples Y & Sr P28c and La P40c in Table 4). The difference to 100 wt % in the derived totals may be caused by: (1) Undetermined amounts of volatiles, such as H_2O or CO_2 (accidentally attracted during sample synthesis or during the *in-situ* runs), (2) too low contents of Na_2O depending on incident beam current density and/or total Na content (Morgan and London, 1996). However, the low standard deviation within each sample analysis suggests chemically homogeneous samples. Backscattered electron images provide no signs of crystallization or bubble nucleation in glass samples up to 4.5 wt % CO_2 at 0.7 GPa / 6.0 wt % at 1.5 GPa in *sSA* composition as well as up to 7.6 wt % CO_2 at 0.7 GPa in *sNC* composition. These values are well within the composition- and pressure-dependent CO_2-solubility limits reported in

Table 4: Chemical composition of *ex-situ* glass samples and quenched *in-situ* samples.
The composition in wt % was determined by electron microprobe analysis (unless indicated otherwise). *CAR* compositions (with > 34 wt % CO_2) of the *in-situ* runs did not quench to glasses and compositional analyses was not feasible. Volumes of glass samples synthesized in piston cylinder experiments and quenched *in-situ* samples were too small for analyzing the CO_2 content. The standard deviation is given in parentheses and refers to the last printed digit.

	[wt %]	SiO_2	Al_2O_3	CaO	Na_2O	Y_2O_3	SrO	Rb_2O*	B_2O_3	EMPA Total	CO_2[c]	H_2O**	Total	ASI[a]
Sample[s]														
Y & Sr glasses	sSA0.0c	57.4(2)	9.9(1)	8.4(1)	22.8(2)	0.64(4)	0.53(3)	0.54(3)		100.1(3)	0.0(1)		100.1	0.19
	sSA0.2ch	56.9(2)	9.6(1)	8.1(1)	22.1(2)	0.62(4)	0.52(3)	0.54(3)		98.3(4)	0.2(1)	1.8(1)	100.3	0.19
	sSA0.7c	57.9(3)	9.9(1)	8.3(1)	22.7(2)	0.58(3)	0.49(3)	0.51(3)		100.3(3)	0.7(1)		101.1	0.19
	sSA1.5c	57.4(2)	10.0(1)	8.3(1)	22.6(2)	0.67(3)	0.57(4)	0.49(4)		100.0(3)	1.5(1)		101.5	0.19
	sSA2.1c	57.6(2)	10.0(1)	8.2(1)	22.3(2)	0.52(3)	0.42(3)	0.44(4)		99.4(3)	2.1(2)		101.5	0.19
	sSA2.4ch	55.7(2)	9.5(1)	8.0(1)	21.6(2)	0.56(3)	0.47(3)	0.49(4)		96.4(4)	2.4(1)	1.9(1)	100.7	0.19
	sSA3.8c	54.3(6)	9.7(2)	7.9(1)	19.7(2)	0.57(4)	0.44(5)	0.47(3)		93.1(6)	3.8(1)		96.9	0.21
	sSA3.9c	57.7(2)	10.0(1)	8.1(1)	21.5(2)	0.53(3)	0.00(0)	0.00(0)		97.8(3)	3.9(1)		101.6	0.20
	sSA6.0c	56.8(11)	10.2(2)	6.7(3)	17.9(9)	0.49(4)	0.35(5)	0.42(4)		92.9(11)	6[n]		98.9	0.24
	sNC0.8c	42.7(4)	8.2(2)	13.1(1)	30.2(3)	0.76(7)	0.61(5)	0.30(4)		95.8(5)	0.8(1)		96.6	0.11
	sNC5.0c	41.2(3)	7.8(2)	12.4(1)	28.9(4)	0.64(7)	0.51(5)	0.27(3)		91.7(4)	5.0(2)		96.7	0.11
Y & Sr in-situ	P00c	58.8(10)	10.7(3)	7.9(3)	19.4(2)	1.65(5)	1.33(4)		0.5(5)	100.2(10)	0[n]		100.2	0.23
	P05c	54.8(10)	9.9(3)	8.1(3)	18.3(4)	1.65(8)	1.21(4)		1.3(3)	95.3(17)	5[n]		100.3	0.22
	P10c	46.2(5)	8.1(2)	9.1(2)	19.5(2)	2.01(6)	1.29(4)		2.8(3)	89.0(6)	10[n]		99.0	0.17
	P28c	22.3(9)	5.0(5)	14.8(8)	19.6(6)	1.9(3)	0.73(5)		10.0(3)	74.4(14)	27.5[n]		103.0	0.09
	P35c	6.2[n]	1.1[n]	14.7[n]	39.6[a]	2.0[n]	1.8[n]				34.6[n]		100.0[n]	0.01
	P39c	1.6[n]	0.3[n]	14.9[n]	40.4[a]	2.0[n]	1.8[n]				39.0[n]		100.0[n]	0.00
	P41c	0.0[n]	0.0[n]	15.1[n]	40.7[a]	1.8[n]	1.7[n]				40.7[n]		100.0[n]	0.00
						La_2O_3	Nb_2O_5							
La glasses	sSA00c	57.5(4)	10.1(1)	8.1(1)	22.9(4)	0.5(2)	0.60(6)			99.7(9)	0.2(1)		99.9	0.19
	sSA00ch	55.7(5)	9.8(1)	7.9(1)	22.0(3)	0.5(2)	0.71(4)			96.7(6)	0.3(1)	1.9(1)	99.0	0.19
	sSA02c	56.2(4)	9.8(2)	8.1(1)	22.4(4)	0.5(2)	0.64(5)			97.6(8)	1.85(4)		99.4	0.19
	sSA02ch	54.7(6)	9.5(2)	8.0(2)	21.6(3)	0.5(2)	0.64(5)			94.9(9)	2.27(6)	2.0(1)	99.2	0.19
	sSA04c	54.7(6)	9.6(1)	7.9(1)	21.5(3)	0.3(1)	0.54(4)			94.7(8)	4.37(3)		99.0	0.19
	sNC00c	42.7(7)	7.6(1)	12.0(2)	28.4(15)	2.5(2)				93.2(9)	0[n]		93.2	0.11
	sNC03c	44.4(4)	7.9(2)	12.5(4)	29.8(6)	0.5(1)	0.72(4)			95.8(11)	3.1(7)		98.9	0.11
	sNC06c	43.5(5)	7.7(1)	11.7(1)	26.2(4)	0.4(2)	0.62(4)			90.3(9)	6.4(5)		96.7	0.12
	sNC08c	42.3(4)	7.5(1)	12.0(1)	28.9(9)	0.6(2)	0.78(4)			92.0(9)	7.6(2)		99.6	0.11
La in-situ	PsSA00c	54.9(4)	9.9(1)	7.8(2)	20.5(4)	4.8(3)			1.1(11)	99.0(12)	0[n]		99.0	0.21
	PsSA05c	52.4(6)	9.4(2)	7.5(2)	21.1(3)	2.7(2)			1.3(8)	94.4(11)	5[n]		99.4	0.19
	PsNC00c	36.2(5)	6.7(1)	9.2(3)	24.6(4)	3.6(3)			6.6(11)	86.9(16)	0[n]		86.9	0.12
	PsNC10c	45.7(6)	8.7(3)	6.7(2)	20.3(6)	2.1(2)			1.0(10)	84.6(15)	10[n]		94.6	0.19
	P35c	6.4[n]	1.2[n]	14.8[n]	39.9[n]	3.0[n]			2.1(18)[e]		34.7[n]		100.0[n]	0.01
	P39c	1.6[n]	0.3[n]	15.1[n]	40.7[n]	3.0[n]			2.5(11)[e]		39.3[n]		100.0[n]	0.00
	P40c	0.0[n]	0.0[n]	14.7[n]	39.7[n]	6.0[n]			11.6(83)[e]		39.6[n]		100.0[n]	0.00

[s] the sample names represent a code, which indicates following sample specifications: Letters - experimental runs on glasses (of *sSA* or *sNC* compositions) or conducted *in-situ* with the Paris-Edinburgh press (P); Digits - the carbon content; an additional h identifies H_2O-bearing samples. An example: PsSA05c represents a sample, used for *in-situ* measurement in the press of *sSA* composition with 5 wt% CO_2.

[c] CS analyser, [n] given as nominal according to starting composition, [e] EMPA measured boron is roughly estimated by averaging individual boron concentrations of the different carbonate mineral quench products and excluded in the total sum.

[a] aluminum saturation index (ASI, defined as the molar ratio of $Al_2O_3/(Na_2O+K_2O+CaO)$).

* Rb and Nb in some of the glass samples were not further investigated for this study.

literature (e.g. Ni and Keppler, 2013a). The images also proofed that silicate *in-situ* run products quenched to homogeneous glasses (exemplary depicted by Figure 11 a).

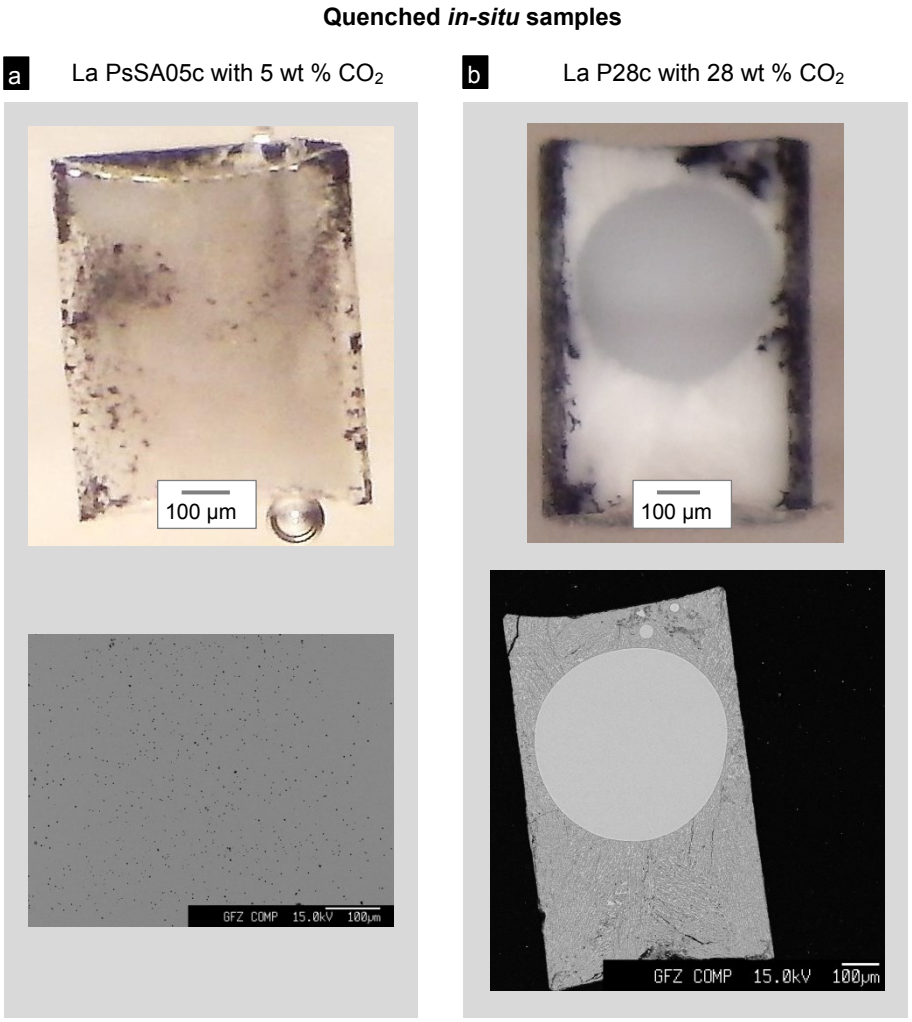

Figure 11: Photographs (top) and backscattered electron images (bottom) of quench products from *HPHT* runs.
(a) Typical glass of quenched *in-situ* low-carbonate silicate melt samples (exemplary depicted by La *sSA05* with 5 wt % CO_2). It shows some bubbles as a result of quenching. (b) Quench product of immiscible silicate (glassy drop) and carbonate (microcrystalline intergrowth texture) melt of La bearing sample with 28 wt % CO_2, excluded from further analysis. Both photographs at the top show a clear contamination of graphite at the rims.

Although pressure and temperature conditions were chosen to prevent the carbonated silicate melt from unmixing, the La sample with 28 wt % CO_2 showed liquid immiscibility: a glassy droplet of quenched silicate melt in the center surrounded by quenched intergrown microcrystalline carbonates (Figure 11 b). Liquid immiscibility is very sensitive to the exact chemical composition. Slight chemical variations in the starting materials, e.g. by accidentally trapped H_2O or the relatively enhanced content of La_2O_3, are likely triggers for the prevalent immiscibility. The grain sizes of the recovered materials are too small for electron microprobe phase identification in the complex Na-Ca-carbonate system (Shatskiy et al., 2013, 2015). The sample with liquid immiscibility was excluded from further structural analysis, as the measured EXAFS is composed of indeterminable contributions of La in the silicate or carbonate compartment. All quench products show pronounced rims of graphite aggregates (Figure 11 a, b, top). Possibly, they stem from interactions with the carbon bearing parts of the pressure assembly. Quenched *in-situ* samples of silicate compositions with ≥ 5 wt % CO_2 show increasing signs of CO_2 degassing in form of quenched bubbles (cf. Figure 11 a). The degassing was likely triggered through temperature and pressure release after the *in-situ* run.

3.3 X-ray absorption fine structure (XAFS)

3.3.1 X-ray absorption near edge structure (XANES)

Y, La and Sr K-edge XANES spectra of model compounds as well as from selected *in-situ* melts at *HPHT* and their glassy quench products at *HP* are presented in Figure 12. Roman numbers in the figure indicate features, which are described in the following. The maximum of the Y K-edge (Figure 12 a) consists of two features, particularly noticeable for the model compound Y_2O_3 (I). The first EXAFS of Y_2O_3 possesses a pronounced fine structure on the low-energy limb (II). The quenched *in-situ* samples show a distinct change in the main-edge (I) from CO_2-free *sSA* composition, with the second feature as prominent peak, to the 28 wt % CO_2 bearing composition, with the first as prominent peak. In Y bearing *HPHT in-situ* melts the second feature is generally reduced to a shoulder, again diminishing in intensity when comparing CO_2-free *sSA* and silicate-

free *CAR41* composition. All spectra of the La K-edge are relatively similar. They show only weakly developed features due to the strong core-hole lifetime broadening. Particularly the spectral features of the *HPHT in-situ* melts become fairly weak. In case of Sr (Figure 12 c), $SrCO_3$ with Sr in 9-fold coordination shows a quite narrow main-edge maximum (III), followed by a relative intense first EXAFS (IV) exhibiting considerable fine structure between 16130 and 16145 eV. In contrast, the main-edge maximum (III) of the quenched *in-situ* sample is wider with an additional shoulder on the high-energy limb (V). The first EXAFS (IV) maximum is shifted to higher energy compared to $SrCO_3$ for all melts and quenched *in-situ* samples. The main-edge maximum (III) becomes wider and more asymmetric at *HPHT* conditions, especially in case of the CO_2-free melt.

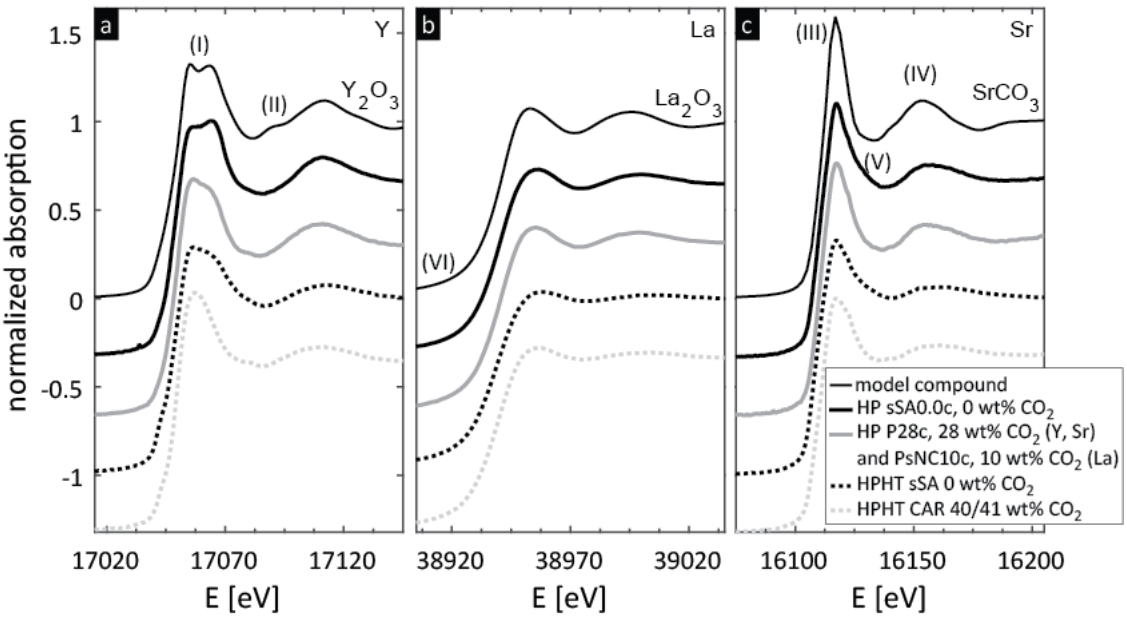

Figure 12: Normalized Y, La and Sr K-edges XANES
Model compounds are represented with thin lines and selected *in-situ* melts at *HPHT* and glassy, quenched *in-situ* samples at *HP* with thick lines. At *HP* conditions (solid lines), the K-edges of 0 and 10 or 28 wt % CO_2 bearing glasses are plotted; at *HPHT* conditions (dotted lines), the K-edges of pure silicate and pure carbonate melts are plotted. The flattening of the pre-edge of the La XANES (VI) is relatively long due to its large core-hole lifetime and would be seen in an enlarged E range. Further spectral features indicated with roman numbers are described in the text.

3.3.2 EXAFS of model compounds

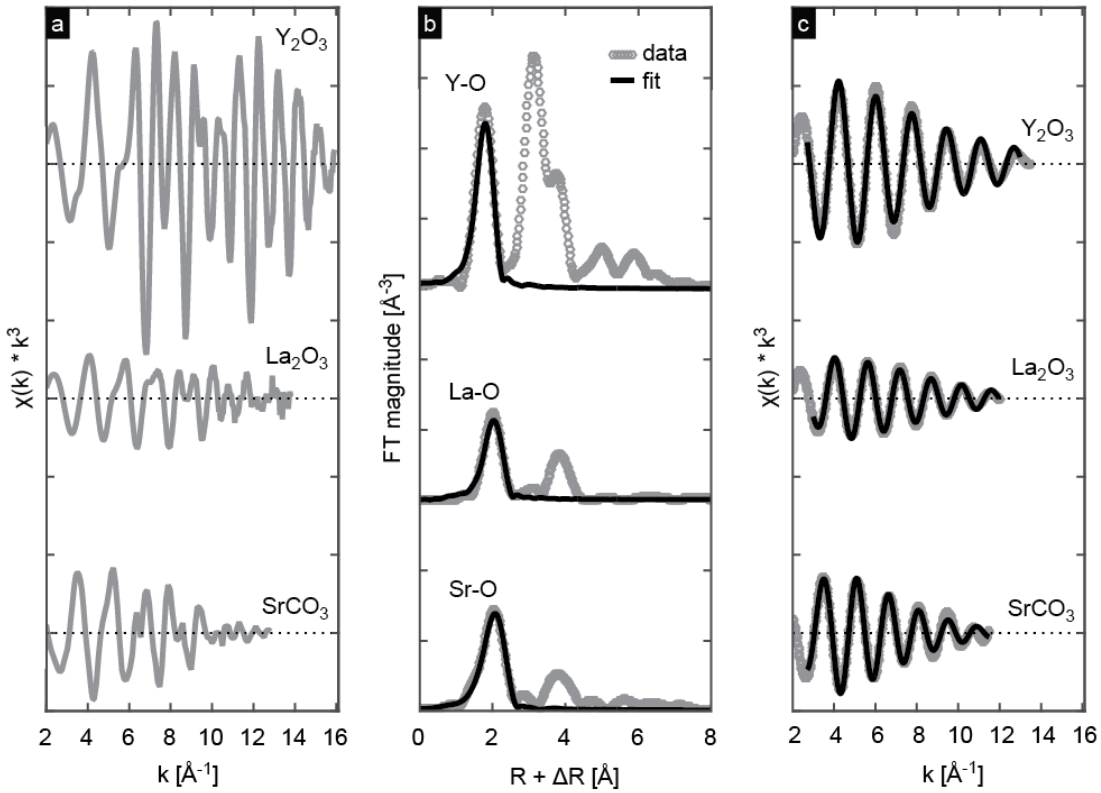

Figure 13: Y, La and Sr EXAFS and their Fourier transforms in model compounds.
(a) K-edge EXAFS of Y, La and Sr in model compounds. (b) Magnitudes of the Fourier transforms (FT) of the EXAFS and respective fits. Distances of the FT are not corrected for the phase shift introduced at the scattering event. This is accounted for by the term ΔR. (c) Fourier filtered first shell oxygen EXAFS signals of indicated model compounds and corresponding fits.

EXAFS spectra of model compounds (Y_2O_3, La_2O_3, $SrCO_3$) showed strong oscillations up to a k of 16 $Å^{-1}$ for Y, 12 $Å^{-1}$ for La and 11 $Å^{-1}$ for Sr (Figure 13 a). Fourier filtering of the first shell oxygen signal (as represented in Figure 13 b) reduced the evaluable signal length down to 11 or 13 $Å^{-1}$ (Figure 13 c), due to windowing effects. Fit ranges were adopted to reach sufficient signal length to independently fit the five parameters of N, R, σ^2, h and ΔE_0 according to the procedure explained in chapter 2.3.2.2. The corresponding single shell fits agree well with the Fourier filtered EXAFS (Figure 13 c) and also as Fourier transforms with the first shell of the Fourier-transformed unfiltered EXAFS (Figure 13 b). The difference in height of the 1st shell maximum between the Fourier

Transforms and the fits is explained by a windowing effect induced during 1st shell filtering, that used relative narrow limits to only include 1st shell contributions. Derived fit parameters (Table 5) are consistent with published X-ray diffraction data (Table 1, references therein) and EXAFS data on Y_2O_3 (Simon et al., 2013), La_2O_3 (Ali et al., 1997), and $SrCO_3$ (O'Day et al., 2000).

Table 5: Y, Sr, La K-edge EXAFS local structure parameters in model compounds.
Results of N, R σ^2 and h [a] do not depend on k-weighting within the range of errors and are in good agreement with diffraction and further EXAFS data (cf. text for references). Parameters in bold (S_0, ΔE_0) will be used in subsequent EXAFS fits of glass and melt samples (for Y as taken from χk^3, for La and Sr as taken from χk^2). Standard deviation in parentheses refers to last printed digit.

	Y-O in Y_2O_3		La-O in La_2O_3		Sr-O in $SrCO_3$	
fit range	2.7 – 13 Å^{-1}		3-12 Å^{-1}		2.7 – 11.7 Å^{-1}	
k-weighing	χk^2	χk^3	χk^2	χk^3	χk^2	χk^3
parameters[a]						
S_0	0.94	**0.94**	**0.94**	0.94	**0.98**	0.98
N	5.8(3)	6.2(5)	8.1(7)	7.6(5)	9.4(5)	9.0(8)
R [Å]	2.293(5)	2.28(1)	2.60(3)	2.58(2)	2.60(1)	2.602(8)
σ^2 [Å^{-2}]	0.005(3)	0.006(3)	0.004(2)	0.006(1)	0.01(1)	0.012(4)
h [Å^{-1}]	0.0(3)	0.02(4)	0.05(2)	0.04(1)	0.0(3)	0.0(4)
ΔE_0 [eV]	1.9(3)	**1.1(8)**	**-0.1(9)**	-0.9(8)	**-2.6(5)**	-2.5(6)

[a] S_0: Amplitude reduction factor, N: Coordination number, R: average bond length, σ^2: Debye-Waller-factor, h: asymmetry parameter, ΔE_0: E_0 edge shift. For further details refer to chapter 2.3.

3.3.3 EXAFS of glass and melt samples

All results of the EXAFS fits of glass and melt samples are given in Table 6, while element specific data are shown in Figure 14 to Figure 16 for Y, La and Sr, respectively. Due to their configurational disorder, EXAFS spectra of glass samples and quenched *in-situ* samples show shorter refineable k-ranges compared to model compound spectra. Significant oscillations in these glasses reach up to a k of 13 Å^{-1} (Y, La) or 10 Å^{-1} (Sr). Spectra of *in-situ* experiments exhibit distinctively reduced amplitudes to about half of that of the corresponding

Table 6: Y, La and Sr K-edge EXAFS local structure parameters of glass samples, *in-situ* melt samples *at HPHT* and their quench products at *HP*.
Fixed parameters: S_0 as determined by model compound fits, σ^2 and h as derived through the preliminary fit procedure (cf. chapter 2.3.2.3). During that procedure the parameter ΔE_0 derived from model compounds was slightly refined. N is positively correlated to R as explained in chapter 2.3.2.2. Calculated bond strengths s are in italic. Standard deviations of EXAFS measurements in parentheses refer to the last printed digit.

		Y S_0=0.94 ΔE_0=1.5 eV			**Sr** S_0=0.98 ΔE_0=-2.5 eV				**La** S_0=0.94 ΔE_0=-0.5 eV		
	σ^2 [Å^{-2}]	0.003			0.011				0.003		
	h [Å^{-1}]	0.05			0.07				0.09		
		R [Å]	**N**	***s [vu]***	**R [Å]**	**N**	***s [vu]***		**R [Å]**	**N**	***s [vu]***
glass	sSA0.0c	2.29(1)	6.3	*0.47*	2.53(1)	6.0	*0.33*	sSA00c	2.52(1)	7.7	*0.39*
	sSA0.2ch	2.29(1)	6.3	*0.48*	2.53(1)	6.1	*0.33*	sSA00ch	2.53(1)	8.0	*0.38*
	sSA0.7c	2.29(1)	6.3	*0.47*	2.53(1)	6.1	*0.33*	sSA02c	2.53(1)	7.9	*0.38*
	sSA1.5c	2.29(1)	6.3	*0.47*	2.53(1)	6.1	*0.33*	sSA02ch	2.54(1)	8.1	*0.37*
	sSA2.1c	2.29(1)	6.3	*0.47*	2.53(1)	6.2	*0.33*	sSA04c	2.54(1)	8.0	*0.37*
	sSA2.4ch	2.29(1)	6.3	*0.47*	2.54(1)	6.3	*0.32*	sNC00c	2.53(1)	8.0	*0.38*
	sSA3.8c	2.29(1)	6.4	*0.47*	2.55(1)	6.4	*0.31*	sNC03c	2.54(1)	8.1	*0.37*
	sSA3.9c	2.29(1)	6.3	*0.47*	-	-	-	sNC06c	2.54(1)	8.0	*0.37*
	sSA6.0c	2.30(1)	6.4	*0.47*	2.57(1)	6.9	*0.29*	sNC08c	2.53(1)	8.0	*0.38*
	sNC0.8c	2.29(1)	6.4	*0.47*	2.55(1)	6.4	*0.31*				
	sNC5.0c	2.29(1)	6.4	*0.47*	2.55(1)	6.5	*0.31*				
quenched in-situ (HP)	P00c	2.29(1)	6.3	*0.48*	2.52(1)	5.9	*0.34*	PsSA00c	2.53(1)	7.8	*0.39*
	P05c	2.29(1)	6.3	*0.48*	2.54(1)	6.3	*0.32*	PsSA05c	2.53(1)	7.9	*0.38*
	P10c	2.29(1)	6.3	*0.47*	2.58(1)	7.0	*0.29*	PsNC00c	2.54(1)	8.1	*0.37*
	P28c	2.31(1)	6.7	*0.45*	2.55(1)	6.5	*0.31*	PsNC10c	2.55(1)	8.3	*0.36*
	σ^2 [Å^{-2}]	0.004			0.011				0.003		
	h [Å^{-1}]	0.13			0.17				0.16		
		R [Å]	**N**	***s [vu]***	**R [Å]**	**N**	***s [vu]***		**R [Å]**	**N**	***s [vu]***
in-situ (HPHT)	P00c	2.37(1)	7.6	*0.40*	2.60(1)	7.0	*0.29*	PsSA00c	2.55(1)	8.0	*0.38*
	P05c	2.36(1)	7.5	*0.40*	2.61(2)	7.1	*0.28*	PsSA05c	2.57(1)	8.5	*0.36*
	P10c	2.36(1)	7.5	*0.40*	2.61(1)	7.1	*0.28*	PsNC00c	2.57(1)	8.5	*0.35*
	P28c	2.38(1)	7.8	*0.39*	-	-	-	PsNC10c	2.58(1)	8.6	*0.35*
	P35c	2.40(1)	8.1	*0.37*	2.64(1)	7.6	*0.26*	P35C	2.58(1)	8.8	*0.34*
	P39c	2.41(1)	8.3	*0.36*	2.64(2)	7.6	*0.26*	P39C	2.60(1)	9.2	*0.33*
	P41c	2.41(1)	8.5	*0.35*	2.64(1)	7.7	*0.26*	P40C	2.59(1)	9.1	*0.33*

glasses. This is due to the enhanced thermal and configurational disorder in melts and results in drastically shortened signal length with significant EXAFS oscillations only up to a k of 8.5 Å^{-1} (Y, La) or 7 Å^{-1} (Sr). Particularly, Sr K-edge melt spectra are of poor quality. A likely cause is its tendency to create ionic bonds, which only show relatively weak cation-ligand correlations (Penner-Hahn, 2005). In the EXAFS of all elements, a minor multi-electron excitation features at ~ 7 Å^{-1} was observed (cf. to Y K-edge EXAFS of Simon, 2016). Due to

the reduced EXAFS range and low signal-to-background ratio, this feature could not be corrected for (Bunker, 2010). Although this effect may introduce a slight systematic error to the data analysis, mainly leading to an underestimation of the coordination number (D'Angelo et al., 1996), the relative trends are not affected. All fits were applied over the maximum possible fit ranges and the consistency of the derived values was confirmed by additionally fitting all spectra over the corresponding short range of *in-situ* data at *HPHT*. It has to be noted that depending on the N-R-correlation applied in the fit model (cf. chapter 2.3.2.2), the coordination number N follows closely each observed trend of the bond length R.

Y K-edge EXAFS

Normalized Y K-edge EXAFS spectra and corresponding fits of all investigated samples are shown in Figure 14 a. Derived values of $R_{Y\text{-}O}$ are shown in Figure 14 b for glass samples and in Figure 14 c for *in-situ* melt samples and their quench products. For all water-free and water-bearing *sSA* and *sNC* glasses with CO_2 contents up to 6 wt %, fitted $R_{Y\text{-}O}$-values are invariable at ~ 2.29 Å within the errors. For *in-situ* melt samples, a common $R_{Y\text{-}O}$ of ~ 2.37 Å is found for all silicate compositions, whereas the quench products show a value of ~ 2.29 Å. *In-situ* melt samples with CO_2 concentrations > 34 wt % show a small but systematic increase in $R_{Y\text{-}O}$ up to 2.41 Å for the highest CO_2 concentration. Despite its boron contamination, the sample at 28 wt % CO_2 falls in line with this trend.

La K-edge EXAFS

Figure 15 shows k^2-weighted La K-edge spectra and fits (a) as well as derived values for $R_{La\text{-}O}$ in glass (b) and *in-situ* melt samples and their quench products (c). $R_{La\text{-}O}$ in water-free *sSA* glass samples increases from 2.52 Å to 2.54 Å with increasing CO_2 content (Figure 15 b, dark triangles). The water-bearing *sSA* glass samples show slightly increased bond lengths compared to their water-free counterparts (Figure 15 b, blue stars). On the other hand, all $R_{La\text{-}O}$ in *sNC*

glass samples are slightly higher compared to bond length of Y-O at ~ 2.54 Å, unaffected by CO_2 content (Figure 15 b, light triangles). Consistently, in quenched melts and in *in-situ* melts (Figure 15 c, diamonds and circles, respectively) the carbon-free *sNC* samples also show an increase in bond length compared to the carbon-free *sSA* samples. The *in-situ* melt samples are shifted to higher $R_{La\text{-}O}$ in total. *CAR* compositions reach $R_{La\text{-}O}$ of up to 2.60 Å. Note, that the pure carbonate sample was highly contaminated by B_2O_3 (exceeding 10 wt %).

Sr K-edge EXAFS

k^2-weighted Sr K-edge spectra and fits as well as derived $R_{Sr\text{-}O}$ for glass and *in-situ* samples are shown in Figure 16. $R_{Sr\text{-}O}$ values of *sSA* glasses (Figure 16 b, dark triangles) increase with CO_2 content from 2.53 Å to 2.57 Å. Water-bearing *sSA* glasses appear to show slightly increased bond length compared to water-free *sSA* glasses. $R_{Sr\text{-}O}$ values of *sNC* glasses remain at 2.55 Å, unaffected by CO_2 content (Figure 16 b, lighter triangles). Consistently, quenched *in-situ* samples show an increase in $R_{Sr\text{-}O}$ from 2.52 to 2.58 Å with CO_2 content. *In-situ* melt samples on the other hand show only a slight increase from 2.60 to 2.61 Å up to 10 wt % CO_2, only to sharply increase at higher carbonate contents, up to 2.64 Å in *CAR* compositions (Figure 16 c). The highly boron contaminated quenched *in-situ* sample at 28 wt % CO_2 does not fit in this trend, while the corresponding *in-situ* melt sample could not be analyzed due to extremely poor data quality[3].

[3] Most likely this is due to a continuously changing sample composition, triggered by an elemental exchange with the pressure assembly (cf. significant boron assimilation in Table 5). Accordingly, the ever changing absorption properties create very unstable conditions and inhibit reliable EXAFS measurements. Only after several hours (> 10 h) of equilibration at *HPHT*, an EXAFS spectrum could be recorded. Nonetheless, the signal was not analyzable in a physically reasonable manner. The melt quenched to a homogenous glass, albeit showing clear signs of decarbonization in form of numerous bubbles.

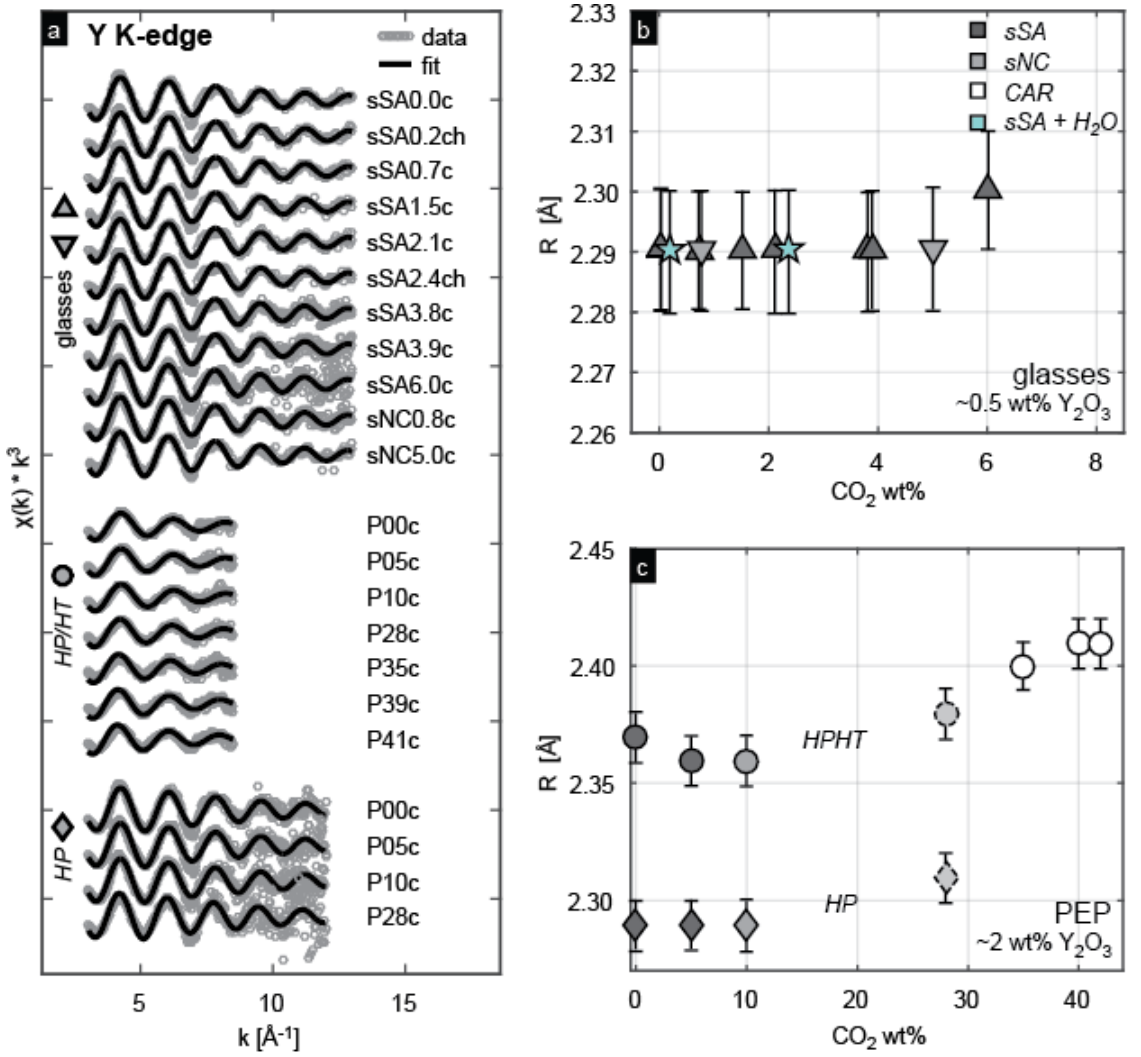

Figure 14: Evolution of Y K-edge EXAFS in glasses and melts.
(a) Normalized k^3-weighted Y K-edge EXAFS χ (k) and fits of glass samples, *in-situ* melt samples at *HPHT* and corresponding quenched *in-situ* samples at *HP*. Compositions range from CO_2-free silicate (*sSA* and *sNC*) to pure carbonate; with CO_2 contents as indicated by the digits in the sample name and h identifying H_2O-bearing samples (cf. Table 4). (b) Bond length $R_{Y\text{-}O}$ as a function of CO_2 content for glass samples and (c) for *in-situ* melt samples at *HPHT* (circles) and to glass quenched *in-situ* samples at *HP* (diamonds). Dashed marker lines indicate samples with high B contamination.

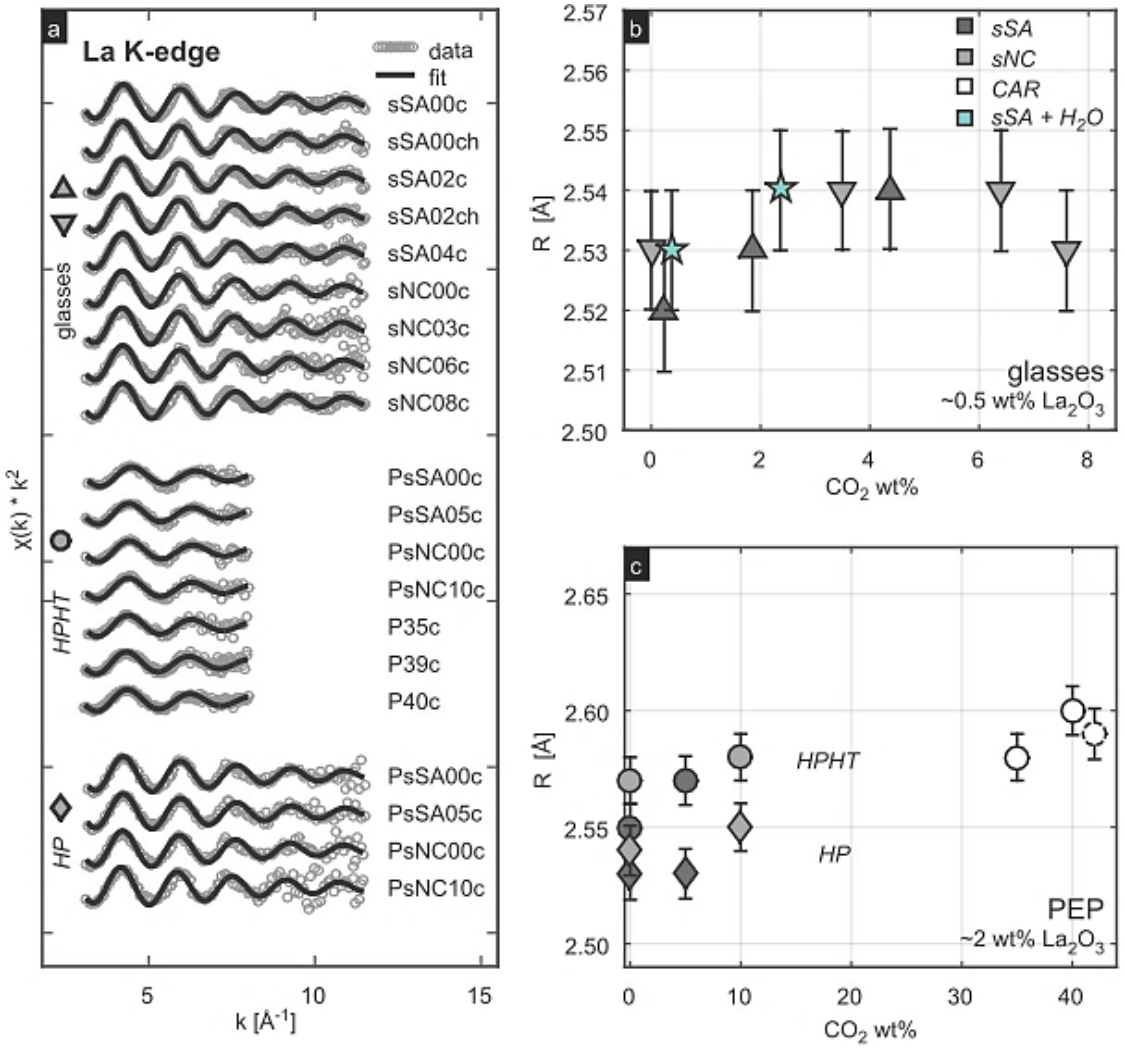

Figure 15: Evolution of La K-edge EXAFS in glasses and melts.
(a) Normalized k²-weighted La K-edge EXAFS χ (k) and fits of glass samples, *in-situ* melt samples at *HPHT* and corresponding quenched *in-situ* samples at *HP*. Compositions range from CO_2-free silicate (*sSA* and *sNC*) to pure carbonate; with CO_2 contents as indicated by the digits in the sample name and h identifying H_2O-bearing samples (cf. Table 4). (b) Bond length $R_{La\text{-}O}$ as a function of CO_2 content for glass samples and (c) for *in-situ* melt samples at *HPHT* (circles) and to glass quenched *in-situ* samples at *HP* (diamonds). Dashed marker lines indicate samples with high B contamination.

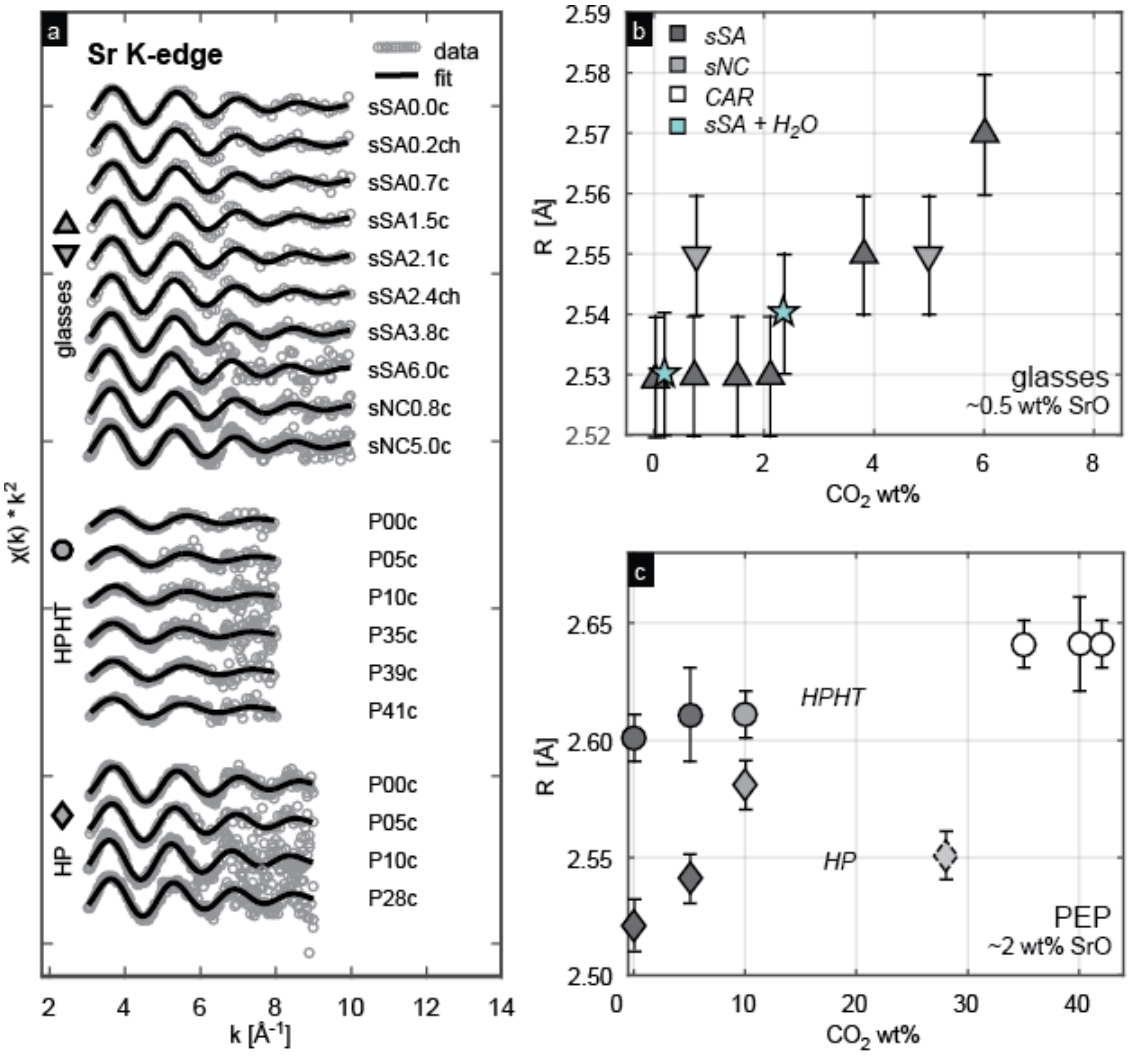

Figure 16: Evolution of Sr K-edge EXAFS in glasses and melts.
(a) Normalized k²-weighted Sr K-edge EXAFS χ (k) and fits of glass samples, *in-situ* melt samples at *HPHT* and corresponding quenched *in-situ* samples at *HP*. Compositions range from CO_2-free silicate (*sSA* and *sNC*) to pure carbonate; with CO_2 contents as indicated by the digits in the sample name and h identifying H_2O-bearing samples (cf. Table 4). (b) Bond length $R_{Y\text{-}O}$ as a function of CO_2 content for glass samples and (c) for *in-situ* melt samples at *HPHT* (circles) and to glass quenched *in-situ* samples at *HP* (diamonds). Dashed marker lines indicate samples with high with B contamination.

In H_2O-bearing *sSA* glasses, La-O and Sr-O bond lengths appear to be slightly increased compared to their H_2O-free counterparts. Since only two data points each are available and the observed shifts are within the error, further discussion would lack a significant basis. *In-situ* experiments show B_2O_3 contaminations of ~ 2 wt %, induced by the boron containing pressure assembly. This value was exceeded in two samples, in which B_2O_3 contents surpass 10 wt % (Table 4). In these experimental runs, metal – oxygen bond lengths tend to be lower than suggested by the overall observed trend. The comparably small boron groups (with B-O bond length 12 % shorter then Si-O) act as network formers, assumingly in roughly equal fractions of trigonal-planar $[BO_3]^{-3}$ and tetrahedral $[BO_4]^{-5}$ (cf. sample no. 54 in NMR studies of Martens and Müller-Warmuth, 2000; Navrotsky, 1996). The observed bond length anomaly cannot be resolved in detail within the scope of this study and effected samples are excluded from further investigation.

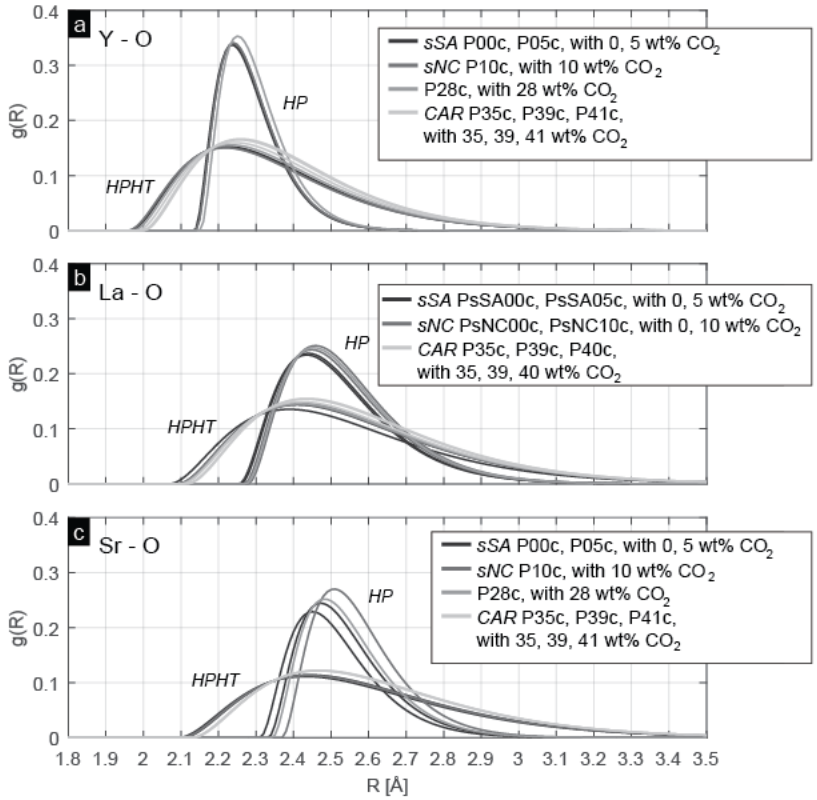

Figure 17: Fitted pair distribution functions of Y-O, La-O and Sr-O.
Fitted pair distribution functions p(r) of (a) Y-O, (b) La-O and (c) Sr-O for *in-situ* melt samples at *HPHT* and quenched *in-situ* samples at *HP*.

Figure 17 shows the fitted pair distribution functions, which prominently illustrate: (1) the enhanced asymmetric distributions found in the glasses of quenched *in-situ* samples (*HP*) and even more pronounced in *in-situ* melts (*HPHT*) and (2) the increasing trend of local disorder around the central atom along Y < La < Sr, expressed in increasing Debye-Waller factors σ^2 and asymmetry parameters h for Y, La and Sr (cf. Table 6).

3.4 Molecular dynamics simulations

3.4.1 Evaluation of the equilibration state

To ensure that information derived from MD trajectories is representative, one has to verify that the simulated system has reached an equilibrium state within the run time. One way of doing this is by demonstrating that structural parameters, such as coordination numbers or proportions of distinct oxygen species, are constant over the sampled time period. In the MD simulations of the silicate melts the fractions of specific oxygen species of bridging oxygens (BO), non-bridging oxygens (NBO) and free oxygens (FO) fluctuate relatively stable around stationary values over time (Figure 18). Striking is the irregular course in *sNC10* compositions, especially stressed by the fluctuations in the Sr melt towards the end of the run. In the quenched glasses, the evolution of the fractions of oxygen species is considerably erratic, with sudden jumps followed by regions of constant values over several time steps. Still, oxygen species fractions in glass runs show amplitudes similar to their melt counterparts and also fluctuate around a constant value. For carbonate melts, which are of ionic character, it is of no sense to define BO or NBO. Instead coordination numbers are regarded: C is constantly 3-fold coordinated, with 6 to 7 Na cations as 2nd shell neighbors.

Carbonate melts are generally non-quenchable. The simulation of the quench produced unphysical configurations, where all C atoms are in isolated positions, without any coordinating oxygens. Thus, the simulated carbonate quench products are excluded from further investigation.

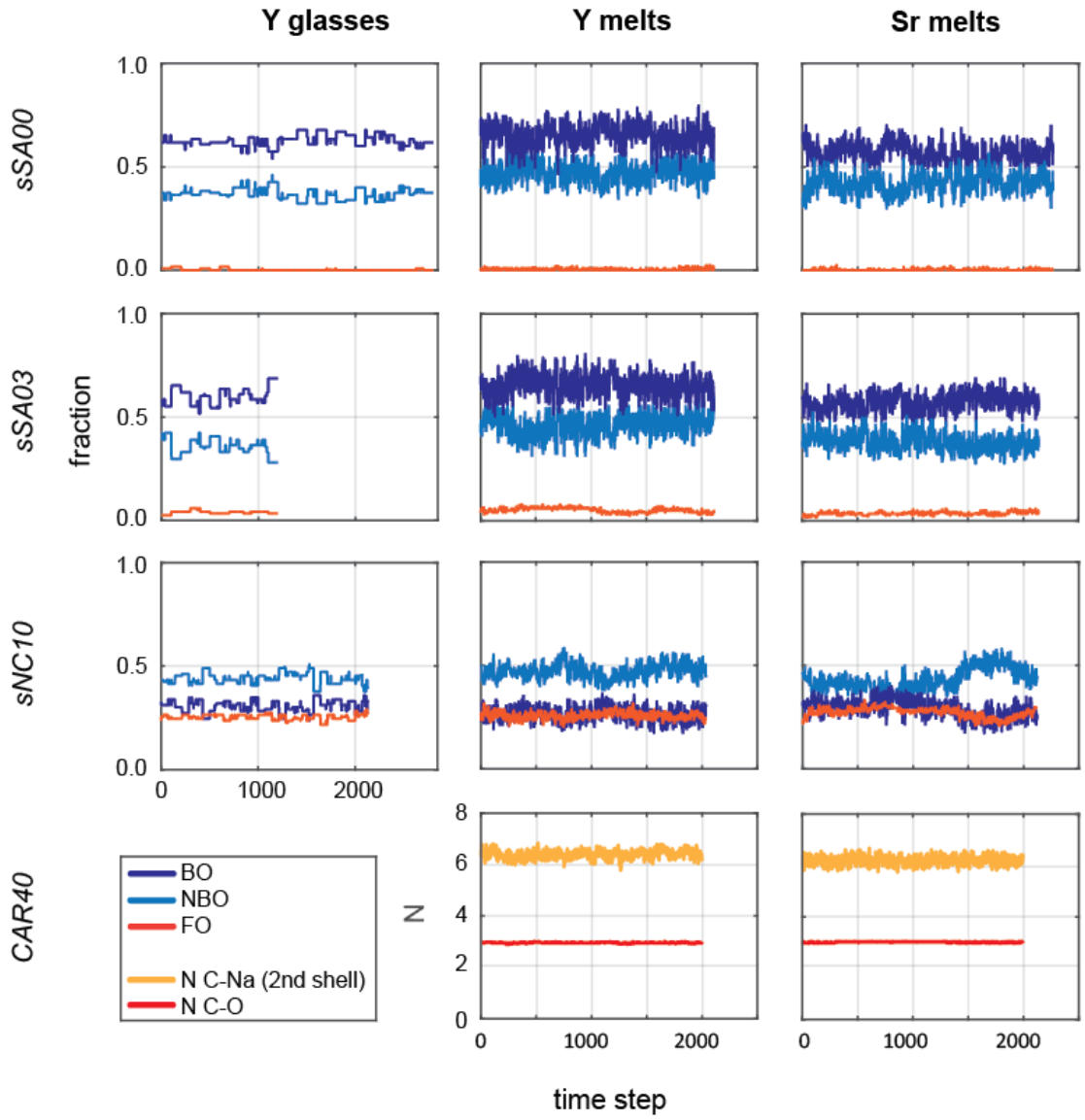

Figure 18: Time-dependent structural evolution in simulated glasses and melts.
Evolution of prevalent oxygen species as fractions of bridging oxygen (BO), non-bridging oxygen (NBO) and free oxygen (FO) in silicate compositions (*sSA00*, *sSA03*, *sNC10*) and of prevalent coordination numbers $N_{C\text{-}Na}$ of Na neighbors in the 2nd shell and $N_{C\text{-}O}$ of 1st shell oxygen neighbors around C in carbonate melts (*CAR40*).

3.4.2 General structural characteristics of simulated glasses and melts

The equilibration test already provides first insights into structural properties of the glasses and melts. A more detailed view on the proportions of oxygen species is presented in Figure 19 with focus on the network former type, Si or $^{[4]}$Al, adjacent to BO and NBO (cf. numeric values in the Appendix 7). Pure to low-

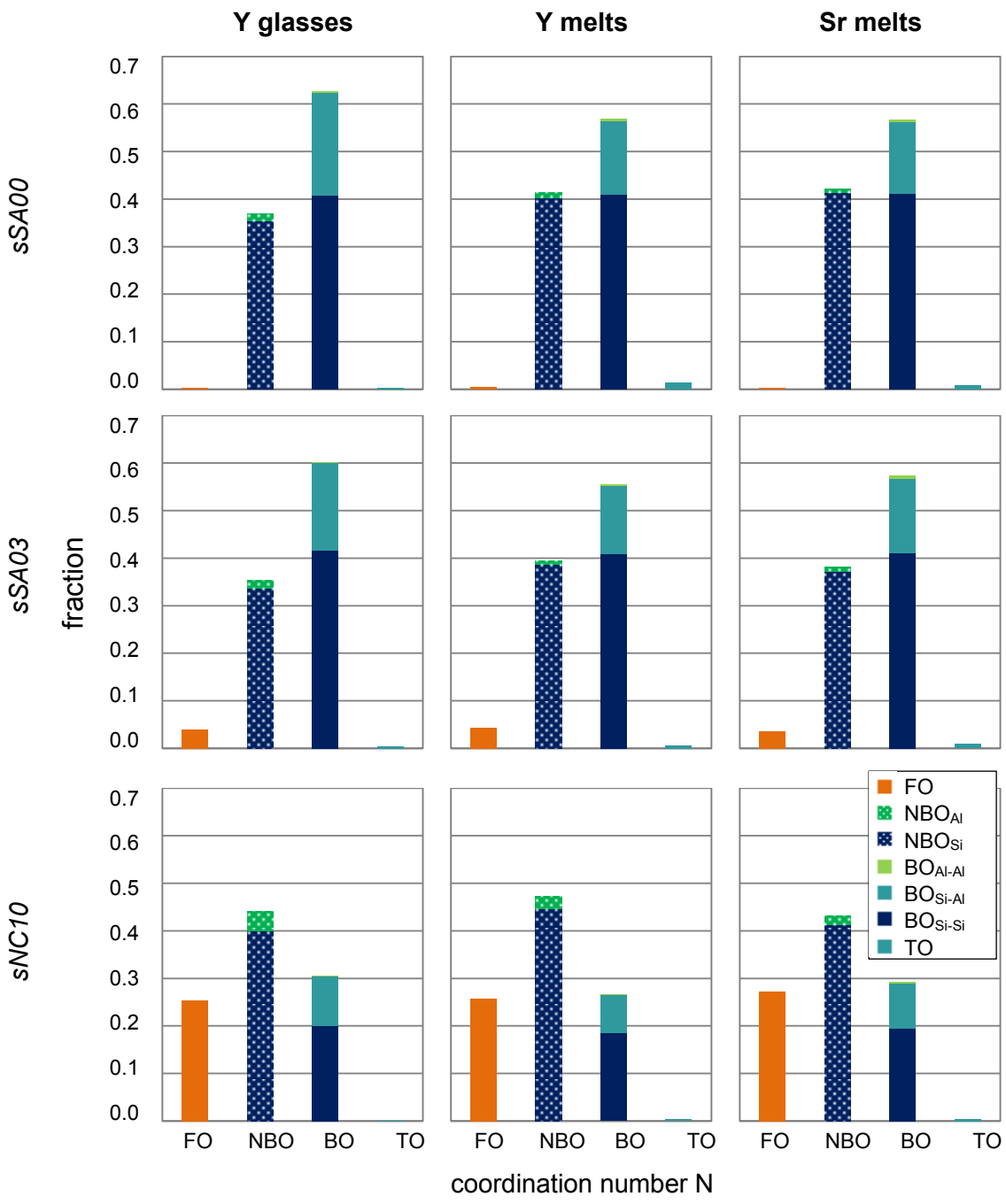

Figure 19: Proportions of oxygen species in silicate simulated glasses and melts.
Fractions of free oxygen (FO), non-bridging oxygen (NBO), bridging oxygen (BO) and tri-cluster oxygen (TO) in silicate glasses and melts: differentiated by involved network formers of $^{[4]}$Al and Si. Carbonate melts contain no NBO or BO.

carbonate silicate glasses and melts (*sSA00* and *sSA03*) contain similar fractions of NBO (~ 40 %) and BO (~ 60 %). Both oxygen species are mainly formed with Si: either as NBO coordinating an Si (NBO_{Si}) or as a BO in between two Si ($BO_{Si\text{-}Si}$), each prevalent with ~ 40 %. Approximately 15 – 20 % of the oxygens are $BO_{Si\text{-}Al}$ and only 4 % of the oxygens are NBO_{Al}. In *sNC10* composition, the dominant oxygen species is NBO (40 – 50 %). With increasing CO_2 contents, there is an increase in free oxygens FO: While there is almost no FO in *sSA00*, there are ~ 4 % FO in *sSA03* and up to ~ 25 % FO in *sNC10* composition. The FOs are established on cost of BOs (which only reach ~ 30 % in *sNC10*). $BO_{Si\text{-}Si}$ is still dominant configuration. Minor amounts (≤ 1 %) of oxygen tri-clusters (TO) are detected across different compositions.

Figure 20 presents average coordination numbers as well as mean and most probable bond lengths of all cation types present in the simulations (cf. numeric values in Appendix 8, specific coordination number distributions in Appendix 9). In each simulation run, Si is basically tetrahedrally coordinated: in glasses with coordination numbers of 4.00 to 4.01 and in melts of 3.96 to 4.06. Al is mainly found in four-fold coordination as $^{[4]}$Al. Still, a considerable share of five-fold coordinated $^{[5]}$Al is present. Especially in melts, $^{[5]}$Al can make up as much as ~ 30 % of all Al (cf. Appendix 9). This results in average Al coordination numbers of 4.15 to 4.21 in glasses and of 4.28 to 4.46 in melts. CO_2-bearing compositions are dominated by carbonate, i.e. three-fold coordinated C. From *sSA03* to *CAR40*, $N_{C\text{-}O}$ increases from 2.82 to 2.98 in Y-bearing and from 2.86 to 3.00 in Sr-bearing melt composition. This corresponds to decreasing proportions of molecular CO_2 from ~ 10 % in *sSA03* to 0 % in *CAR40* (cf. Appendix 9). In contrast to these relatively stable patterns is the structural evolution of the remaining cations Y, Sr, Ca and Na along the join *sSA00* – *CAR40*. Conspicuous is the sudden drop in their coordination numbers in *sNC10* composition, which is potentially non-equilibrated (cf. Figure 18). Ignoring these irregularities, $N_{Y\text{-}O}$ is constant for *sSA00* and *sSA03* at ~ 6.6, with an increase to ~ 7.0 for *CAR40*. Opposing, $N_{Sr\text{-}O}$ increases already with initial CO_2-addition from ~ 7.5 in *sSA00* to ~ 7.9 in *sSA03* and *CAR40*.

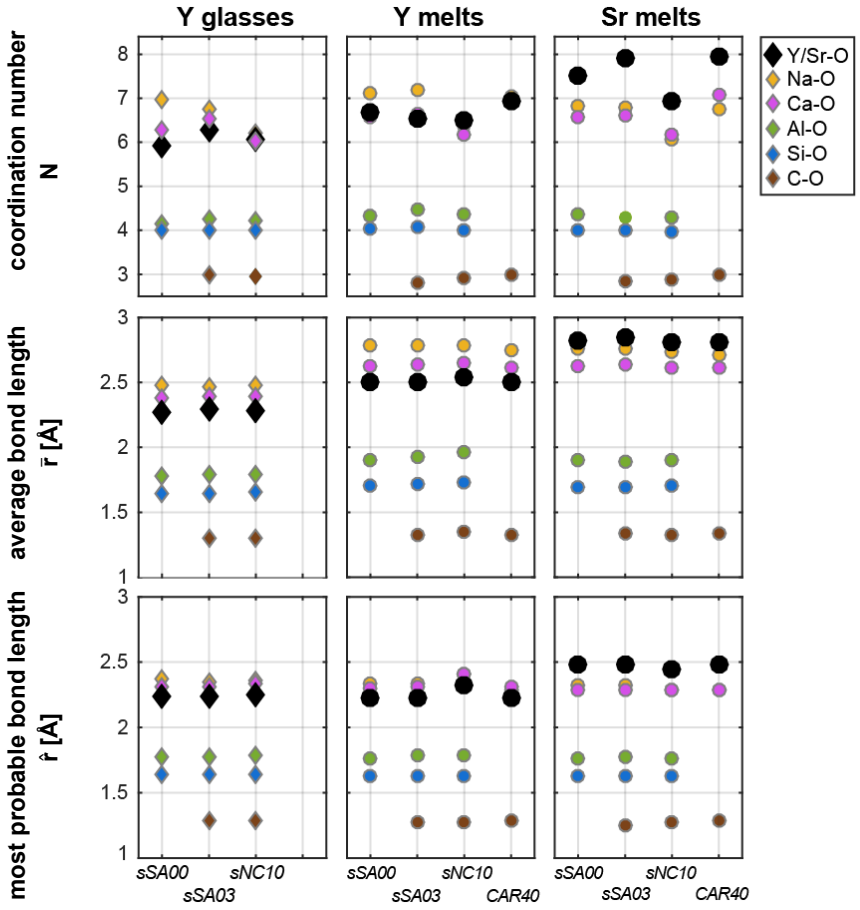

Figure 20: Coordination numbers and bond length in simulated glasses and melts. The CO_2 dependent evolution of coordination numbers and bond lengths along the compositional join sSA00 - sSA03 - sNC10 - CAR40 for all involved cations (Y or Sr, Na, Ca, Al, Si and C). Diamonds indicate the glasses, circles indicate melts.

In general, the MD derived bond lengths (average bond length $\bar{r}$ and most probable bond length $\hat{r}$) for each cation type are basically constant over the compositional join *sSA00 – CAR40* (cf. numeric values in Appendix 8). Here, the focus lies on $\bar{r}$, as this corresponds to the mean bond lengths R derived in EXAFS analysis. As Si-O and Al-O bond lengths distribution are symmetric in glasses, $\bar{r}$ and $\hat{r}$ are both the same at ~ 1.64 Å for Si-O and ~ 1.78 Å for Al-O. In the melts, $\bar{r}_{Si-O}$ and $\bar{r}_{Al-O}$ are slightly higher at 1.71 Å and ~ 1.90 Å, respectively. In Y-bearing composition, $\bar{r}_{Al-O}$ increases from 1.90 to 1.96 Å along the composition of *sSA00* to *sNC10*. All other cations have an $\bar{r}$ of constantly higher values compared to $\hat{r}$ in melts and in glasses. $\bar{r}_{C-O}$ is of ~ 1.30 Å in glasses and ~ 1.33 Å in melts. $\bar{r}_{Y-O}$ is ~ 2.28 Å in glasses and 2.50 Å in melts. Sr-O has a $\bar{r}_{Sr-O}$ of

~ 2.83 Å in melts. Values of $\bar{r}$ are up to 2.79 Å for Na and 2.65 Å for Ca in melts. Further details of the coordination environment of all involved cations, especially regarding their second shell cation neighbors are presented in Appendix 6.

3.4.3 Local structure of Y and Sr in simulated glasses and melts

Enhanced insights into the structural incorporation of Y and Sr are obtained by evaluating the structural role of coordinating oxygens, i.e. the proportions of BO, NBO and FO around a selected central cation. Figure 21 presents the distribution of coordination number of Y and Sr in all glasses and melts and respective average proportions of oxygen species in their first shell (cf. numeric values in Appendix 10 till 12). The following descriptions refer to averaged values over all coordination numbers. Y is mostly 6- or 7-fold and Sr 6- to 9-fold coordinated. Most Y or Sr coordinating oxygens are NBO_{Si} (~ 80 % in Y *sSA*, dropping down to ~ 60 % in Y *sNC* in glasses and melts; 55 - 60 % in Sr *sSA* and *sNC* melts, blue dotted bars in Figure 21). While Sr is not associated with any NBO_{Al}, minor amounts are found around Y (~ 10 % in glasses and up to 7 % in silicate melts, green dotted bars in Figure 21). Second most abundant oxygen species around Y and Sr are bridging oxygens, especially pronounced in *sSA03*: Sr is coordinated by BO with up to 44 %, Y with up to 22 % in the melt and with up to 18 % in the glass (solid dark and light blue bars in Figure 21). In *sSA00* and *sNC10*, Y and Sr are less likely coordinated with BO. In all cases, the most abundant BO is $BO_{Si\text{-}Si}$. Still 7 to 12 % of $BO_{Si\text{-}Al}$ is found in melts of Sr *sSA*, Y *sSA03* and Y *sNC10* (light blue bars in Figure 21). In general, higher fractions of BO are found for higher coordinated Y and Sr cations. FO are only of minor importance in the coordination around Y in *sSA* composition (up to 2 %), however are frequently found around Y and Sr in *sNC10* composition (16 – 28 %, orange bars in Figure 21). Exotic oxygen species are only found in very minor proportions with up to 0.2 % of $BO_{Al\text{-}Al}$ in Sr *sSA03* melt and of up to 0.3 % TO in silicate Y melts.

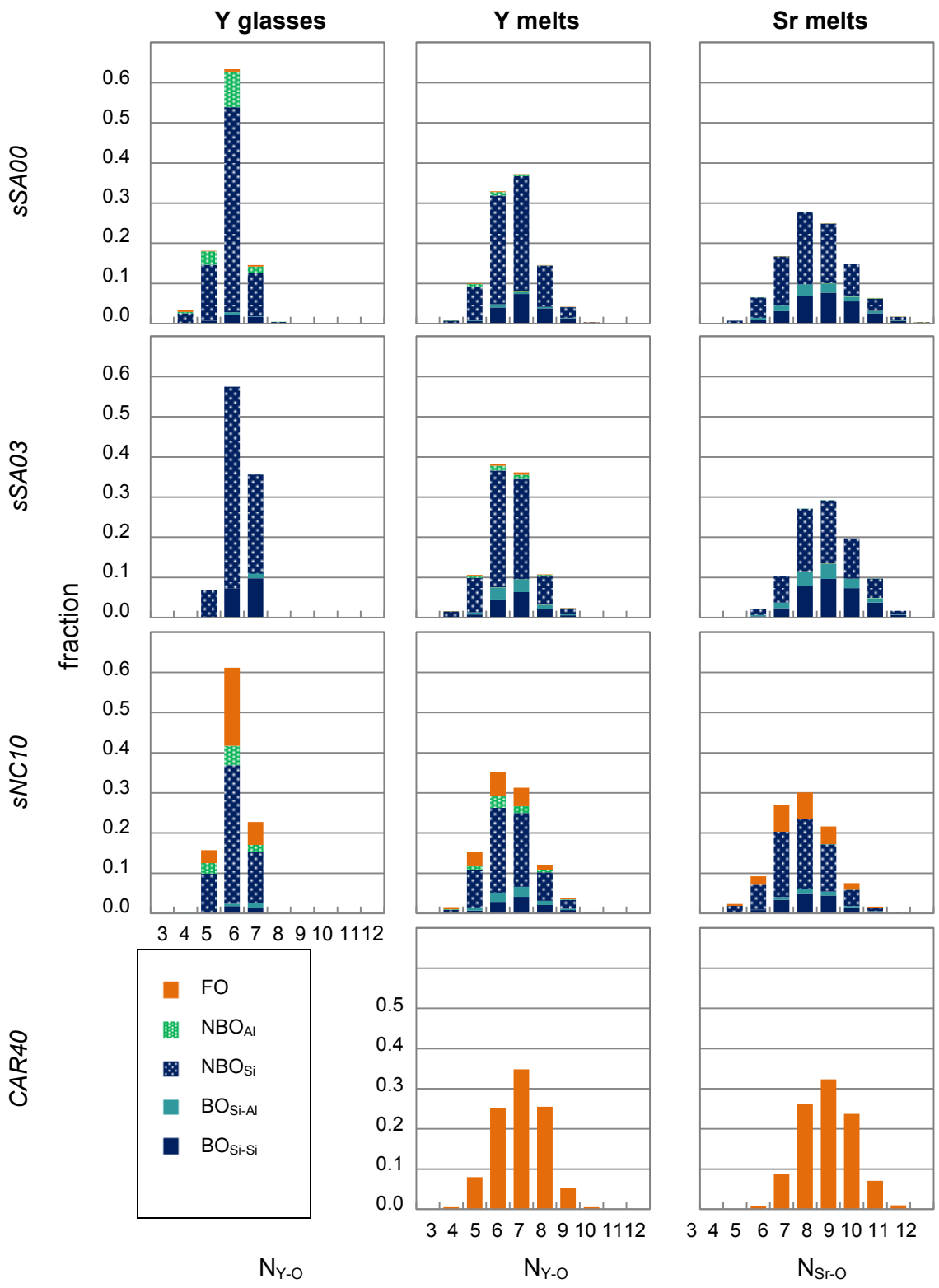

Figure 21: Proportions of oxygen species associated with Y and Sr in simulated glasses and melts. Fractions of free oxygen (FO), non-bridging oxygen (NBO), bridging oxygen (BO) and tri-cluster oxygen (TO) in the coordination environment of Y and Sr: differentiated by Y and Sr coordination number N (horizontal axis) and by involved network formers of [4]Al and Si.

3.4.4 Local structure of C in simulated glasses and melts

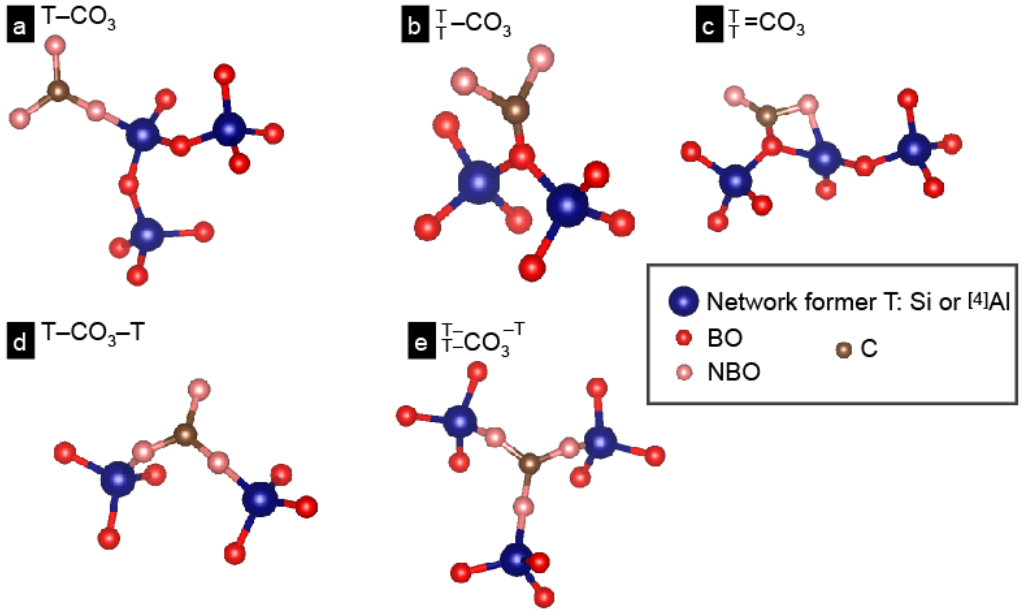

Figure 22: Potential carbonate – network interactions as found in MD simulations. Carbonate groups were found to interact with the network formers Si or $^{[4]}$Al either via a bridging oxygen (BO) or a non-bridging oxygen (NBO). It may be in a non-bridging position associated to one NBO (a), to a BO (b) or to a BO and a NBO to form the complex depicted in (c). It also may be in a bridging position between two network formers (T–CO_3–T) as in (d) or even between three network formers ($\frac{T}{T}{-}CO_3^{-T}$) as in (e). Created with the software AVOGADRO (Hanwell et al., 2012) and VESTA (Momma and Izumi, 2008).

C in glasses and melts can be present as two-fold coordinated molecular CO_2, as three-fold coordinated carbonate group (CO_3) or in very rare cases even as CO- or CO_4-groups. The following list presents all carbonate groups found in the present MD study and their network interactions are illustrated in Figure 22:

- FC is a free carbonate group, which has no connection to a network forming Si or $^{[4]}$Al.
- T–CO_3 is a carbonate group, where one oxygen is shared with a network former. Accordingly, there are Si–CO_3 formed via an NBO_{Si}, $^{[4]}$Al–CO_3 formed via an NBO_{Al} (Figure 22 a) or $\frac{T}{T}{-}CO_3$ formed via a BO (not further specified whether with Si or $^{[4]}$Al, Figure 22 b). A special case is given by the complex $\frac{T}{T}{=}CO_3$ (Figure 22 c), where two of the carbonates' oxygens are connected

to the same network former. At least one of the involved oxygens is an NBO and the associated network formers may be $^{[4]}$Si, $^{[5]}$Si or $^{[4]}$Al.

- T–CO_3–T is a carbonate group, which has a bridging role between two network formers. Depending on the network former species, it can be specified as Si–CO_3–Si, Si–CO_3–$^{[4]}$Al or $^{[4]}$Al–CO_3–$^{[4]}$Al (Figure 22 d). In rare cases, all three oxygens are shared with different network formers, referred to as tri-cluster carbonate $\overset{\mathrm{T}-}{\mathrm{T}-}\mathrm{CO}_3^{-\mathrm{T}}$ (Figure 22 e).

The proportions of C species shown Figure 23 (cf. numeric values in Appendix 13) can be summarized as follows:

(I) The simulated glasses almost only contain carbonate, while the corresponding melts show significant amounts of molecular CO_2 (up to 18 % in *sSA03*). Only minor amount of molecular CO_2 are found in quenched Y *sNC10* glass and in *CAR40* melts (≤ 2 %). Another rare species are CO_4-groups, making up at the maximum 1.4 % (in Sr *sSA03* melt).

(II) CO_2 mainly occurs as an isolated group. In rare cases it shares one oxygen atom with a network former (cf. Appendix 13).

(III) While the Y *sSA03* melt mainly contains FC (38 %), the chemically corresponding Sr *sSA03* melt mainly contains T–CO_3 (59 %).

(IV) In *sNC10* compositions the main species is generally FC with up to 60 % in Sr melt. The 2nd most abundant species is Si–CO_3 with up to 30 %.

(V) All silicate compositions contain minor proportions of T–CO_3–T (≤ 9 %), with relative equal proportions of Si–CO_3–Si and Si–CO_3–$^{[4]}$Al and smaller amounts of $^{[4]}$Al–CO_3–$^{[4]}$Al.

(VI) All silicate melts apart from Sr *sNC10* show minor proportions of $\overset{\mathrm{T}}{\mathrm{T}}\!=\mathrm{CO}_3$ (≤ 2 %).

(VII) The quenched glasses have an increased share of $^{[4]}$Al–CO_3 in comparison to the melts. This is especially pronounced for the Y *sSA03* glass with 38 % $^{[4]}$Al–CO_3 vs. 3 or 11 % in Y or Sr *sSA03* melt.

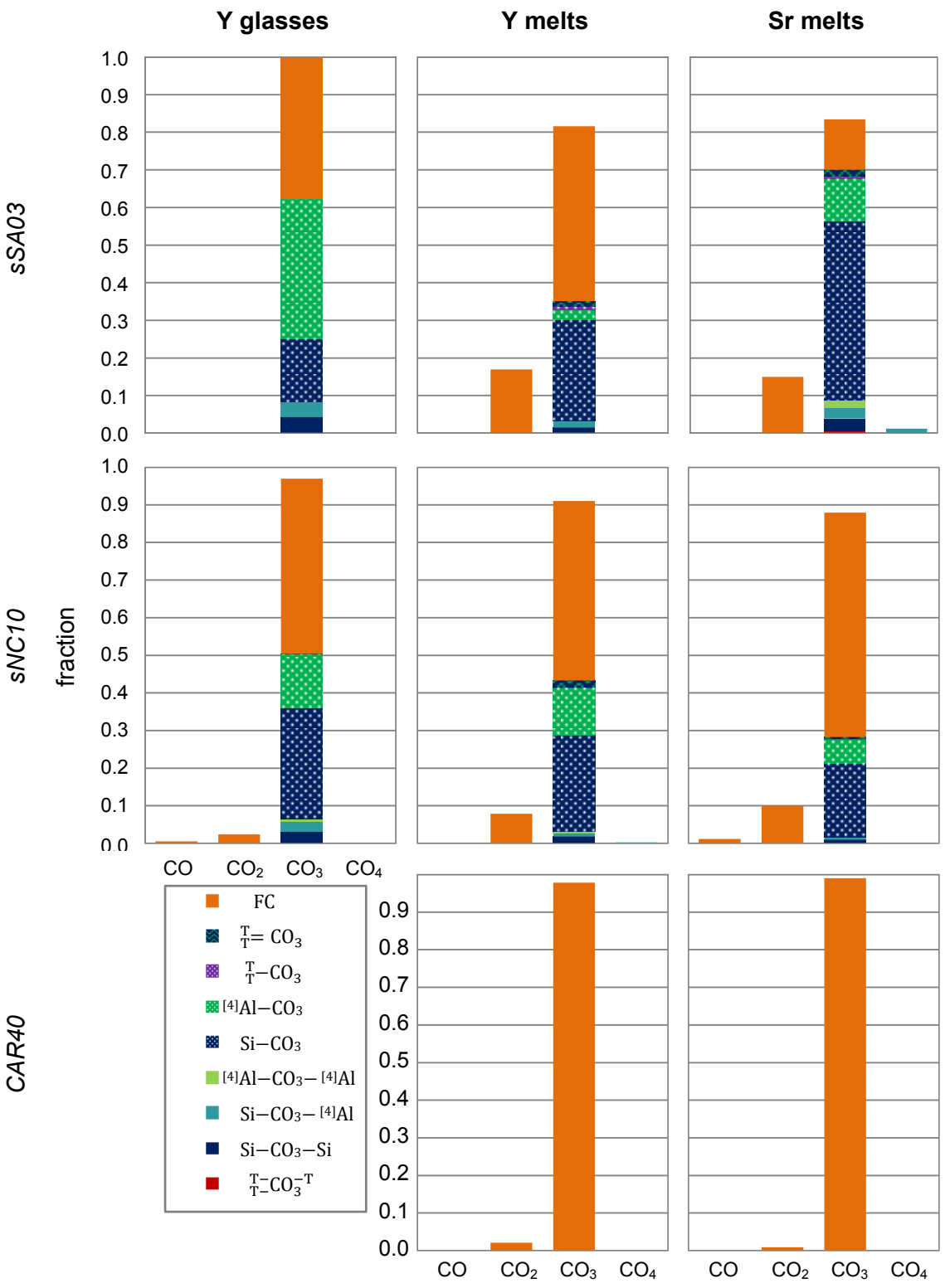

Figure 23: Proportions of C species in simulated glasses and melts.
Fractions of free C (FC), non-bridging C (T–CO_3), bridging C (T–CO_3–T) and tri-cluster C ($^{T}_{T}{-}CO_3{-}^{T}$) in glasses and melts: differentiated by C coordination numbers (horizontal axis) and by involved network formers and by structural units.

3.4.5 Summary of molecular dynamics simulations

Several snapshots of the simulated trajectories are given in Figure 24. Although they cannot represent the average melt structures completely, they contain a selection of possible configurations and give a general impression of the prevalent interactions. Snapshots of the Y *sSA00* (Figure 24 a) and Y *sSA03* (Figure 24 b) melts clearly show the loosely connected network of Si and $^{[4]}$Al. The network modifying Na and Ca cations are located in the cages and channels constructed by the network. Y is also located in such a cage with 6 to 7 coordinating oxygens in average, mostly as NBO_{Si}. Y *sSA03* melt contains carbonate groups, mainly surrounded by Na. Here, one planar carbonate is edge-sharing connected to a $^{[4]}$Al to form an $^{T}_{T}{=}\ CO_3$. The atoms of *sNC10* are not equally distributed but tend to separate into a C/Na/Ca-rich compartment (left hand side of Figure 24 c) and a Si/Al-rich compartment (right hand side of Figure 24 c). The creation of a carbonate dominated compartment correlates to the highly elevated fraction of FO found for *sNC10* composition (Figure 19). Over the simulation run, Y constantly tends to be located at the interface between silicate- and carbonate-rich compartments. Carbonate groups tend to avoid interactions with network formers; however one configuration of $^{T}_{T}{=}\ CO_3$ is shown in the selected snap shot. The degree of this separation is ever changing over the run time of the simulation, which indicates the absence of an equilibrium state (as already indicated by huge variations in the time dependence of the oxygen environment in Figure 18). Here, a snapshot was selected in which the separation is particularly pronounced. The heterogeneities exclude the *sNC10* sample as consistent member of the investigated silicate – carbonate join. This is already perceived in the distinct coordination number outliers presented in Figure 20, implying severe structural differences of *sNC10* compared to the other compositions.

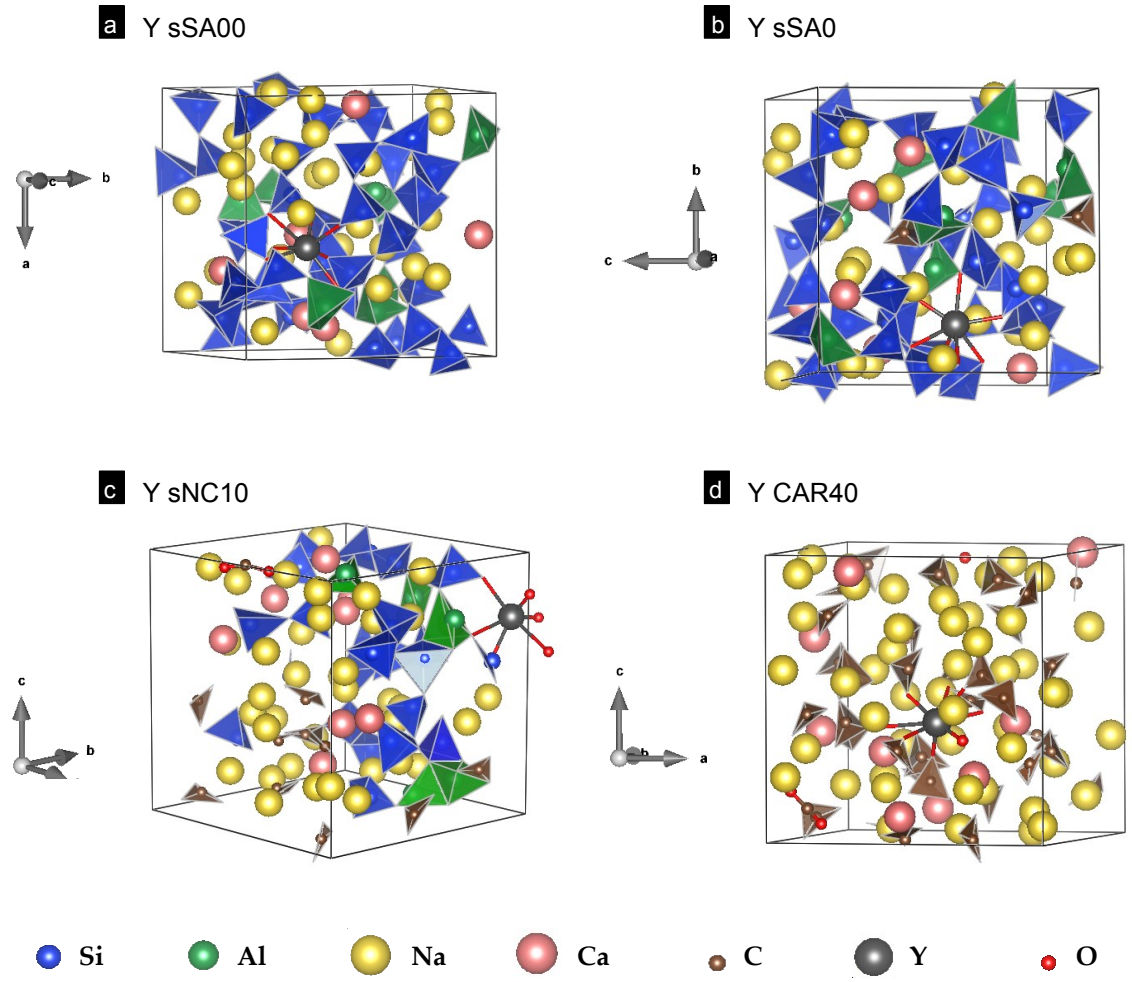

Figure 24: Selected snapshots of simulated Y melts.
Presented are the Y melts of *sSA00* (a), *sSA03* (b), *sNC10*(c) and *CAR40* (d). The coordination polyhedra of Si, Al and C are depicted in the same color as the respective atom and also represent the corresponding oxygens. Thus, only oxygens not coordinating Si, Al or C are shown in red. The coordination number of Y is indicated by its bonds to first shell oxygens.

The pure carbonate melt Y *CAR40* (Figure 24 d) contains planar carbonate groups which are either corner, edge or face sharing with adjacent Na and Ca cations in random distribution. Y is usually eight-fold coordinated within this structure. The snap shot presents the occurrence of molecular CO_2 as well as two oxygens, not associated to a carbonate group. A closer look into the carbonate melt reveals the formation of channels, stretching throughout the simulation cell as depicted in Figure 25.

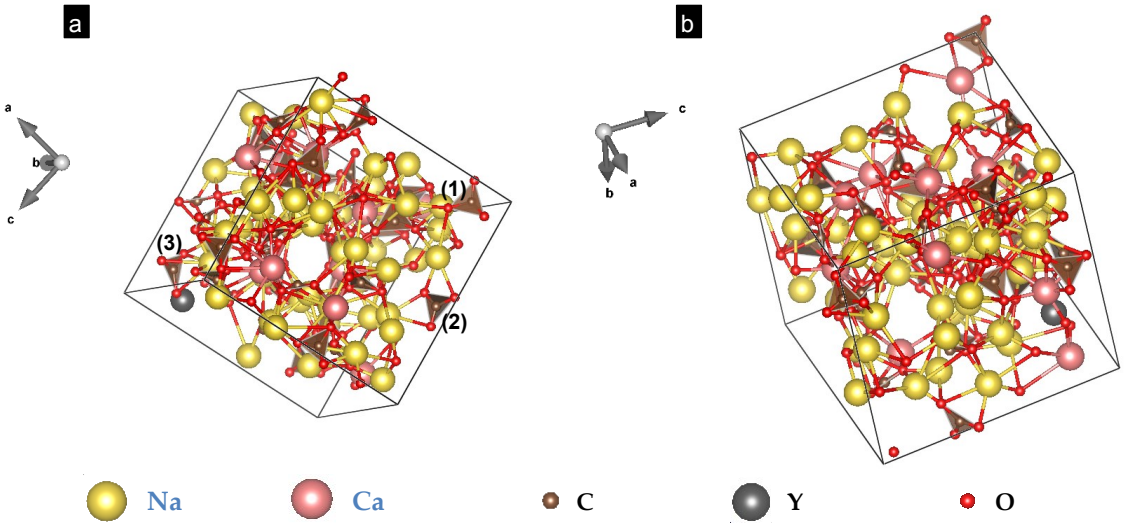

Figure 25: Selected snapshots of simulated Y carbonate melts indicative for channel formation.
Na/Ca-O bonds are included to emphasize the channel structures. The carbonate group interacts (1) corner, (2) edge or (3) face sharing with adjacent Na or Ca polyhedra (indicated in (a)).

4 Discussion

4.1 EXAFS and simulation experiments on silicate-carbonate glasses and melts

EXAFS was used to study the local structural environment of Y, La and Sr at low concentrations in synthetized glasses of various carbonate contents. *In-situ* EXAFS at high pressure and temperature made it possible to investigate melts ranging over the complete join from silicate via carbonate-bearing silicate to non-quenchable carbonate compositions. A novel design of the pressure assembly for the Paris-Edinburgh press was employed, which shows enhanced mechanical stability and transmittance properties. Thus, low element transmission EXAFS (down to ~ 2 wt % Y_2O_3 or SrO) at high pressure and temperature (up to 2.5 GPa at ~ 2000 K) was feasible at relevant X-ray energies (> 12500 eV). The structural changes of the local environments of Y, La and Sr observed along the silicate-carbonate join are rather small. In the investigated melts, the absolute variations in oxygen bond lengths of Y, La and Sr are below 0.04 Å. Nevertheless, such magnitudes are in good agreement with bond lengths variation between CO_2-free and CO_2-bearing rhyolitic, basaltic and kimberlitic melts (e.g. $\Delta R_{Ca\text{-}O} \leq 0.05$ Å) in MD studies of Guillot and Sator (2011, online version, Table C2). The significance of observed bond length variations is further supported by:

(I) Consistent element-specific bond lengths found in glass samples and quenched *in-situ* samples.

(II) Consistent general trends in bond lengths evolution along the studied joins for all elements in glass samples, in *in-situ* melt samples as well as in their quenched counterparts (cf. trends in Figure 14 b with Figure 14 c, in Figure 15 b with Figure 15 c and in Figure 16 b with Figure 16 c).

(III) Variations in Y and Sr K-edge XANES along the join silicate-carbonate melt indicate a continuous structural change of their coordination environment.

The first point implies that neither an effect of different elemental concentrations for Y, Sr and La (~ 0.5 wt % of Y_2O_3, SrO, La_2O_3 in glasses; 1.2 - 2 wt % Y_2O_3 or SrO, 3 or 6 wt % La_2O_3 in melts) nor a pressure induced effect is observable.

The second point implies, at least within the resolution of this experimental setting, a qualitative transferability of bond length characteristics from glass to melt structure. *In-situ* measurements at *HPHT* are of poorer quality (e.g. regarding EXAFS length, signal-to-background level) due to the enhanced thermal damping of the EXAFS signal. The increased absolute bond lengths of *in-situ* melt samples compared to glass and quenched *in-situ* samples are attributed to the thermal expansion (consistent with the linear thermal expansion expected by Hazen et al. (2000), cf. eq. 6). The wider maxima in the pair distributions and their enhanced asymmetries (cf. Figure 17) are due to increased thermal and configurational disorder in the melts.

Explorative MD studies were concomitantly conducted to (1) find support for EXAFS derived structural properties of Y and Sr, (2) elucidate the local environment of the remaining atoms in the composition and (3) provide general structural information on the silicate to carbonate glasses and melts investigated. It has to be stressed, that the presented MD studies are highly sensitive towards sampling effects due to relatively short run times and the small number of simulated atoms (~ 200). This is especially evident for low-content elements (Y and Sr in all compositions, C in *sSA03*) as an accidently captured meta-stable motif may severely bias the statistics of the configurational analysis. For these elements, derived average values are only of indicative character. This is for example manifested by comparing the low C-bearing Y and Sr *sSA03* melts. Although both melts essentially have the same chemical composition, the observed average local structure of C differs dramatically (Figure 23). However, it is reasonable to assume that major element data are valid, as they show consistent structural trends along the investigated joins as well as between chemically corresponding Y and Sr compositions (cf. oxygen species in Figure 19, R and N in Figure 20, carbon species in high-carbon melts of *sNC10* and *CAR40* in Figure 23, major element PDFs in Appendix 2 till 4).

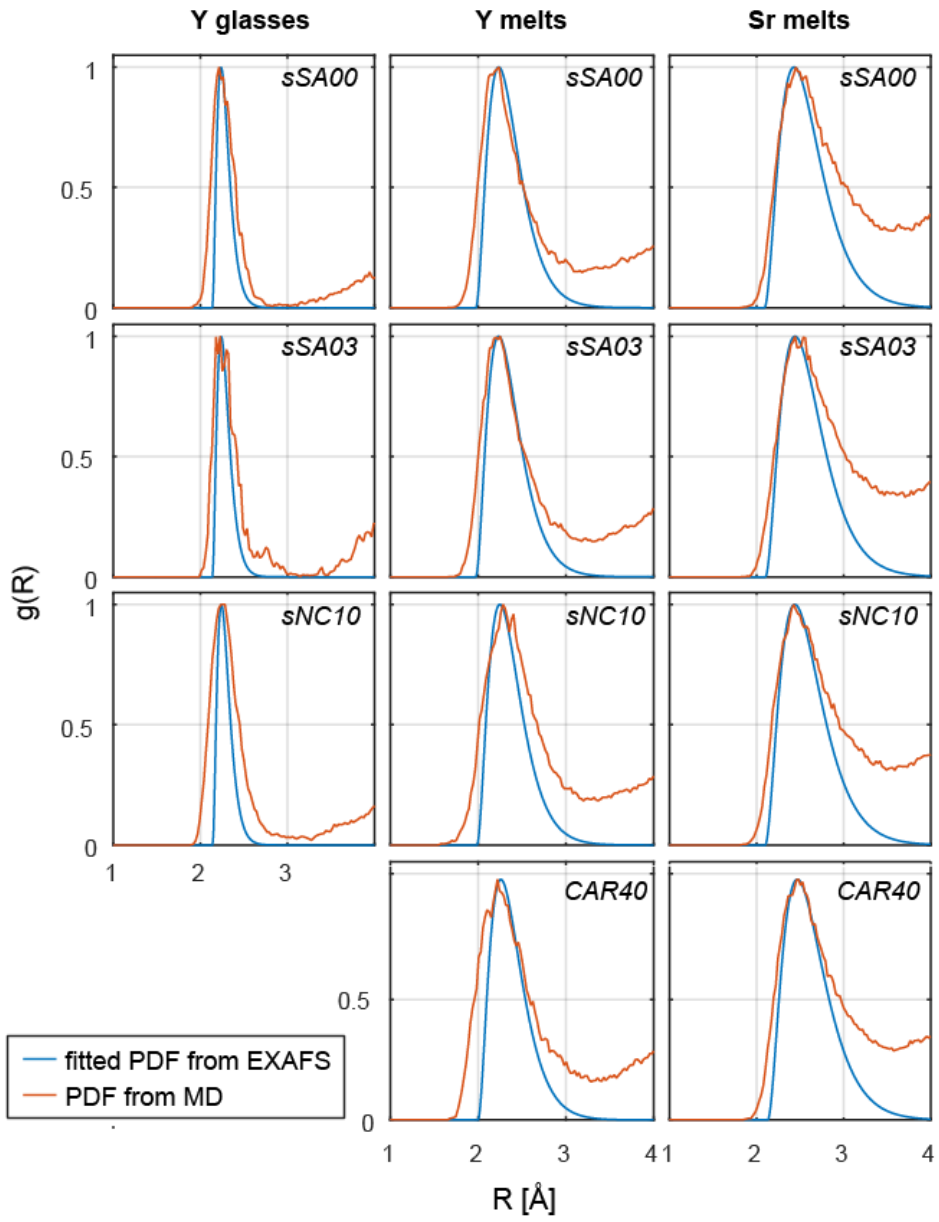

Figure 26: Comparison of MD simulated and EXAFS PDFs of glasses and melts.
PDFs derived from simulations as g(R) and EXAFS PDFs as p(R) = g(R)*N were normalized to their maximum for comparison and to cancel out amplitude effects of different concentrations (eq. 16).

Trace element data of simulations and EXAFS can be checked for consistency by comparing MD-derived PDFs with the fitted PDFs (cf. eq. 12) from EXAFS analysis (Figure 26). PDFs derived from EXAFS are subjects to following restrictions:

(I) In addition to single scattering effects between the respective atom pair, the EXAFS signal may show contributions of multiple scattering events of different atomic backscatterers (Stern et al., 1992). This effect does not interfere with PDFs presented here, as the EXAFS of disordered glasses and melts essentially contain first shell contributions only.

(II) As EXAFS generally lacks low-k information, the derived PDFs have a lack of information towards higher distances, expressed in an underestimation of the tail (Crozier, 1997; Eisenberger and Brown, 1979; Filipponi, 1994; Stern et al., 1992). A method to overcome this is presented by Stern et al. (1992), however is not applicable for highly disordered systems.

(III) A common assumption in EXAFS fitting is an underlying baseline of $g_{base}(R) = 0$ (Filipponi, 1994). This results in the PDFs descending down to 0 after the first shell maximum. While this assumption holds true in crystalline materials, it is not valid for highly disordered materials such as melts. Filipponi (1994) developed a method to account for this effect by including an additional background function into the fit procedure. This function relies on supplementary structural information, e.g. derived from additional diffraction or MD studies. As this function is highly temperature-sensitive, it should only be used for experiments conducted at the same temperature conditions. This is not the case in this study.

Point (II) and (III) provide the reasons for the fact that the EXAFS PDFs are significantly lower towards larger distances. The simulated PDFs are slightly noisy since they are retrieved from only one atom of Y or Sr over the sampling time. In contrast, the EXAFS PDFs are smooth since they represent a fitted distribution function. For Y glasses, simulated and EXAFS PDFs agree very well regarding their most probable bond length, i.e. the position of the maximum of the distribution. For Y melts, simulated and EXAFS PDFs show slight but unsystematic differences in maxima positions. For Sr melts, EXAFS PDFs maxima tend to be at slightly lower positions compared to simulated PDFs maxima for

CO_2-free compositions. This is balanced out with increasing CO_2 content until both maxima are coinciding for the pure Sr carbonate melt. simulated PDFs generally show a wider distribution. This might be largely attributed to the elevated temperatures of 3000 K prevalent in MD runs, which trigger an increased thermal disorder.

For the first time, the presented EXAFS dataset allows us to track local structural changes of minor and trace elements along the silicate-carbonate join, as relative differences within one experimental series can be interpreted. It should be noted though, that comparison to results of other studies may show systematic deviations due to differences in the fit models. In order to constrain the structural control on chemical partitioning in these systems, and to provide prime insights into the incorporation mechanisms, the observations were interpreted using established concepts of metal incorporation in silicate glasses and melts and compared to results drawn from concomitant MD simulations.

4.2 Structural properties of sodium-rich silicate glasses and melts

4.2.1 General structural characteristics

The low ASI values of the sodium-rich compositions studied (cf. Table 4) reflect the excess of Ca and Na compared to Al. Consequently, Al is assumed to be predominantly in tetrahedral coordination and to act as network former. This is confirmed by MD simulations, in which Al is in a mainly four-fold coordination (cf. $N_{Al\text{-}O}$ of between 4.15 and 4.46 in Figure 20 and Al coordination number distribution in Appendix 9). Still, *sSA* and *sNC,* have overall low concentrations of network forming cations and consequently low degrees of polymerization as is clearly illustrated in the corresponding simulated melt snapshots in Figure 23. The simulations further show that with decreasing ASI along *sSA00* – *sSA03* – *sNC10*, the fraction of BO also decreases. This is mainly due to a distinct increase in the fraction of FO and a minor increase in the fraction of NBO in *sNC10* composition only (Figure 19). This correlation demonstrates the fragility of the NBO/T parameter as an indicator for a melt structure. It only considers NBO as driving parameter and totally neglects BO and FO variations, which

highly influence polymerization characteristics. Additionally, it does not take into account the effect of variable field strength of cations.

BOs in the simulated samples are mainly formed in between Si-Si or $^{[4]}$Al-Si, with oxygen in between $^{[4]}$Al-$^{[4]}$Al appearing only in minor proportions. In glasses, the ratio $BO_{Al\text{-}Al}/BO$ is between 0.2 and 0.6 % and in melts between 0.6 and 1.0 % (recalculated from the basis O to the basis BO according to Appendix 7, cf. Figure 19). Especially the latter ratio rather corresponds to a random distribution of $^{[4]}$Al and Si to form BOs, where $BO_{Al\text{-}Al}/BO$ would be ~ 1 % (cf. Table 7). This is contradictory to the commonly assumed Al-Al avoidance rule, as known from crystalline minerals (Loewenstein, 1954). The Al-Al avoidance rule was found to be violated in aluminosilicate glasses for increasing cation field strengths of involved network modifiers (e.g. ^{17}O and ^{29}Si NMR studies of Lee and Stebbins, 1999, 2000; Stebbins et al., 1999) or at elevated temperatures (^{17}O NMR studies of Dubinsky and Stebbins, 2015). Despite the fact, that strict Al-Al-avoidance would be formally achievable, MD studies on Y and La doped aluminosilicate melts (Haigis, 2013) and ^{27}Al NMR studies of lanthanum aluminosilicate glasses (Jaworski et al., 2012) report a random distribution of $^{[4]}$Al and Si.

Table 7: Calculated random proportions of BO species.
The probabilities[4] are derived under the assumption that $^{[4]}$Al and Si are randomly associated with NBO and BO.

	sSA00	*sSA03*	*sNC10*
$BO_{Si\text{-}Si}$	78.1%	78.1%	77.2%
$BO_{Si\text{-}Al}$	20.8%	20.8%	21.8%
$BO_{Al\text{-}Al}$	1.1%	1.1%	1.0%

[4] As simplified calculated probability p on the basis of atom numbers given in Table 3 and averagely assuming 65 % of Al in tetrahedral coordination (cf. Appendix 9):
$p_{BO\text{-}Si\text{-}Si}=[n_{Si}/(n_{Si}+n_{Al})]*[(n_{Si}-1)/(n_{Si}+n_{Al}-1)]$, $p_{BO\text{-}Al\text{-}Al}=[n_{Al}/(n_{Si}+n_{Al})]*[(n_{Al}-1)/(n_{Si}+n_{Al}-1)]$,
$p_{BO\text{-}Si\text{-}Al}=[n_{Si}/(n_{Si}+n_{Al})]*[n_{Al}/(n_{Si}+n_{Al}-1)]+[n_{Al}/(n_{Si}+n_{Al})]*[n_{Si}/(n_{Si}+n_{Al}-1)]$.

In *sSA* melts at least 1 % of the oxygens forms tri-clusters (TO), i.e. they have a bridging function between three network formers. The existence of TO was early proposed by Lacy (1963) and Toplis et al. (1997) and was ever since strongly debated (e.g. Henderson, 2005). Minor proportions of TO in aluminosilicate glasses and melts are commonly found in MD studies (Cormier et al., 2003; Du, 2009; Iftekhar et al., 2012; Jaworski et al., 2012; Okhotnikov et al., 2013; Vuilleumier et al., 2009; Wagner et al., 2017; however, normally not evaluated regarding its stability over time).

4.2.2 Y, La and Sr in sodium-rich silicate glasses and melts

Particularly the incorporation of the network modifiers Y, La or Sr as major components into silicate glasses has seen a number of studies, mainly due to their technical significance (such as in optical or medical applications or in the context of nuclear waste disposal, e.g. Du, 2009 references therein; Marchi et al., 2005; McKeown et al., 2003; Xiang and Du, 2011). Only a few studies concentrated on low elemental concentrations, typically relevant for geological systems (e.g. Haigis et al., 2013; Kohn et al., 1990; Ponader and Brown, 1989; Simon et al., 2013).

Table 8: Reported Y, La, Sr oxygen coordination and bond lengths in silicate glasses and melts.

	N	R [Å]	Method and Reference
Y			
glasses	6.2-7.0	2.24-2.34	EXAFS: Simon et al. (2013); neutron/X-ray scattering: Pozdnyakova et al. (2008); classical MD: Du (2009), Iftekhar et al. (2012), Okhotnikov et al. (2013)
melts	6.2-7.9	2.38-2.57	classical MD: Haigis et al. (2013), *ab initio* and classical MD: Wagner et al. (2017)
La			
glasses	6-9	2.35-2.59	EXAFS: Larson et al. (1991), Ponader and Brown (1989); X-ray/neutron scattering: Pozdnyakova et al. (2008), Wilding et al. (2007); classical MD: Jaworski et al. (2012), Okhotnikov et al. (2013), Park et al. (2002)
melts	6.7-8.2	2.55-2.71	*ab initio* and classical MD: Wagner et al. (2017)
Sr			
glasses	5-8	2.5-2.73	EXAFS: Kohn et al. (1990), McKeown et al. (2003); X-ray/neutron scattering: Cormier et al. (1999), Creux et al. (1995), Johnson et al. (2007); classical MD: Xiang and Du (2011)

Y, La and Sr coordination numbers and distances derived by EXAFS (Table 6) and MD simulations (Figure 20 and Appendix 8) in CO_2-fee silicate glasses and melts are in good agreement with data of previous studies (Table 8, references therein). Figure 27 presents the range of bond distances and calculated bond strengths for Y-O, La-O and Sr-O. Concurrent MD studies confirm increased average bond lengths for all cations in melts compared to glasses. At the same time the most probable bond length basically remains constant. This implies a widening of the coordinating oxygen distribution as the prevalent expansion mechanism.

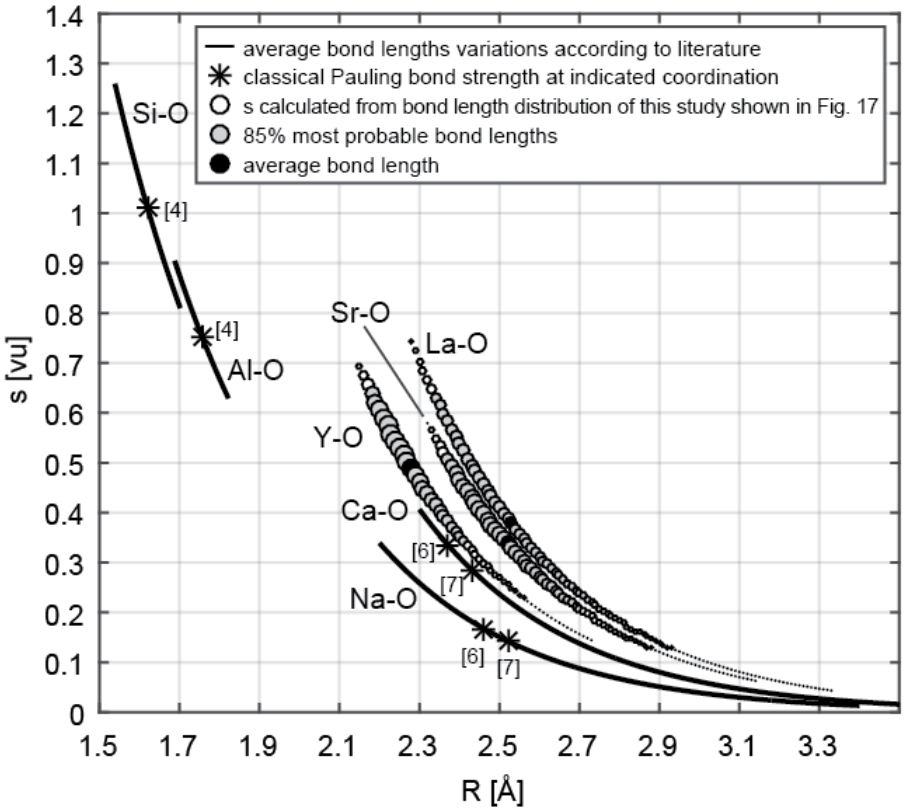

Figure 27: Correlation of bond length R and bond strength s for relevant cations.
Variation in average bond lengths of Si-O, Al-O, Ca-O and Na-O as observed in silicates were taken from literature (Brown and Gibbs, 1970; Brown et al., 1969; Gibbs et al., 1972). Y-O, La-O and Sr-O bond lengths distribution in CO_2 free *sSA* glasses as determined in this study. The size of the circular symbols corresponds to the probability of the respective bond length. Bond strengths were calculated according to eq. 5 and with data of Brese and O'Keeffe (1991).

A compelling model to describe the association between a cation and the network is given by the bond valence theory (Brown, 2009), which allows to rationalize the relation between the bond length R and the bond valence or bond strength s (in valence unites, vu) and eventually the coordination number N (cf. eq. 13 and 14). Additionally, stable structures require satisfied electrostatic valences as described by Pauling's 2nd rule: i.e. the sum of all bond valences of an ion needs to equal its formal charge within ± 0.1 vu. Figure 27 presents the classical Pauling bond strengths of Si-O and Al-O in tetrahedral coordination and Ca-O and Na-O in 6- and 7-fold coordination as calculated by eq. 13. In alkali silicate structures, individual bond lengths of Si-O, Al-O, Ca-O or Na-O may show huge variations; consequently, individual effective bond strengths cover large ranges (cf. Figure 27). These variations clearly depict the sensitivity

of structural arrangements towards the competition between different ions to reach their energetic most favorable configuration. The ability of a cation to promote its preferred local environment can be described by its field strength s_f:

$$s_f = z_c / R_i^2 \quad (20)$$

with z_c as the cation valence and R_i as the ionic radius (cf. Table 9). Bond valence theory proved as a useful approach to understand the local environment, of several metal cations in silicate melts. This was successfully employed in combination with data retrieved from X-ray absorption spectroscopy, in latter years also in corroboration with MD: e.g. Zr (Farges et al., 1991), Th (Farges, 1991), U (Farges et al., 1992), Ni (Galoisy and Calas, 1993), Ti (Farges et al., 1996), Fe (Rossano et al., 2000), and also Y (Haigis et al., 2013; Simon et al., 2013). Rossano et al. (2002) and Trcera et al. (2011) used the bond valence model to check the validity of the structural models derived by MD simulations using classical potentials. This provided a substantial improvement for employing the MD models for calculating XANES spectra of the Mg K-edge (Trcera et al. 2011).

Table 9: Cation field strength of compositional cations.
Calculated with ionic radii of Shannon (1976) and in decreasing order. In bold are the field strengths of cations investigated with EXAFS.

	Cation field strength s_f [vu/Å^2]							
Coordination	IV	V	VI	VII	VIII	IX	X	XII
Si^{4+}	59.17							
Al^{3+}	19.72							
Y^{3+}			**3.70**	**3.26**	**2.89**	**2.60**		
La^{3+}			**2.82**	**2.48**	**2.23**	**2.03**	**1.86**	**1.62**
Ca^{2+}			2.00	1.78	1.59	1.44	1.32	1.11
Sr^{2+}			**1.44**	**1.37**	**1.26**	**1.17**	**1.08**	**0.96**
Na^{+}	1.02	1.00	0.96	0.80	0.72	0.65		0.52

4.2.2.1 Bond valence theory applied on Y, La and Sr

Figure 28 shows potential network former – network modifier configurations. Oxygen valences are already, at least partly, compensated by Si or $^{[4]}$Al or by additional network modifiers (as given by s in Figure 27). The formation of a distinct structural unit strongly depends on the ability of a cation M to provide the respective bond valence to maintain electrostatic neutrality for the linking oxygen (as indicated next to the M-O bonds in Figure 28).

NBOs (Figure 28 a, b, c) have a much higher need for charge compensation than BOs (Figure 28 d, e, f). This leads to a strong competition for the modifying cations to bond to NBOs in the order of Y > La > Sr, according to their average ability to supply bond strength (Figure 27), which depends on their field strength (Y > La > Sr in 6- or 7-fold coordination, cf. Table 9). In Ca-bearing compositions, this effect is enhanced: Y shows the highest bond strength, whereas La and Sr additionally compete with Ca (cf. Table 9, Figure 27). Y's strength is also manifested in its lower local disorder, expressed in lower σ^2 and h, compared to Sr or La in the silicate and carbonate compositions investigated (Table 6).

Of the presented NBO-configurations, Al-NBO with an additional network modifier (Figure 28 b) and Si-NBO without additional network modifiers (Figure 28 c) require the highest charge compensations. Both, Y and La may show high bond strengths (≥ 0.65 vu) and could potentially charge balance the linking oxygen. However, this would require all involved bond lengths to be pushed to the limits usually observed in silicate structures and is thus unlikely. Instead, balancing out Si-NBO units with an additional network modifier (Figure 28 a) is easier to achieve by Y and La but also by Sr. Accordingly, further network modifying Na or Ca in vicinity would reduce the required charge balance drastically and thus, facilitate the structural linkage to cations with lower bond strength (e.g. La with an average s of 0.39, Sr with an average s of 0.33 vu). Bridging oxygens in Si-BO-Si (Figure 28 d) and Si-BO-Al (Figure 28 e) units may already be in electrostatic balance. However, a structural link to a cation with low bond strength such as La and Sr is still achievable. To summarize, Y strongly favors NBO-rich environments, whereas La and even more

pronounced Sr generally favor NBO environments in association with additional network modifiers and are better able to adapt to BO-rich environments.

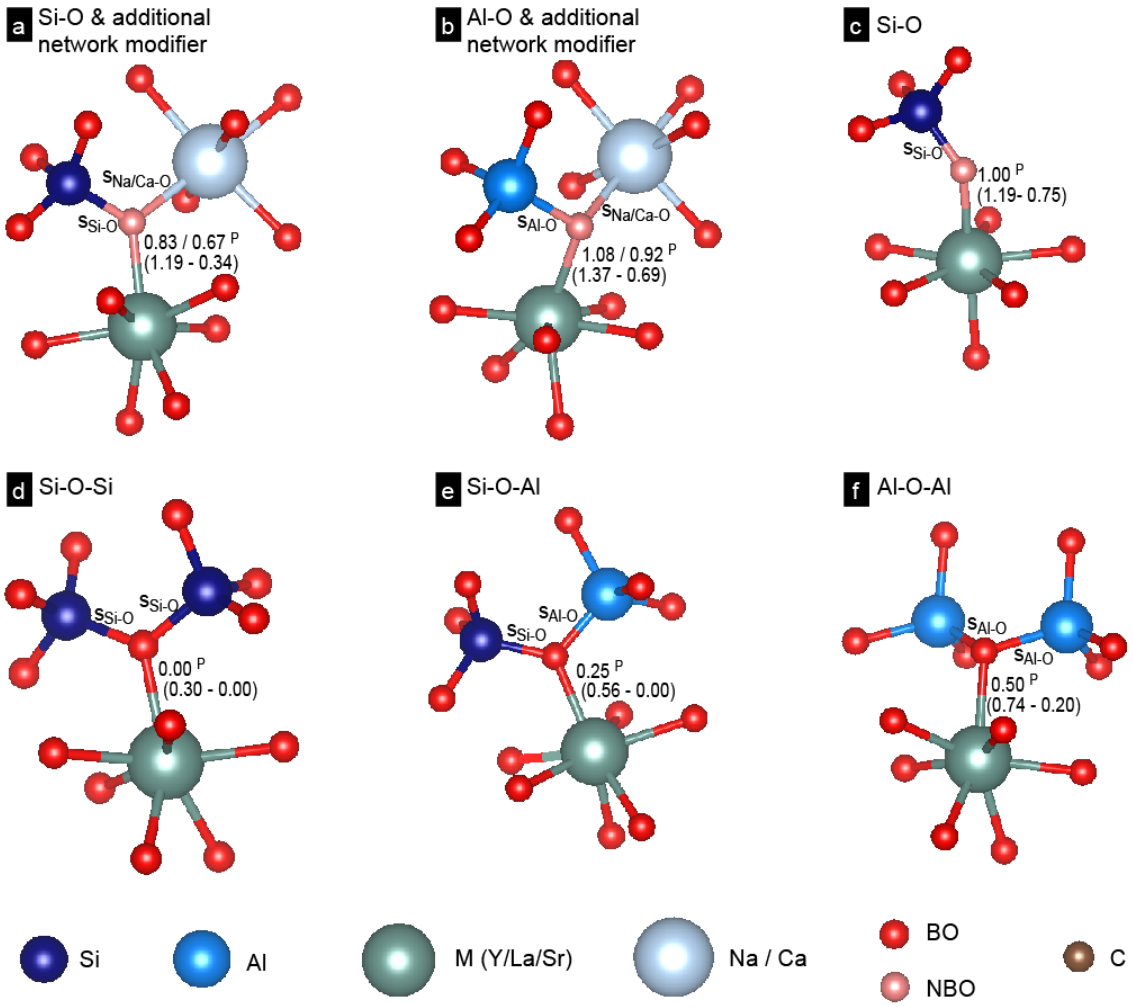

Figure 28: Potential structural units in silicate networks.
Potential structural units of modifying cations M interacting with the non-bridging oxygens of the silicate network (top) and with the bridging oxygens (bottom). Values next to M-O bonds indicate the proportion of $s_{M\text{-}O}$ supplied by the cation to ensure an electrostatic valence on O equal to 2 (^{P} as calculated from classical Pauling bond strengths, values in parentheses as calculated from maximum and minimum values of bond strength of involved atoms, cf. Figure 27). Created with the software AVOGADRO (Hanwell et al., 2012) and VESTA (Momma and Izumi, 2008).

The bond valence considerations are supported by the MD studies as they emphasize a strong preference of NBO and thus avoidance of BO in the coordination environment of Sr and even stronger of Y: In sSA00 melts, the fraction of

BOs adjacent to Y is only 1/3 of that in the bulk composition, for Sr it is only 2/3 (compare values of BO in the 1st shell of Y and Sr in Appendix 11 and 12 with values of BOs in bulk compositions from Appendix 7). At the same time, Sr is surrounded by twice as much BO than Y in all investigated melt compositions (compare values of BO in the 1st shell of Y and Sr in Appendix 11 and 12). Y also tends to interact with at least some NBO_{Al} (up to 6 % of all NBO), while Sr only interacts with NBO_{Si}. This clearly demonstrates Sr's ability to adapt to structural motifs with higher local electrostatic valences. In Y glasses with lower average Y coordination numbers, even less BO coordinates Y (down to 1/10 of bulk BO fraction) and even more adjacent NBOs are associated with an Al (up to 14 %).

The local environments of Y and Sr show a clear Al-Al-avoidance in glasses (total oxygen $BO_{Al\text{-}Al}$ fractions of 0.0 %) and a slight avoidance in melts (total oxygen $BO_{Al\text{-}Al}$ fractions of ≤ 0.1 %). This is in contrast to the rather random BO distribution between Si and Al as found in the overall melt compositions (cf. chapter 4.2.1). It indicates, that the increased $BO_{Al\text{-}Al}$ fractions found in melts are not triggered by Y as stabilizing factor, as was suggested for other rare earth elements (for La by Jaworski et al., 2012).

4.2.2.2 Local structure of Y, La, Sr in CO_2-free glasses and melts

In CO_2-free glass samples, bond lengths of Y-O are similar for *sSA* and *sNC* (ASI of 0.19 and 0.11, respectively) compositions. This is in agreement with a former EXAFS study by Simon et al. (2013), that only shows an increase of Y-O bond lengths in more polymerized compositions above an ASI of 0.64. This bond length increase is consequently accompanied by a bond strength decrease and thus prevents over-bonding of bridging oxygen (i.e. keep their bond-valence sum at approximately 2).

La-O and Sr-O seem to undergo a slight increase in bond length from *sSA* to *sNC* CO_2-free compositions. This effect may be triggered by the unique structural characteristics of the sodium-rich compositions (*sNC* with ~ 32 mol % Na_2O compared to *sSA* with ~ 23 mol % Na_2O, cf. Table 4, recalculated in mol %). Si K-edge XAFS on silicate glasses with more than ~ 30 mol % Na_2O show drastic adjustments in the network structure (Henderson, 1995). These are

interpreted in the context of a modified random network model (cf. chapter 1.2 and Figure 1 b), where alkali-rich channels separate the silicate network into many sub-networks of higher local polymerization (Greaves, 1985; Jabraoui et al., 2016). EXAFS derived bond length variations in this study imply: (1) Due to its high field strength, Y is able to establish its favored configuration in close association with NBOs in the extremely peralkaline compositions. (2) In comparison to Y, La is of larger size and Sr is of lower field-strength. In the extremely peralkaline composition, on the one hand, La and Sr could easily promote their favored configuration in the relatively dynamic (percolation) channels, outcompeting the other low field strength cation Na. On the other hand, larger sites are provided in the locally higher polymerized silicate subnetworks (cf. Simon et al., 2013, references therein).

In the MD simulation of the corresponding composition *sNC10*, the ongoing structural rearrangements and small systems size prevent statistically reliable conclusions. However, the indicated separation into a C/Na/Ca-rich and a Si/Al-rich compartment (cf. chapter 3.4.5) could be interpreted in two ways: (I) as an attempt to form a modified random network with the C/Na/Ca-rich compartment corresponding to the percolation channels separating the silicate network; (II) as an unmixing according to the phenomenon of liquid immiscibility between a silicate and a carbonate melt. Unfortunately, particularly the simulation cell size with only ~ 200 atoms is too small to allow for further conclusions.

4.2.2.3 Local structure of Y, La, Sr in CO_2-bearing glasses and melts

The EXAFS data suggest that introducing CO_2 into the *sSA* glasses gradually increases both the La-O and Sr-O bond length (Figure 15 b and Figure 16 b). This has two possible implications: (1) Y, with its higher field strength (cf. Table 9), successfully competes for its favored structural configuration, unaffected by introduced CO_2. (2) CO_2 preferentially assimilates in structural environments associated with La or Sr. Two potential environments for CO_2 dissolution based on bond valence considerations are suggested and summarized in Figure 29.

(I) CO_2 attachment to a non-bridging oxygen with one or two additional adjacent network modifiers (Figure 28 a, b) to form T–CO_3 with a non-

bridging oxygen (Figure 29 a). To avoid an over-bonding of the linking oxygen, the bond strength contribution of associated network modifiers needs to decline by increasing their distance. This mechanism would agree well with numerous observations of carbonate having a close association to network modifiers such as Ca (e.g. Brooker et al., 2001b; Haigis et al., 2013).

(II) CO_2 incorporation in regions with a locally high tetrahedron density (Figure 28 d, e, f), such as in between two tetrahedra to form T–CO_3–T (Figure 29 b). This locally introduces additional oxygens and also requires large shares of electrostatic valence provided by the two linking oxygens to charge balance C. For network modifiers in vicinity, this leads to an increase in coordination number and a decrease in bond strength.

Apart from different preferences of Y, La and Sr to associate with certain structural units, La and Sr are inferior in competing for a favorable environment due to their lower cation field strengths (cf. chapter 4.2.2.1). Consequently, Sr is most sensitive towards CO_2-induced structural changes followed by La. Additional dissolution mechanisms are possible, e.g. the formation of metal carbon complexes which are only loosely associated to the silicate network. However, they are not resolvable by investigating EXAFS bond length variations of the studied elements here.

In the extremely sodium-rich *sNC* glasses, CO_2 dissolution has no detectable impact on oxygen bond lengths of Y, La and Sr. In the light of the modified random network model, this implies that the strongly microsegregated silicate network (cf. chapter 1.2 and 4.2.2.2) is rather flexible in adjusting to the electrostatic needs of dissolved CO_2 and network modifiers, not forcing unfavorable configurations.

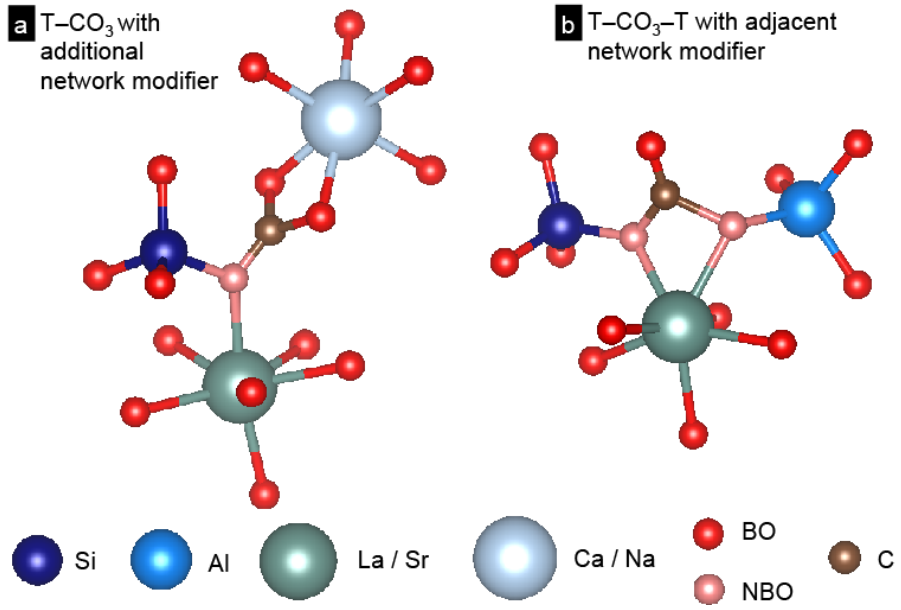

Figure 29: Two potential mechanisms of CO_2 dissolution in vicinity to La or Sr.
(a) The carbonate as T–CO_3 between a network former, La or Sr and an additional network modifier. (b) The carbonate as a T–CO_3–T between two network modifiers and adjacent to La or Sr. Created with the software AVOGADRO (Hanwell et al., 2012) and VESTA (Momma and Izumi, 2008).

The MD simulations suggest an increase in Y and Sr coordination number as a function of CO_2 along the join *sSA00* to *CAR40*, except *sNC10* which shows compartment separation (cf. Figure 20). These trends in coordination numbers correspond well to the EXAFS derived trends in coordination numbers, which can be directly concluded from the determined bond lengths, to which they are correlated (cf. Table 6, Figure 14 and Figure 16). Thus, both EXAFS and MD data show: (1) initially constant Y bond lengths / coordination numbers, which only increase in carbonate compositions and (2) immediately increasing Sr bond lengths / coordination numbers, starting with the first introduction of CO_2 into the system. On the one hand, PDFs obtained from the MD studies demonstrate that the change in Sr coordination number in melts can be mainly attributed to an increase in amplitude, e.g. a real increase in coordination number (Appendix 4). On the other hand, they show that the change in Y coordination number can be mainly attributed to a widening of the first coordination shell, i.e. an increase in disorder (Appendix 3). It is tedious to transfer detailed structural mechanisms derived from MD studies conducted at 3000 K to melts or even

glasses investigated with EXAFS at much lower temperatures. Nevertheless, an increase in local disorder around Y as a consequence of structural adaption of Y to changing environments is also documented by Simon et al. (2013) in EXAFS studies on silicate glasses and melts. There, the observed increases in Y bond length were attributed to an increase in local disorder rather than to a shift of the most probable bond length.

4.2.3 C in sodium-rich silicate glasses and melts

The CO_2 speciation in silicate melts is controlled by melt composition, pressure and temperature (Ni and Keppler, 2013b). At elevated temperatures, the equilibrium $CO_2 + O^{2-} \leftrightarrow CO_3^{2-}$ shifts towards molecular CO_2 (e.g. Morizet et al., 2001; Nowak et al., 2003), at elevated sodium contents it shifts towards carbonate (e.g. Brooker et al., 2001b; Kohn et al., 1991). In chemical analogy to alkali silicate melts investigated with infrared spectroscopy (Konschak and Keppler, 2014), carbonate is assumed to be the predominant species in compositions synthesized in this study. This assumption is supported by the presented MD simulations (cf. chapter 4.2.3). Several other recent MD studies in silicate melts observed carbonate either as free carbonate (FC), as associated with one network tetrahedron (T–CO_3) or as bridging between two network tetrahedra (T–CO_3–T). Classical MD studies of Guillot and Sator (2011) concentrated on CO_2 solubility in rhyolitic, basaltic and kimberlitic melt. In experiments containing 2 wt % CO_2, these authors identified typical structural units of T–CO_3–T and T–CO_3 with a distinct preference to associate with NBO over BO. Vuilleumier et al. (2015) compared results of classical MD and *ab initio* MD on basaltic and kimberlitic melts (each with ~ 20 wt % CO_2). The authors showed that *ab initio* MD yields very different proportions of carbonate complexes, calculating 48 % as T–CO_3, 31 % as T–CO_3–T and 21 % as free carbonate in basaltic melts and 75 % as free carbonate, 22 % as T–CO_3 and 3 % as T–CO_3–T in kimberlitic melts. The free carbonate was always in close association with an alkali earth cation.

In this study, MD confirms carbonate as the dominant species (cf. Figure 23, > 80 %). As already proposed on the basis of EXAFS data (cf. mechanisms (I) discussed above), the formation of T–CO_3 is one major carbonate incorporation

mechanisms in silicate networks. 30 to 60 % of all C form such configurations, with a strong preference for NBO_{5i} in melts (Figure 23 and Appendix 13). The proportion of T–CO_3 declines from *sSA03* to *sNC10* composition on the account of creating more FC (up to 60 %). In *sNC10* composition, this is attributed to the creation of a carbonate-rich compartment, characterized by loosely interacting free carbonate groups and network modifiers. The formation of T–CO_3–T structural units (cf. mechanism II) is rather insignificant, with occurrences of below 2 % (Figure 23 and Appendix 13). It is noteworthy that of all T–CO_3-T units, 12 to 25 % are $^{[4]}$Al–CO_3–$^{[4]}$Al, which is significantly more than a random Al-Si distribution would suggest (~ 1 %, in analogy to calculations presented in Table 7). Furthermore, MD suggests FC as most dominant carbonate configuration: up to 100 % in carbonate melts, up to 46 % in the silicate composition of *sSA03* and up to 60 % in the separated liquid of *sNC10*.

MD studies suggested that next to carbonate, at least 8 mol % of the carbon is found in the form of moleculare CO_2 in sodium-rich silicate melts. Otherwise, their quenched counterparts contain either no or insignificant amounts of molecular CO_2. A lack of molecular CO_2 in depolymerized glasses is well documented in experiments (e.g. Blank and Brooker, 1994; Fine and Stolper, 1985). Classical MD studies of Guillot and Sator (2011) on kimberlitic, rhyolitic and basaltic melts also found significant proportions of molecular CO_2 at high temperature (> 1700 K). Furthermore, they observed a temperature dependence of the CO_2:CO_3 ratio, which would suggest no molecular CO_2 in the depolymerized basaltic composition at lower temperatures, which are representative for glasses. There is additional experimental evidence that CO_2 formation is strongly triggered by increasing temperatures from annealing experiments in albitic, dacitic and jadeitic glasses (Morizet et al., 2001; Nowak et al., 2003) and from diffusion experiments in albitic and jadeitic melts (Spickenbom et al., 2010).

4.3 Structural properties of carbonate melts

In the carbonate-dominated melts (*CAR*), an increase in bond length compared to the CO_2-free or low-CO_2 content melts can be inferred for all studied elements (Figure 14 c, Figure 15 c, Figure 16 c). In the case of Y, this is the first ob-

served change in bond lengths along the complete join between silicate and carbonate melt: Only at exceedingly high CO_2 contents between the silicate-poor carbonate (*CAR35* and *CAR39*) and silicate-free carbonate (*CAR41*) compositions, Y adapts to the carbonate-dominated environment. This confirms the mutual avoidance of Y and CO_3^{2-}, as already suggested by the insensitivity of Y towards moderate CO_2 increases in silicates (cf. chapter 4.2.2.3). La shows continuously increasing bond lengths with increasing CO_2 content up into the carbonate region (excluding the highly boron contaminated pure carbonate sample), continuing the trend already observed for moderate CO_2 contents. Sr on the other hand shows a different picture. Although the Sr-O bond length is generally increased compared to silicate composition, no change is detectable between the silicate-poor *CAR35* and the silicate-free *CAR41* composition. This implies that Sr is already located in an energetically stable carbonate environment and remains unaffected by further decrease in the amount of SiO_4-tetrahedra. This observation is consistent with a close association of Sr to CO_3^{2-} as already suggested by the sensitivity of the Sr environment to moderate changes in CO_2 content in silicate compositions.

A long-standing problem is the development of structural models of carbonate melts, which are of ionic character. Based on results of vibrational spectroscopy on carbonate compositions exceptionally quenchable to glasses, Genge et al. (1995) suggest that the carbonate melt structure is a loose framework formed by carbonate ions and alkali earths as bridging cations. This framework is supported by modifying cations or molecular groups (e.g. alkalis or metal hydroxyl complexes) in interstitial positions as depicted in Figure 1 c. According to bond valence considerations, the bridging alkali earth cation would need to provide ~ 0.67 vu to reach electrostatic neutrality on the linking oxygens (already supplied with ~ 1.33 vu from 3-fold coordinated C^{4+}). This requirement translates to 3-fold coordinated alkali earth cations. In the hypothetical case that a 3-valent cation (such as Y or La) serves as a bridging element, an average coordination number of 4.5 would be expected. All investigated elements in carbonate compositions studied here show coordination numbers above 6 and respective bond strengths below 0.5 vu. This is also true for the alkali earth Sr and excludes the investigated cations and elements with similar chemical behavior (such as Ca for Sr) from performing the bridging function as described in that model.

On the basis of the EXAFS-derived data and due to the close chemical resemblance of the *CAR* composition to the mineral nyerereite ($Na_2Ca(CO_3)_2$), a structural carbonate melt model in analogy to motifs found in this mineral (Bolotina et al., 2017; Gavryushkin et al., 2016) is suggested. Nyerereite is often observed in natural samples from Oldoinyo-Lengai and in quench products from Na-Ca-rich carbonate-silicate melts (Safonov et al., 2017 and ref. therein). Its structure is built by stacked blocks of Na-Ca-Na layers (Figure 30 a). The Na and Ca polyhedra are highly irregular with 6, 8 or 9 vertices. Bond lengths to oxygen range from 2.29 to 2.97 Å (with an average around 2.5 Å). The carbonate groups are oriented either nearly horizontally (Figure 30 c) or strongly inclined (60 – 70 ° with regard to the stacking, Figure 30 b) and show a distinct deviation from planarity (dihedral angles between 1 and 8.2 °). Carbonate oxygens can be linked to three or four adjacent Ca and Na polyhedra and the polyhedra are connected to the CO_3-group by sharing either corners or edges. Local structural units as found in nyerereite are potential candidates for also creating highly disordered glass and melt structures.

The observed EXAFS coordination environment of Sr in *CAR* melts with 7 to 8 oxygens at a distances averaging at 2.64 Å is in good agreement with the highly coordinated Ca or Na polyhedra found in nyerereite. The slight deviation of the average bond lengths may be explained by considering that (1) Sr is slightly bigger than Ca in nyerereite and (2) a generally increased bond length at high temperatures. Carbonate groups are coordinated by 8 to 9 metal cations and readily adapt to their electrostatic requirements. In such a flexible structure of CO_3-groups, even the higher charged Y and La could be easily incorporated in irregular coordination polyhedra with 7 to 9 oxygens at distances between 2.37 and 2.90 Å as found by EXAFS.

In fact, the concomitant MD study reveals that the carbonate groups are randomly distributed in *CAR40* melts, with ~ 7.7 coordinating Na, Ca and Y/Sr polyhedra. The coordination polyhedra of Na and Ca are rather distorted and are corner-, edge- or even face-sharing with the planar carbonate. Thus, the planar carbonate can be located in various coordination environments. This is in agreement with results from vibrational spectroscopy (Genge et al., 1995; Williams and Knittle, 2003), which provided evidence for at least two different structural sites of carbonate in melts and exceptionally quenched glasses.

A deeper look into the simulated structure may indicate that the simulated melt is percolated by channels (exemplary depicted Figure 25), which are present over the entire simulation run times. They give rise to the reduction in 2nd shell neighbors down to ~ 7.7 compared to 8 to 9 as found in the channel-free crystal structure of nyerereite (cf. Figure 30 b and c). However those channels may be an artefact in the simulation caused by confinement effect due to the restriced cell size and needs further verification in future studies.

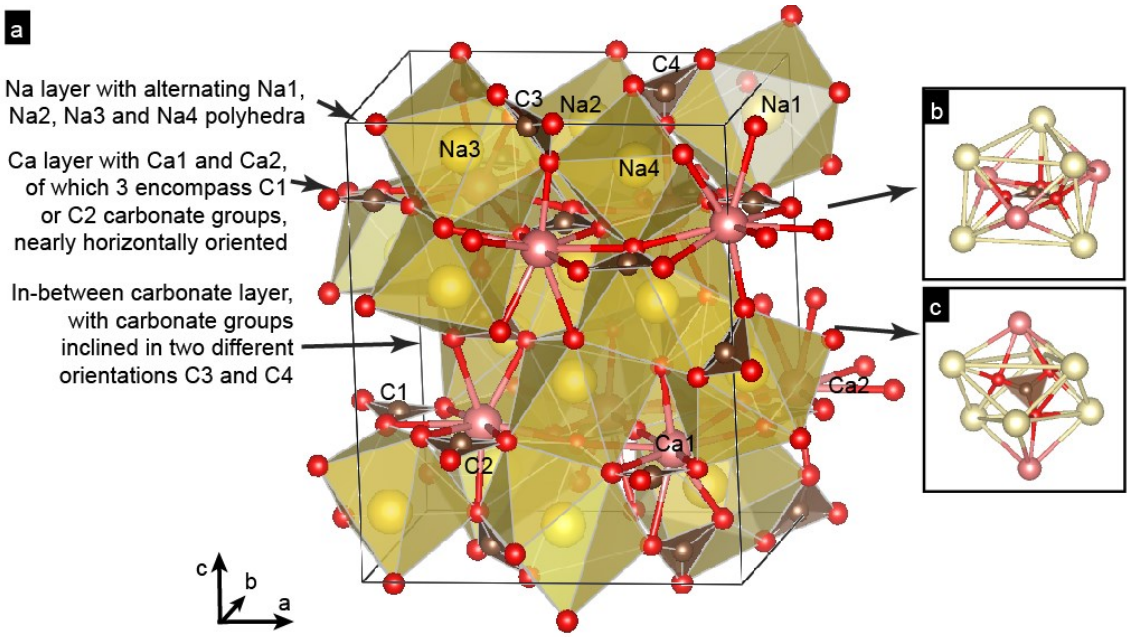

Figure 30: Crystal structure of nyerereite.
(a) Crystal structure of nyerereite, $Na_2Ca(CO_3)_2$, illustrating the stacking of Na-Ca-Na layers. Carbonate groups are either located within the Ca layer or in-between two Na-Ca-Na blocks. The coordination environment of the carbonate group (b) within the Ca layer as a three-capped trigonal Na_6Ca_3 prism and (c) in between two Na layers as two-capped Na_6Ca_2 octahedron. Created with the software VESTA (Momma and Izumi, 2008).

5 Conclusion

5.1 Implications

The experimental approach of combining laboratory EXAFS and simulation experiments revealed novel insights into trace element incorporation in sodium-rich silicate – carbonate melts and glasses at high pressure (up to 2 GPa) and temperature (up to 1500 °C in EXAFS and at 3000 K in simulations). EXAFS unveiled systematic variations of trace element bond lengths (coupled to coordination numbers), as a function of the CO_2 content. These patterns are further supported by coordination numbers derived in the simulations. MD also gives insights into general structural melt characteristics, such as mechanisms of carbonate incorporation in and polymerization of silicate melts. Additionally, it provides preliminary glimpses on phenomena such as unmixing in carbonate-rich silicate melt (simulated Y *sNC10*) or implications for a carbonate melt structure with channel-like features (simulated Y *CAR40*).

The inferred trends in local structural properties along the join CO_2-free *sSA* – C*AR* can be well correlated to trace element partitioning data reported by Veksler et al. (1998). The strong fractionation of Y into the silicate melts (similar to *sSA* composition) is explained by its preference for environments that allow for relatively short bond distances and are not associated with carbonate groups. Veksler et al. (1998) describe a moderate fractionation of La and a stronger fractionation of Sr into the carbonate melt (similar to *CAR* composition). This is consistent with the observation that La and Sr readily increase their coordination numbers with increasing carbonate content. A general enrichment in light rare earth elements over heavy rare earth elements is found in natural carbonatites all over the world (Jones et al., 2013) and is especially pronounced in the economically important light rare earth carbonate mineral bastnaesite. However, as suggested by Martin et al. (2013), rare earth element fractionation between carbonate and silicate melt strongly depends on the composition of the melts and may also feature strong enrichment of all rare earth elements or a general depletion of rare earth elements in the carbonate melt. The authors demonstrated that an increase in polymerization of the silicate melt leads to a shift of trace element partitioning toward the carbonatite melt. Simi-

larly, in contrast to the more polymerized *sSA* compositions, there are no significant changes observable in local environments of Y, La or Sr in the less polymerized *sNC* glasses and melts. Their highly flexible microsegregated network, as implied by the modified random-network model (e.g. Greaves, 1985; Henderson, 1995), provides a range of structural environments and easily adapts to the electrostatic requirements of both network modifiers and introduced carbonate. This is further emphasized by the wide range of incompatible elements and high CO_2 concentrations, that can be found in natural melt inclusions and matrix glasses investigated by de Moor et al. (2013) on samples of the carbonatite volcano Oldoinyo Lengai, of which *sNC* represents a simplified version.

In the sodium-rich silicate compositions investigated here, CO_2 is mainly incorporated as carbonate. Two main mechanisms for carbonate incorporation prevail: (1) the formation of non-bridging carbonates (T–CO_3), sharing one oxygen atom with a network former or (2) the formation of an isolated free carbonate group (FC). Minor shares of carbonate fulfill a bridging function between two network formers (T–CO_3–T), with a strong preference for $^{[4]}$Al over Si. Additionally, MD data suggest a rather rare structural unit of carbonate forming a non-bridging complex with a network former via two shared oxygens ($^{T}_{T}$= CO_3). Sodium-rich silicate melts at elevated temperatures contain around ~ 10 % molecular CO_2. As the fraction of molecular CO_2 is largely dependent on temperature, melts at lower temperatures contain less molecular CO_2 and glasses at ambient temperature almost none. The temperature dependence of the ratio CO_2:CO_3 has to be taken into account, when deducing models of C-bearing melts on the basis of data derived from glasses. Simply transferring information from glasses to melts will lead to a strong underestimation of CO_2 proportions in the melt. Prominent melt properties correlated to carbon in terms of its species or concentration are e.g. viscosity, (carbon) diffusivity, solubility or isotope fractionation (Morizet et al., 2001). Calorimetric studies on phonolitic and jadeitic glasses of Morizet et al. (2007) demonstrated that CO_2 concentration has basically no influence on the viscosity, which is in contradiction to previous falling-sphere studies (Brearley and Montana, 1989; White and Montana, 1990). Potential reasons for this discrepancy may be found in variations of composition or temperature and thus the type of C species present. Furthermore, it is suggested that carbonate diffusion in silicate melts is severely slower than mo-

lecular CO_2 diffusion (Spickenbom et al., 2010), which was confirmed by MD studies of Guillot and Sator (2011). Diffusion studies of Spickenbom et al. (2010) imposingly demonstrate, how CO_2 diffusion models, which incorporate the temperature dependence of C speciation (e.g. Nowak et al., 2004), compellingly describe transport processes in melts.

5.2 Outlook

Despite the unique insights obtained from the combined EXAFS and MD study, a wide range of aspects of silicate – carbonate melt structures remain subject to future research. One eminent step would be to design an in-depth MD study on carbonate systems in order to verify some of the suggestions made in this study. Uncertainties in the distribution of atomic configurations (e.g. over-representation of metastable configurational states) may be overcome by longer runtimes and larger sample sizes, i.e. larger number of atoms in the simulation. Larger simulations cells would also enable to scale down the concentration of the elements of interest, eventually reaching realistic trace element contents.

Ideally, the experimental set-up for EXAFS measurements would be optimized to allow for real trace element concentration not only in glasses, but also in melts. The major limiting factor for *in-situ* transmission EXAFS is given by the constrained sample thickness inside the nano-crystalline diamond capsule. Thus, fluorescence EXAFS is a potential candidate for measuring more realistic trace element concentrations in melts at *HPHT*. In addition to designing an alternative measurement arrangement for the press and the fluorescence detector, to allow for a high flux over a large solid angle, fundamental prerequisites are a highly brilliant X-ray source and extremely sensitive detectors. Complementary insights to EXAFS can be provided by XANES. Especially, the significant variations of the Y K-edge observed in this study are promising candidates for an in-depth XANES analysis. Another experimental approach to elucidate the chemical environment of Y and La in non-crystalline materials is given by NMR spectroscopy. These elements are remarkably suited for NMR in aluminosilicate systems, since ^{27}Al and ^{17}O NMR can be carried out without disturbances due to paramagnetism observed with other rare earth elements (Florian et al., 2007).

Future investigations should focus on the role of cation clustering. Especially high field strength cations such as rare earth elements are known to show a tendency for non-homogeneous distributions which can lead to cation clustering (Park et al., 2002; Schaller et al., 1999). There is good evidence from NMR and Raman spectroscopic studies on La's tendency to form clusters in sodium lanthanum silicate glasses (Schaller et al., 1999). Intensive MD studies on La_2O_3-Na_2O-SiO_2 glasses even confirmed La clustering to be independent of La concentration (Corrales and Park, 2002; Park and Corrales, 2002; Park et al., 2002). In the present MD study, this was not an issue as only a single atom of Y or Sr was introduced into the cell. However, it is not clear to which extend trace element clustering played a role in the EXAFS of glasses and melts. Here, clustering would severely affect the melt structure, as it creates micro-heterogeneities, which strongly differ from the Si-poor regions in the modified random network structure (cf. Figure 1 a). La as a high field strength element is actually able to strip away O anions from Si. This would force the network to adopt itself around the La to reach charge neutrality and to accommodate these larger cations (Corrales and Park, 2002). In a technological context, rare earth element clustering is the major limitation for designing optical amplifiers as used in optoelectronic applications (Auzel and Goldner, 2001; Monteil et al., 2004).

Another topic posed to question is the role of water in the investigated chemical system. Melt inclusion in nepheline crystals and matrix glasses in lapilli of Oldoinyo Lengai contain between 0.7 and 10.1 wt % H_2O (De Moor et al., 2013). The presented EXAFS study only considered two water-bearing samples in each trace element series. Additionally, increased bond lengths of water-bearing samples compared to their water-free counterparts are only minor and barely exceeding the experimental error. Thus, a detailed investigation of the influence of water on structural properties and quench effects was hindered. As water is the most significant volatile component in melts (Carroll and Holloway, 1994), its dissolution mechanism is strongly debated (Kohn, 2000; Le Losq et al., 2013, 2015; Moretti et al., 2014; Mysen et al., 1980; Stolper, 1982; Xue and Kanzaki, 2004, 2006, 2008). Even at low concentrations, H_2O in magmatic systems has a major impact on the structural characteristics and physical properties of melts, such as liquidus and solidus temperatures, viscosities, crystal nucleation rates

and diffusivities (Mysen and Richet, 2005). This may dramatically affect deep Earth processes such as source melting, magmatic degassing, magma rheology, transport or eruption style (Morizet et al., 2007, and references therein).

Eventually, further studies built upon the presented data will allow for the development of a comprehensive structural model on carbonate-silicate glasses and melts and serving well in explaining their physical properties and their control on related geological phenomena. This study documents a rewarding combination of (*in-situ*) EXAFS and molecular dynamics simulations. It provided unique insights into CO_2 and trace element incorporation in silicate-carbonate melts and glasses and into the carbonate melt structure and ultimately delivers a structural explanation for observed trace element partitioning in natural compositions.

References

Alder, B.J., and Wainwright, T.E. (1959). Studies in molecular dynamics. General method. Journal of Chemical Physics *31*, 459.

Ali, F., Chadwick, A.V., and Smith, M.E. (1997). EXAFS analysis of the structural evolution of gel-formed La_2O_3. Journal of Materials Chemistry *7*, 285–291.

Allen, M.P., and Tildesley, D.J. (1989). Computer Simulation of Liquids (New York, NY, USA: Clarendon Press).

Auzel, F., and Goldner, P. (2001). Towards rare-earth clustering control in doped glasses. Optical Materials *16*, 93–103.

Barker, S., Higgins, J., Elderfield, H., and Elderfield, H. (2003). The future of the carbon cycle: review, calcification response, ballast and feedback on atmospheric CO2. Philosophical Transactions of the Royal Society A: Mathematical, Physical and Engineering Sciences *361*, 1977–1999.

Behrens, P. (1992). X-ray absorption spectroscopy in chemistry: II. X-ray absorption near edge structure. TrAC Trends in Analytical Chemistry *11*, 237–244.

Bell, K., and Keller, J. (1995). Carbonatite Volcanism - Oldoinyo Lengai and the Petrogenesis of Natrocarbonatites (Berlin Heidelberg: Springer-Verlag).

Besson, J.M., Nelmes, R.J., Hamel, G., Loveday, J.S., Weill, G., and Hull, S. (1992). Neutron powder diffraction above 10 GPa. Physica B: Physics of Condensed Matter *180–181*, 907–910.

Bickmore, B.R., Craven, O., Wander, M.C.F., Checketts, H., Whitmer, J., Shurtleff, C., Yeates, D., Ernstrom, K., Andros, C., and Thompson, H. (2017). Bond valence and bond energy. American Mineralogist *102*, 804–812.

Blank, J.G., and Brooker, R.A. (1994). Experimental Studies of Carbon Dioxide in Silicate Melts: Solubility, Speciation, and Stable Carbon Isotope Behavior. In Volatiles in Magmas; Reviews in Mineralogy and Geochemistry 30, (Washington: Mineralogical Society of America), pp. 157–186.

Bolotina, N.B., Gavryushkin, P.N., Korsakov, A.V., Rashchenko, S.V., Seryotkin, Y.V., Golovin, A.V., Moine, B.N., Zaitsev, A.N., and Litasov, K.D. (2017). Incommensurately modulated twin structure of nyerereite Na1.64K0.36Ca(CO3)2. Acta Cryst B *73*, 276–284.

Botcharnikov, R., Freise, M., Holtz, F., and Behrens, H. (2005). Solubility of C-O-H mixtures in natural melts: new experimental data and application range of recent models. Annals of Geophysics *48*, 633–646.

Brearley, M., and Montana, A. (1989). The effect of CO2 on the viscosity of silicate liquids at high pressure. Geochimica et Cosmochimica Acta *53*, 2609–2616.

Brese, N.E., and O'Keeffe, M. (1991). Bond-Valence Parameters for Solids. Acta Crystallographica Section B *47*, 192–197.

Briois, V., Fonda, E., Belin, S., Barthe, L., Fontaine, C.L., Langlois, F., Ribbens, M., and Villain, F. (2011). SAMBA: The 4–40 keV X-ray absorption spectroscopy beamline at SOLEIL. In UVX 2010 - 10e Colloque Sur Les Sources Cohérentes et Incohérentes UV, VUV et X ; Applications et Développements Récents, (EDP Sciences), pp. 41–47.

Brooker, R.A., and Kjarsgaard, B.A. (2011). Silicate-carbonate liquid immiscibility and phase relations in the system SiO_2-Na_2O-Al_2O_3-Cao-CO_2 at 0.1-2.5 GPa with applications to carbonatite genesis. Journal of Petrology *52*, 1281–1305.

Brooker, R.A., Kohn, S.C., Holloway, J.R., McMillan, P.F., and Carroll, M.R. (1999). Solubility, speciation and dissolution mechanisms for CO_2 in melts on the $NaAlO_2$-SiO_2 join. Geochimica et Cosmochimica Acta *63*, 3549–3565.

Brooker, R.A., Kohn, S.C., Holloway, J.R., and McMillan, P.F. (2001a). Structural controls on the solubility of CO_2 in silicate melts part I: Bulk solubility data. Chemical Geology *174*, 225–239.

Brooker, R.A., Kohn, S.C., Holloway, J.R., and McMillan, P.F. (2001b). Structural controls on the solubility of CO_2 in silicate melts Part II: IR characteristic of carbonate groups in silicate glasses. Chemical Geology *174*, 241–254.

Brown, I.D. (2009). Recent developments in the methods and applications of the bond valence model. Chemical Reviews *109*, 6858–6919.

Brown, G.E., and Gibbs, G.V. (1970). Stereochemistry and ordering in the tetrahedral portion of silicates. The American Mineralogist *55*, 1587–1607.

Brown, G.E., Gibbs, G.V., and Ribbe, P.H. (1969). The nature and the variation in length of the Si-O and Al-O bonds in framework silicates. The American Mineralogist *54*, 1044–1061.

Brown, G.E., Farges, F., and Calas, G. (1995). X-ray Scattering and X-ray Spectroscopy Studies of Silicate Melts. In Structure, Dynamics, and Properties of Silicate Melts;, (Washington: Mineralogical Society of America), pp. 317–410.

Bunker, G. (1983). Application of the ratio method of EXAFS analysis to disordered systems. Nuclear Instruments and Methods In Physics Research *207*, 437–444.

Bunker, G. (2010). Introduction to XAFS: A Practical Guide to X-ray Absorption Fine Structure Spectroscopy (Cambridge University Press).

Calas, G., Henderson, G.S., and Stebbins, J.F. (2006). Glasses and Melts: Linking Geochemistry and Materials Science. ELEMENTS *2*, 265–268.

Carroll, M.R., and Holloway, J.R. (1994). Volatiles in Magmas (Washington: Mineralogical Society of America).

Clayden, N.J., Esposito, S., Aronne, A., and Pernice, P. (1999). Solid state 27Al NMR and FTIR study of lanthanum aluminosilicate glasses. Journal of Non-Crystalline Solids *258*, 11–19.

Cochain, B., Sanloup, C., de Grouchy, C., Crépisson, C., Bureau, H., Leroy, C., Kantor, I., and Irifune, T. (2015). Bromine speciation in hydrous silicate melts at high pressure. Chemical Geology *404*, 18–26.

Cormack, A.N., Yuan, X., and Park, B. (2001). Molecular Dynamics Simulations of Silicate Glasses and Melts. Glass Physics and Chemistry *27*, 28–36.

Cormier, L., Calas, G., Creux, S., Gaskell, P.H., Bouchet-Fabre, B., and Hannon, A.C. (1999). Environment around strontium in silicate and aluminosilicate glasses. Physical Review B *59*, 13517–13520.

Cormier, L., Ghaleb, D., Neuville, D.R., Delaye, J.-M., and Calas, G. (2003). Chemical dependence of network topology of calcium aluminosilicate glasses: a computer simulation study. Journal of Non-Crystalline Solids *332*, 255–270.

Corrales, L.R., and Park, B. (2002). Molecular dynamics simulation of La2O3–Na2O–SiO2 glasses. III. The driving forces of clustering. Journal of Non-Crystalline Solids *311*, 118–129.

Creux, S., Bouchet-Fabre, B., and Gaskell, P.H. (1995). Anomalous wide angle X-ray

scattering study of strontium silicate and aluminosilicate glasses. Journal of Non-Crystalline Solids *192–193*, 360–363.

Crichton, W.A., and Mezouar, M. (2002). Noninvasive pressure and temperature estimation in large-volume apparatus by equation-of-state cross-calibration. High Temperatures. High Pressures *34*, 235–242.

Crozier, E.D. (1997). A review of the current status of XAFS spectroscopy. Nuclear Instruments and Methods in Physics Research Section B: Beam Interactions with Materials and Atoms *133*, 134–144.

Cygan, R.T., and Kubicki, J.D. (2001). Molecular Modeling Theory: Applications in the Geosciences; Reviews in Mineralogy and Geochemistry 42 (Mineralogical Society of America, Washington).

D'Angelo, P., Nolting, H.F., and Pavel, N.V. (1996). Evidence for multielectron resonances at the Sr *K* edge. Physical Review A *53*, 798–805.

Daryl Crozier, E. (1995). Impact of the asymmetric pair distribution function in the analysis of XAFS. Physica B: Physics of Condensed Matter *208–209*, 330–333.

Dasgupta, R., and Hirschmann, M.M. (2010). The deep carbon cycle and melting in Earth's interior. Earth and Planetary Science Letters *298*, 1–13.

Dasgupta, R., Hirschmann, M.M., and Smith, N.D. (2007). Water follows carbon: CO_2 incites deep silicate melting and dehydration beneath mid-ocean ridges. Geology *35*, 135–138.

De Moor, J.M., Fischer, T.P., King, P.L., Botcharnikov, R.E., Hervig, R.L., Hilton, D.R., Barry, P.H., Mangasini, F., and Ramirez, C. (2013). Volatile-rich silicate melts from Oldoinyo Lengai volcano (Tanzania): Implications for carbonatite genesis and eruptive behavior. Earth and Planetary Science Letters *361*, 379–390.

De Villiers, J.P.R. (1971). Crystal Structures of Aragonite, Strontianite, and Witherite. The American Mineralogist *56*, 758–767.

Dingwell, D.B., and Webb, S.L. (1990). Relaxation in silicate melts. European Journal of Mineralogy 427–451.

Dobson, D.P., Jones, A.P., Rabe, R., Sekine, T., Kurita, K., Taniguchi, T., Kondo, T., Kato, T., Shimomura, O., and Urakawa, S. (1996). In-situ measurement of viscosity and density of carbonate melts at high pressure. Earth and Planetary Science Letters *143*, 207–215.

Du, J. (2009). Molecular dynamics simulations of the structure and properties of low silica yttrium aluminosilicate glasses. Journal of the American Ceramic Society *92*, 87–95.

Dubinsky, E.V., and Stebbins, J.F. (2015). Quench rate and temperature effects on framework ordering in aluminosilicate melts. American Mineralogist *91*, 753–761.

Eisenberger, P., and Brown, G.S. (1979). The study of disordered systems by EXAFS: Limitations. Solid State Communications *29*, 481–484.

Farges, F. (1991). Structural environment around Th^{4+} in silicate glasses: Implications for the geochemistry of incompatible Me^{4+} elements. Geochimica et Cosmochimica Acta *55*, 3303–3319.

Farges, F., Ponader, C.W., and Brown, G.E. (1991). Structural environments of incompatible elements in silicate glass/melt systems: I. Zirconium at trace levels. Geochimica et Cosmochimica Acta *55*, 1563–1574.

Farges, F., Ponader, C.W., Calas, G., and Brown, G.E. (1992). Structural environments of incompatible elements in silicate

glass/melt systems: II. U^{IV}, U^{VI}. Geochimica et Cosmochimica Acta *56*, 4205–4220.

Farges, F., Brown, G.E., Navrotsky, A., Gan, H., and Rehr, J.J. (1996). Coordination chemistry of Ti(IV) in silicate glasses and melts: II. Glasses at ambient temperature and pressure. Geochimica et Cosmochimica Acta *60*, 3039–3053.

Filipponi, A. (1994). The radial distribution function probed by X-ray absorption spectroscopy. J. Phys.: Condens. Matter *6*, 8415.

Filipponi, A. (2001). EXAFS for liquids. Journal of Physics: Condensed Matter *13*, 23–60.

Fine, G., and Stolper, E. (1985). The speciation of carbon dioxide in sodium aluminosilicate glasses. Contributions to Mineralogy and Petrology *91*, 105–121.

Florian, P., Sadiki, N., Massiot, D., and Coutures, J.P. (2007). ^{27}Al NMR study of the structure of lanthanum- and yttrium-based aluminosilicate glasses and melts. Journal of Physical Chemistry B *111*, 9747–9757.

Fogel, R.A., and Rutherford, M.J. (1990). The solubility of carbon dioxide in rhyolitic melts; a quantitative FTIR study. American Mineralogist *75*, 1311–1326.

Galoisy, L., and Calas, G. (1993). Structural environment of nickel in silicate glass/melt systems: Part 2. Geochemical implications. Geochimica et Cosmochimica Acta *57*, 3627–3633.

Gavryushkin, P.N., Thomas, V.G., Bolotina, N.B., Bakakin, V.V., Golovin, A.V., Seryotkin, Y.V., Fursenko, D.A., and Litasov, K.D. (2016). Hydrothermal Synthesis and Structure Solution of $Na_2Ca(CO_3)_2$: "Synthetic Analogue" of Mineral Nyerereite. Crystal Growth & Design *16*, 1893–1902.

Genge, M.J., Jones, A.P., and Price, G.D. (1995). An infrared and Raman study of carbonate glasses: implications for the structure of carbonatite magmas. Geochimica et Cosmochimica Acta *59*, 927–937.

Gibbs, G.V., Hamil, M.M., Louisnathan, S.J., Bartell, L.S., and Yow, H. (1972). Correlation between Si-O bond length, Si-O-Si angle and bond overlap populations calculated using extended Hückel moleculare orbital theory. The American Mineralogist *57*, 1578–1613.

Goedecker, S., Allen, M.P., and Hutter, J. (1996). Separable dual-space Gaussian pseudopotentials. Phys. Rev., B Condens. Matter *54*, 1703–1710.

Greaves, G.N. (1985). EXAFS and the structure of glass. Journal of Non-Crystalline Solids *71*, 203–217.

Green, T.H. (1994). Experimental studies of trace-element partitioning applicable to igneous petrogenesis — Sedona 16 years later. Chemical Geology *117*, 1–36.

Grégoire, M., Moine, B.N., O'reilly, S.Y., Cottin, J.Y., and Giret, A. (2000). Trace Element Residence and Partitioning in Mantle Xenoliths Metasomatized by Highly Alkaline, Silicate- and Carbonate-rich Melts (Kerguelen Islands, Indian Ocean). J. Petrology *41*, 477–509.

Guillot, B., and Sator, N. (2011). Carbon dioxide in silicate melts: A molecular dynamics simulation study. Geochimica et Cosmochimica Acta *75*, 1829–1857.

Gurman, S.J. (1995). Interpretation of EXAFS Data. J Synchrotron Rad, J Synchrotron Radiat *2*, 56–63.

Haigis, V. (2013). Trace elements in silicate melts and the thermal conductivity of the Earth's deep mantle: insights from atomistic modeling of geomaterials. Dissertation. Freie Universität Berlin.

Haigis, V., Salanne, M., Simon, S., Wilke, M., and Jahn, S. (2013). Molecular dynamics simulations of Y in silicate melts and implications for trace element partitioning. Chemical Geology *346*, 14–21.

Hanwell, M.D., Curtis, D.E., Lonie, D.C., Vandermeersch, T., Zurek, E., and Hutchison, G.R. (2012). Avogadro: an advanced semantic chemical editor, visualization, and analysis platform. Journal of Cheminformatics *4*, 17.

Hardacre, C. (2005). Application of EXAFS to Molten Salts and Ionic Liquid Technology. Annual Review of Materials Research *35*, 29–49.

Hazen, R.M., Downs, R.T., and Prewitt, C.T. (2000). Principles of Comparative Crystal Chemistry. In High-Pressure and High-Temperature Crystal Chemistry, (Washington: Mineralogical Society of America), pp. 1–33.

Hazen, R.M., Hemley, R.J., and Mangum, A.J. (2012). Carbon in Earth's interior: Storage, cycling, and life. Eos Trans. AGU *93*, 17–18.

Hazen, R.M., Jones, A.P., and Baros, J.A. (2013). Carbon in Earth (Washington: Mineralogical Society of America).

Henderson, G.S. (1995). A Si K-edge EXAFS/XANES study of sodium silicate glasses. Journal of Non-Crystalline Solids *183*, 43–50.

Henderson, G.S. (2005). The Structure of Silicate Melts: A Glass Perspective. Can Mineral *43*, 1921–1958.

Henderson, P., Nolan, J., Cunningham, G.C., and Lowry, R.K. (1985). Structural controls and mechanisms of diffusion in natural silicate melts. Contr. Mineral. and Petrol. *89*, 263–272.

Hohenberg, P., and Kohn, W. (1964). Inhomogeneous Electron Gas. Phys. Rev. *136*, B864–B871.

Hoover, W.G. (1985). Canonical dynamics: Equilibrium phase-space distributions. Physical Review A *31*, 1695–1697.

Hoover, W.G., and Rossj, M. (1971). Statistical theories of melting. Contemporary Physics *12*, 339–356.

Huang, C., and Cormack, A.N. (1990). The structure of sodium silicate glass. The Journal of Chemical Physics *93*, 8180–8186.

Hutter, J., Iannuzzi, M., Schiffmann, F., and VandeVondele, J. (2014). CP2K: Atomistic simulations of condensed matter systems. Wiley Interdisciplinary Reviews. Computational Molecular Science *4*, 15–25.

Iftekhar, S., Pahari, B., Okhotnikov, K., Jaworski, A., Stevensson, B., Grins, J., and Edén, M. (2012). Properties and structures of RE_2O_3-Al_2O_3-SiO_2 (RE = Y, Lu) glasses probed by molecular dynamics simulations and solid-state NMR: the roles of aluminum and rare-earth ions for dictating the microhardness. Journal of Physical Chemistry C *116*, 18394–18406.

Irifune, T., Kurio, A., Sakamoto, S., Inoue, T., and Sumiya, H. (2003). Materials: Ultrahard polycrystalline diamond from graphite. Nature *421*, 599–600.

Irving, A.J. (1978). A review of experimental studies of crystal/liquid trace element partitioning. Geochimica et Cosmochimica Acta *42*, 743–770.

Jabraoui, H., Achhal, E.M., Hasnaoui, A., Garden, J.-L., Vaills, Y., and Ouaskit, S. (2016). Molecular dynamics simulation of thermodynamic and structural properties of silicate glass: Effect of the alkali oxide modifiers. Journal of Non-Crystalline Solids *448*, 16–26.

Jaworski, A., Stevensson, B., Pahari, B., Okhotnikov, K., and Edén, M. (2012). Local structures and Al/Si ordering in lanthanum aluminosilicate glasses explored by advanced ^{27}Al NMR experiments and molecular dynamics simulations. Physical Chemistry Chemical Physics *14*, 15866.

Jendrzejewski, N., Trull, T.W., Pineau, F., and Javoy, M. (1997). Carbon solubility in Mid-Ocean Ridge basaltic melt at low pressures (250–1950 bar). Chemical Geology *138*, 81–92.

Johnson, J.A., Urquidi, J., Holland, D., Johnson, C.E., and Appelyard, P.G. (2007). Strontium environment transition in tin silicate glasses by neutron and X-ray diffraction. Journal of Non-Crystalline Solids *353*, 4084–4092.

Jones, A.P., Genge, M., and Carmody, L. (2013). Carbonate Melts and Carbonatites. In Carbon in Earth, (Washington: Mineralogical Society of America), pp. 289–322.

Jones, J.H., Walker, D., Pickett, D.A., Murrell, M.T., and Beattie, P. (1995). Experimental investigations of the partitioning of Nb, Mo, Ba, Ce, Pb, Ra, Th, Pa, and U between immiscible carbonate and silicate liquids. Geochimica et Cosmochimica Acta *59*, 1307–1320.

Jund, P., Kob, W., and Jullien, R. (2001). Channel diffusion of sodium in a silicate glass.

Kamenetsky, M.B., Sobolev, A.V., Kamenetsky, V.S., Maas, R., Danyushevsky, L.V., Thomas, R., Pokhilenko, N.P., and Sobolev, N.V. (2004). Kimberlite melts rich in alkali chlorides and carbonates: A potent metasomatic agent in the mantle. Geology *32*, 845.

Kasting, J.F., and Catling, D. (2003). Evolution of a Habitable Planet. Annual Review of Astronomy and Astrophysics *41*, 429–463.

Kevorkov, A.M., Karyagin, V.F., Munchaev, A.I., Uyukin, E.M., Bolotina, N.B., Chernaya, T.S., Bagdasarov, K.S., and Simonov, V.I. (1995). Y_2O_3 single crystals: Growth, structure, and photoinduced effects. Crystallography Reports *40*, 23–26.

Klaudius, J., and Keller, J. (2006). Peralkaline silicate lavas at Oldoinyo Lengai, Tanzania. Lithos *91*, 173–190.

Kohn, S.C. (2000). The dissolution mechanisms of water in silicate melts; a synthesis of recent data. Mineralogical Magazine *64*, 389–408.

Kohn, W., and Sham, L.J. (1965). Self-consistent equations including exchange and correlation effects. Phys. Rev. *140*, A1133–A1138.

Kohn, S.C., Charnock, J.M., Henderson, C.M.B., and Greaves, G.N. (1990). The structural environments of trace elements in dry and hydrous silicate glasses; a manganese and strontium K-edge X-ray absorption spectroscopic study. Contributions to Mineralogy and Petrology *105*, 359–368.

Kohn, S.C., Brooker, R.A., and Dupree, R. (1991). ^{13}C MAS NMR: A method for studying CO_2 speciation in glasses. Geochimica et Cosmochimica Acta *55*, 3879–3884.

Konschak, A., and Keppler, H. (2014). The speciation of carbon dioxide in silicate melts. Contributions to Mineralogy and Petrology *167*, 1–13.

Lacy, E.D. (1963). Aluminium in glasses and melts. Phys. Chem. Glasses *4*, 234–238.

Larson, E.M., Ellison, A.J.G., Lytle, F.W., Navrotsky, A., Greegor, R.B., and Wong, J. (1991). XAS study of lanthanum coordination environments in glasses of the system K_2O-SiO_2-La_2O_3. Journal of Non-Crystalline Solids *130*, 260–272.

Le Losq, C., Moretti, R., and Neuville, D.R. (2013). Speciation and amphoteric behaviour of water in aluminosilicate melts and glasses: high-temperature Raman spectroscopy and reaction equilibria. European Journal of Mineralogy *25*, 777–790.

Le Losq, C., Mysen, B.O., and Cody, G.D. (2015). Water and magmas: insights about the water solution mechanisms in alkali silicate melts from infrared, Raman, and $^{29\$}$Si solid-state NMR spectroscopies. Progress in Earth and Planetary Science *2*, 22.

Le Maitre, R.W., Streckeisen, A., Zanettin, B., Bas, M.J.L., Bonin, B., and Bateman, P. (2005). Igneous Rocks: A Classification and Glossary of Terms: Recommendations of the International Union of Geological Sciences Subcommission on the Systematics of Igneous Rocks (Cambridge ; New York: Cambridge University Press).

Lee, S.K., and Stebbins, J.F. (1999). The degree of aluminum avoidance in aluminosilicate glasses. American Mineralogist *84*, 937–945.

Lee, S.K., and Stebbins, J.F. (2000). Al–O–Al and Si–O–Si sites in framework aluminosilicate glasses with Si/Al=1: quantification of framework disorder. Journal of Non-Crystalline Solids *270*, 260–264.

Lee, W.-J., and Wyllie, P.J. (1996). Liquid Immiscibility in the Join $NaAlSi_3O_8$–$CaCO_3$ to 2.5 GPa and the Origin of Calciocarbonatite Magmas. J. Petrology *37*, 1125–1152.

Liu, Q., and Lange, R.A. (2003). New density measurements on carbonate liquids and the partial molar volume of the $CaCO_3$ component. Contributions to Mineralogy and Petrology *146*, 370–381.

Loewenstein, W. (1954). The distribution of aluminum in the tetrahedra of silicates and aluminates. American Mineralogist *39*, 92–96.

Marchi, J., Morais, D.S., Schneider, J., Bressiani, J.C., and Bressiani, A.H.A. (2005). Characterization of rare earth aluminosilicate glasses. Journal of Non-Crystalline Solids *351*, 863–868.

Mariano, A.N. (1989). Nature of economic mineralization in carbonatites and related rocks. In Carbonatites: Genesis and Evolution, (London: Unwin Hyman), pp. 149–176.

Martens, R., and Müller-Warmuth, W. (2000). Structural groups and their mixing in borosilicate glasses of various compositions - an NMR study. Journal of Non-Crystalline Solids *265*, 167–175.

Martin, L.H., Schmidt, M.W., Mattsson, H.B., and Guenther, D. (2013). Element Partitioning between Immiscible Carbonatite and Silicate Melts for Dry and H_2O-bearing Systems at 1-3 GPa. Journal of Petrology *54*, 2301–2338.

Martin, L.H.J., Schmidt, M.W., Mattsson, H.B., Ulmer, P., Hametner, K., and Günther, D. (2012). Element partitioning between immiscible carbonatite–kamafugite melts with application to the Italian ultrapotassic suite. Chemical Geology *320–321*, 96–112.

Mathon, O., Beteva, A., Borrel, J., Bugnazet, D., Gatla, S., Hino, R., Kantor, I., Mairs, T., Munoz, M., Pasternak, S., et al. (2015). The time-resolved and extreme conditions XAS (Texas) facility at the European Synchrotron Radiation Facility: The general-purpose EXAFS bending-magnet beamline BM23. Journal of Synchrotron Radiation *22*, 1548–1554.

McIntire, W.L. (1963). Trace element partition coefficients—a review of theory and applications to geology. Geochimica et Cosmochimica Acta *27*, 1209–1264.

McKeown, D.A., Kot, W.K., and Pegg, I.L. (2003). X-ray absorption studies of the local strontium environments in borosilicate was-

te glasses. Journal of Non-Crystalline Solids *317*, 290–300.

McMillan, P.F., and Wolf, G.H. (1995). Vibrational spectroscopy of silicate liquids; Reviews in Mineralogy and Geochemistry 32 (Washington: Mineralogical Society of America).

Momma, K., and Izumi, F. (2008). VESTA: A three-dimensional visualization system for electronic and structural analysis. Journal of Applied Crystallography *41*, 653–658.

Monteil, A., Chaussedent, S., Alombert-Goget, G., Gaumer, N., Obriot, J., Ribeiro, S.J.L., Messaddeq, Y., Chiasera, A., and Ferrari, M. (2004). Clustering of rare earth in glasses, aluminum effect: experiments and modeling. Journal of Non-Crystalline Solids *348*, 44–50.

Morard, G., Mezouar, M., Rey, N., Poloni, R., Merlen, A., Le Floch, S., Toulemonde, P., Pascarelli, S., San-Miguel, A., Sanloup, C., et al. (2007). Optimization of Paris–Edinburgh press cell assemblies for in situ monochromatic X-ray diffraction and X-ray absorption. High Pressure Research *27*, 223–233.

Moretti, R., Le Losq, C., and Neuville, D.R. (2014). The amphoteric behavior of water in silicate melts from the point of view of their ionic-polymeric constitution. Chemical Geology *367*, 23–33.

Morgan, G.B., and London, D. (1996). Optimizing the electron microprobe analysis of hydrous alkali aluminosilicate glasses. American Mineralogist *81*, 1176–1185.

Morizet, Y., Kohn, S.C., and Brooker, R.A. (2001). Annealing experiments on CO_2–bearing jadeite glass: an insight into the true temperature dependence of CO_2 speciation in silicate melts. Mineralogical Magazine *65*, 701–707.

Morizet, Y., Nichols, A.R.L.K., Brooker, R.A., and Dingwell, D.B. (2007). The influence of H2O and CO2 on the glass transition temperature: insights into the effects of volatiles on magma viscosity. European Journal of Mineralogy 657–669.

Mysen, B.O. (1983). The Structure of Silicate Melts. Annual Review of Earth and Planetary Sciences *11*, 75–97.

Mysen, B.O. (1990). Relationships between silicate melt structure and petrologic processes. Earth Science Reviews *27*, 281–365.

Mysen, B.O., and Richet, P. (2005). Silicate Glasses and Melts: Properties and Structure (Elsevier).

Mysen, B.O., Virgo, D., Harrison, W.J., and Scarfe, C.M. (1980). Solubility mechanisms of H_2O in silicate melts at high pressures and temperatures: a Raman spectroscopic study. American Mineralogist *65*, 900–914.

Navrotsky, A. (1996). Thermochemistry of Borosilicate Melts and Glasses - From Pyrex to Pegmatites. In Boron: Mineralogy, Petrology, and Geochemistry; Reviews in Mineralogy 33, (Washington: Mineralogical Society of America), pp. 165–179.

Nesbitt, H.W., Bancroft, G.M., Henderson, G.S., Ho, R., Dalby, K.N., Huang, Y., and Yan, Z. (2011). Bridging, non-bridging and free (O2–) oxygen in Na2O-SiO2 glasses: An X-ray Photoelectron Spectroscopic (XPS) and Nuclear Magnetic Resonance (NMR) study. Journal of Non-Crystalline Solids *357*, 170–180.

Newville, M. (2014). Fundamentals of XAFS. In Spectroscopic Methods in Mineralogy and Material Sciences, G.S. Henderson, D.R. Neuville, and R.T. Downs, eds. pp. 33–74.

Ni, H., and Keppler, H. (2013a). Carbon in Silicate Melts; Reviews in Mineralogy and Geochemistry 75. (Washington: Mineralogical Society of America), pp. 251–287.

Ni, H., and Keppler, H. (2013b). Carbon in Silicate Melts. Reviews in Mineralogy and Geochemistry 75 *75*, 251–287.

Nosé, S. (1984). A molecular dynamics method for simulations in the canonical ensemble. Molecular Physics *52*, 255–268.

Nowak, M., Porbatzki, D., Spickenbom, K., and Diedrich, O. (2003). Carbon dioxide speciation in silicate melts: a restart. Earth and Planetary Science Letters *207*, 131–139.

Nowak, M., Schreen, D., and Spickenbom, K. (2004). Argon and CO2 on the race track in silicate melts: A tool for the development of a CO2 speciation and diffusion model. Geochimica et Cosmochimica Acta *68*, 5127–5138.

O'Day, P.A., Newville, M., Neuhoff, P.S., Sahai, N., and Carroll, S.A. (2000). X-Ray Absorption Spectroscopy of Strontium(II) Coordination: I. Static and Thermal Disorder in Crystalline, Hydrated, and Precipitated Solids and in Aqueous Solution. Journal of Colloid and Interface Science *222*, 184–197.

Okhotnikov, K., Stevensson, B., and Edén, M. (2013). New interatomic potential parameters for molecular dynamics simulations of rare-earth (RE = La, Y, Lu, Sc) aluminosilicate glass structures: exploration of RE^{3+} field-strength effects. Physical Chemistry Chemical Physics *15*, 15041–55.

Pace, N.R. (2001). The universal nature of biochemistry. Proc. Natl. Acad. Sci. U.S.A. *98*, 805–808.

Pal'yanov, Y.N., Sokol, A.G., Borzdov, Y.M., Khokhryakov, A.F., and Sobolev, N.V. (1999). Diamond formation from mantle carbonate fluids. Nature *400*, 417–418.

Park, B., and Corrales, L.R. (2002). Molecular dynamics simulation of La_2O_3–Na_2O–SiO_2 glasses. II. The clustering of La^{3+} cations. Journal of Non-Crystalline Solids *311*, 107–117.

Park, B., Li, H., and Corrales, L.R. (2002). Molecular dynamics simulation of La_2O_3–Na_2O–SiO_2 glasses. I. The structural role of La3+ cations. Journal of Non-Crystalline Solids *297*, 220–238.

Penner-Hahn, J.E. (2005). X-ray Absorption Spectroscopy. In ELS, (John Wiley & Sons, Ltd), pp. 1–24.

Perdew, J.P., Burke, K., and Ernzerhof, M. (1996). Generalized Gradient Approximation Made Simple. Phys. Rev. Lett. *77*, 3865–3868.

Peters, P.M., and Houde-Walter, S.N. (1997). X-ray absorption fine structure determination of the local environment of Er^{3+} in glass. Appl. Phys. Lett. *70*, 541–543.

Peterson, T.D. (1989). Peralkaline nephelinites. I. Comparative petrology of Shombole and Oldoinyo L'engai, East Africa. Contr. Mineral. and Petrol. *101*, 458–478.

Peterson, T.D. (1990). Petrology and genesis of natrocarbonatite. Contributions to Mineralogy and Petrology *105*, 143–155.

Petibon, C.M., Kjarsgaard, B.A., Jenner, G.A., and Jackson, S.E. (1998). Phase Relationships of a Silicate-bearing Natrocarbonatite from Oldoinyo Lengai at 20 and 100 MPa. Journal of Petrology *39*, 2137–2151.

Pierson, H.O. (2012). Handbook of Carbon, Graphite, Diamonds and Fullerenes: Processing, Properties and Applications (William Andrew).

Pohlenz, J., Pascarelli, S., Mathon, O., Belin, S., Shiryaev, A., Safonov, O., Veligzhanin, A., Murzin, V., Irifune, T., and Wilke, M. (2016). Structural properties of sodium-rich carbonate-silicate melts: An in-situ high-pressure EXAFS study on Y and Sr. J. Phys.: Conf. Ser. *712*, 012083.

Ponader, C.W., and Brown, G.E. (1989). Rare earth elements in silicate glassmelt systems:

I. Effects of composition on the coordination environments of La, Gd, and Yb. Geochimica et Cosmochimica Acta *53*, 2893–2903.

Post, W.M., Peng, T.-H., Emanuel, W.R., King, A.W., Dale, V.H., and Deangelis, D.L. (1990). The Global Carbon Cycle. American Scientist *78*, 310–326.

Pozdnyakova, I., Sadiki, N., Hennet, L., Cristiglio, V., Bytchkov, A., Cuello, G., Coutures, J., and Price, D. (2008). Structures of lanthanum and yttrium aluminosilicate glasses determined by X-ray and neutron diffraction. Journal of Non Crystalline Solids *354*, 2038–2044.

Ravel, B., and Newville, M. (2005). ATHENA, ARTEMIS, HEPHAESTUS: Data analysis for X-ray absorption spectroscopy using IFEFFIT. Journal of Synchrotron Radiation *12*, 537–541.

Rehr, J.J., and Albers, R.C. (2000). Theoretical approaches to x-ray absorption fine structure. Rev. Mod. Phys. *72*, 621–654.

Rehr, J.J., Kas, J.J., Vila, F.D., Prange, M.P., and Jorissen, K. (2010). Parameter-free calculations of X-ray spectra with FEFF9. Physical Chemistry Chemical Physics *12*, 5503–5513.

Rosa, A., Pohlenz, J., de Grouchy, C., Cochain, B., Kono, Y., Pasternak, S., Mathon, O., Irifune, T., and Wilke, M. (2016). In-situ characterisation of liquid network structure at high pressure and temperature using XAS coupled with Paris-Edinburgh Press. High Pressure Research *Online*, 1477–2299.

Rossano, S., Ramos, A., Delaye, J.-M., Creux, S., Filipponi, A., Brouder, C., and Calas, G. (2000). EXAFS and Molecular Dynamics combined study of CaO − FeO − 2SiO2 glass. New insight into site significance in silicate glasses. Eurephysics Letters *49*, 597–602.

Rossano, S., Farges, F., Ramos, A., Delaye, J.-M., and Brown, G.E. (2002). Bond valence in silicate glasses. Journal of Non-Crystalline Solids *304*, 167–173.

Roux, J., Holtz, F., Lefevre, A., and Schulze, F. (1994). A reliable high-temperature setup for internally heated pressure vessels; applications to silicate melt studies. American Mineralogist *79*, 1145–1149.

Safonov, O.G., Shiryaev, A.A., Tyurnina, A.V., and Huthwelker, T. (2017). Structural features of quench products of melts in the chloride-carbonate-silicate systems revealed by vibrational and X-ray spectroscopy. Petrology *25*, 23–41.

Schaller, T., Stebbins, J.F., and Wilding, M.C. (1999). Cation clustering and formation of free oxide ions in sodium and potassium lanthanum silicate glasses: nuclear magnetic resonance and Raman spectroscopic findings. Journal of Non-Crystalline Solids *243*, 146–157.

Schiller, G. (1986). Die Kristallstrukturen von Ce_2O_3 (A-Form), $LiCeO_2$ und CeF_3 - ein Beitrag zur Kristallchemie des dreiwertigen Cers. Dissertation, in German. Drei-Eck-Verl. Löchner.

Schimel, D.S. (1995). Terrestrial ecosystems and the carbon cycle. Global Change Biology *1*, 77–91.

Seifert, R. (2013). Compressibility of volatile-bearing magmatic liquids. Dissertation. ETH-Zürich.

Seifert, F.A., Mysen, B.O., and Virgo, D. (1981). Structural similarity of glasses and melts relevant to petrological processes. Geochimica et Cosmochimica Acta *45*, 1879–1884.

Seto, Y., Hamane, D., Nagai, T., and Fujino, K. (2008). Fate of carbonates within oceanic plates subducted to the lower mantle, and a possible mechanism of diamond formation. Physics and Chemistry of Minerals *35*, 223–229.

Shannon, R.D. (1976). Revised effective ionic radii and systematic studies of interatomic distances in halides and chalcogenides. Acta Cryst A *32*, 751–767.

Shatskiy, A., Sharygin, I.S., Litasov, K.D., Borzdov, Y.M., Palyanov, Y.N., and Ohtani, E. (2013). New experimental data on phase relations for the system Na2CO3-CaCO3 at 6 GPa and 900–1400 °C. American Mineralogist *98*, 2164–2171.

Shatskiy, A., Gavryushkin, P.N., Litasov, K.D., Koroleva, O.N., Kupriyanov, I.N., Borzdov, Y.M., Sharygin, I.S., Funakoshi, K., Palyanov, Y.N., and Ohtani, E. (2015). Na-Ca carbonates synthesized under upper-mantle conditions: Raman spectroscopic and X-ray diffraction studies. European Journal of Mineralogy *27*, 175–184.

Sifré, D., Gardés, E., Massuyeau, M., Hashim, L., Hier-Majumder, S., and Gaillard, F. (2014). Electrical conductivity during incipient melting in the oceanic low-velocity zone. Nature *509*, 81–5.

Sigurdsson, H., Houghton, B., McNutt, S., Rymer, H., and Stix, J. (2015). The Encyclopedia of Volcanoes (Amsterdam: Academic Press).

Simon, S. (2016). Der Einfluss der Koordination von Spurenelementen in silikatischen und aluminosilikatischen Schmelzen auf Elementverteilungsprozesse in magmatischen Systemen. Dissertation, in German. Universität Potsdam.

Simon, S., Wilke, M., Chernikov, R., Klemme, S., and Hennet, L. (2013). The influence of composition on the local structure around yttrium in quenched silicate melts — Insights from EXAFS. Chemical Geology *346*, 3–13.

Smith, W., Greaves, G.N., and Gillan, M.J. (1995). Computer simulation of sodium disilicate glass. The Journal of Chemical Physics *103*, 3091–3097.

Spickenbom, K., Sierralta, M., and Nowak, M. (2010). Carbon dioxide and argon diffusion in silicate melts: Insights into the CO2 speciation in magmas. Geochimica et Cosmochimica Acta *74*, 6541–6564.

Stebbins, J.F. (1995). Dynamics and structure of silicate and oxide melts; nuclear magnetic resonance studies. In Structure, Dynamics, and Properties of Silicate Melts; Reviews in Mineralogy 32, (Washington: Mineralogical Society of America), pp. 191–246.

Stebbins, J.F., McMillan, P.F., and Dingwell, D.B. (1995). Structure, Dynamics, and Properties of Silicate Melts (Washington: Mineralogical Society of America).

Stebbins, J.F., Lee, S.K., and Oglesby, J.V. (1999). Al-O-Al oxygen sites in crystalline aluminates and aluminosilicate glasses: High-resolution oxygen-17 NMR results. American Mineralogist *84*, 983–986.

Stern, E.A., Ma, Y., Hanske-Petitpierre, O., and Bouldin, C.E. (1992). Radial distribution function in x-ray-absorption fine structure. Phys. Rev. B *46*, 687–694.

Stolper, E. (1982). The speciation of water in silicate melts. Geochimica et Cosmochimica Acta *46*, 2609–2620.

Toplis, M.J., Dingwell, D.B., and Lenci, T. (1997). Peraluminous viscosity maxima in Na2O–Al2O3 –SiO2 liquids: the role of oxygen triclusters in silicate melts. Geochim. Cosmochim. Acta *61*, 2605–2612.

Trcera, N., Rossano, S., Madjer, K., and Cabaret, D. (2011). Contribution of molecular dynamics simulations and ab initio calculations to the interpretation of Mg K-edge experimental XANES in K(2)O-MgO-3SiO(2) glass. J Phys Condens Matter *23*, 255401.

Treiman, A.H. (1989). Carbonatite Magma: Properties and Processes. In Carbonatites: Genises and Evolution, K. Bell, ed. (Unwin Hyman Ltd), pp. 89–104.

Tuckerman, M.E., and Martyna, G.J. (2000). Understanding Modern Molecular Dynamics: Techniques and Applications. The Journal of Physical Chemistry B *104*, 159–178.

VandeVondele, J., and Hutter, J. (2007). Gaussian basis sets for accurate calculations on molecular systems in gas and condensed phases. The Journal of Chemical Physics *127*, 114105.

VandeVondele, J., Krack, M., Mohamed, F., Parrinello, M., Chassaing, T., and Hutter, J. (2005). QUICKSTEP: Fast and accurate density functional calculations using a mixed Gaussian and plane waves approach. Computer Physics Communications *167*, 103–128.

Varshneya, A.K. (2013). Fundamentals of Inorganic Glasses (Elsevier).

Veksler, I.V., Petibon, C., Jenner, G.A., Dorfman, A.M., and Dingwell, D.B. (1998). Trace Element Partitioning in Immiscible Silicate–Carbonate Liquid Systems: an Initial Experimental Study Using a Centrifuge Autoclave. J. Petrology *39*, 2095–2104.

Veksler, I.V., Dorfman, A.M., Dulski, P., Kamenetsky, V.S., Danyushevsky, L.V., Jeffries, T., and Dingwell, D.B. (2012). Partitioning of elements between silicate melt and immiscible fluoride, chloride, carbonate, phosphate and sulfate melts, with implications to the origin of natrocarbonatite. Geochimica et Cosmochimica Acta *79*, 20–40.

Vessal, B., Greaves, G.N., Marten, P.T., Chadwick, A.V., Mole, R., and Houde-Walter, S. (1992). Cation microsegregation and ionic mobility in mixed alkali glasses. Nature *356*, 504–506.

Vuilleumier, R., Sator, N., and Guillot, B. (2009). Computer modeling of natural silicate melts: What can we learn from ab initio simulations. Geochimica et Cosmochimica Acta *73*, 6313–6339.

Vuilleumier, R., Seitsonen, A.P., Sator, N., and Guillot, B. (2015). Carbon dioxide in silicate melts at upper mantle conditions: Insights from atomistic simulations. Chemical Geology *418*, 77–88.

Wagner, J., Haigis, V., Künzel, D., and Jahn, S. (2017). Trace element partitioning between silicate melts – A molecular dynamics approach. Geochimica et Cosmochimica Acta *205*, 245–255.

Warren, B.E. (1937). X-Ray Determination of the Structure of Liquids and Glass. Journal of Applied Physics *8*, 645–654.

Wendlandt, R.F., and Harrison, W.J. (1979). Rare earth partitioning between immiscible carbonate and silicate liquids and CO_2 vapor: Results and implications for the formation of light rare earth-enriched rocks. Contr. Mineral. and Petrol. *69*, 409–419.

White, B.S., and Montana, A. (1990). The effect of H2O and CO2 on the viscosity of sanidine liquid at high pressures. Journal of Geophysical Research: Solid Earth *95*, 15683–15693.

Wilding, M.C., and Benmore, C.J. (2006). Structure of Glasses and Melts. In Neutron Scattering in Earth Sciences; Reviews in Mineralogy and Geochemistry 63, (Washington: Mineralogical Society of America), pp. 275–311.

Wilding, M., Badyal, Y., and Navrotsky, A. (2007). The local environment of trivalent lanthanide ions in sodium silicate glasses: A neutron diffraction study using isotopic substitution. Journal of Non-Crystalline Solids *353*, 4792–4800.

Williams, Q., and Knittle, E. (2003). Structural complexity in carbonatite liquid at high pressures. Geophys. Res. Lett. *30*, 1022.

Winterer, M. (1997). XAFS - A data analysis program for materials science. Journal de Physique IV *7*, 243–244.

Xiang, Y., and Du, J. (2011). Effect of strontium substitution on the structure of 45S5 bioglasses. Chemistry of Materials *23*, 2703–2717.

Xue, X., and Kanzaki, M. (2004). Dissolution mechanisms of water in depolymerized silicate melts: Constraints from 1H and 29Si NMR spectroscopy and ab initio calculations. Geochimica et Cosmochimica Acta *68*, 5027–5057.

Xue, X., and Kanzaki, M. (2006). Depolymerization effect of water in aluminosilicate glasses: Direct evidence from 1H-27Al heteronuclear correlation NMR. American Mineralogist *91*, 1922–1926.

Xue, X., and Kanzaki, M. (2008). Structure of hydrous aluminosilicate glasses along the diopside–anorthite join: A comprehensive one- and two-dimensional 1H and 27Al NMR study. Geochimica et Cosmochimica Acta *72*, 2331–2348.

Yamada, A., Wang, Y., Inoue, T., Yang, W., Park, C., Yu, T., and Shen, G. (2011). High-pressure x-ray diffraction studies on the structure of liquid silicate using a Paris-Edinburgh type large volume press. Review of Scientific Instruments *82*, 15103.

Yang, D.S., Fazzini, D.R., Morrison, T.I., Tröger, L., and Bunker, G. (1997). Modeling of pair distribution functions for XAFS in disordered systems. Journal of Non-Crystalline Solids *210*, 275–286.

Zen, E. (1988). Phase relations of peraluminous granitic rocks and their petrogenetic implications. Annual Review of Earth and Planetary Sciences *16*, 21–51.

Zhang, Y., and Zindler, A. (1993). Distribution and evolution of carbon and nitrogen in Earth. Earth and Planetary Science Letters *117*, 331–345.

Zhao, Y., Von Dreele, R.B., Weidner, D.J., and Schiferl, D. (1997). P-V-T Data of hexagonal boron nitride h BN and determination of pressure and temperature using thermoelastic equations of state of multiple phases. High Pressure Research *15*, 369–386.

Appendix

1 Determination of cell box sizes in molecular dynamics simulations

Cubic cell box length l was calculated using melt volumes V_{melt}: $l = \sqrt[3]{V_{melt}}$

With V_{melt} for *sSA00*, *sSA03* and *sNC10* according to (Sigurdsson et al., 2015):

$$V_{melt} = \sum X_i \left[\overline{V_{i,1673K}} + \left(\frac{\delta \overline{V_i}}{\delta T} \right)_P (T - 1673\ K) + \left(\frac{\delta \overline{V_i}}{\delta P} \right)_T P \right]$$

With X_i as the partial molar volume of the respective component i and:

Table A 1: Thermal expansions and compressibilities of components i.

i	$V_{i,1673K}$ [10^6 m^3/mol]	$(\delta V_i / \delta T)_P$ [10^9 m^3/mol*K]	$\delta V_i/\delta P$ [10^6 m^3/mol*GPa]
SiO_2	26.86	0.000	-1.890
Al_2O_3	37.42	0.000	-2.260
Na_2O	28.88	7.680	-2.400
CaO	16.53	3.740	0.340
CO_2	21	0.000	0.000

With V_{melt} for *CAR40* according to (Liu and Lange, 2003):

$$V_{melt} = \sum X_i \left[\overline{V_{i,1100}} + \left(\frac{\delta \overline{V_i}}{\delta T} \right)_P (T - 1100\ K) \right]$$

With X_i as the partial molar volume of the respective component i and:

Table A 2: Thermal expansions of components i.

i	$V_{i,1100K}$ [cm^3/mol]	$(\delta V_i / \delta T)_P$ [10^{-3} cm^3/mol*K]
Na_2CO_3	53.2	13.040
$CaCO_3$	40.2	7.150

2 Pair distribution functions of simulated Y glasses

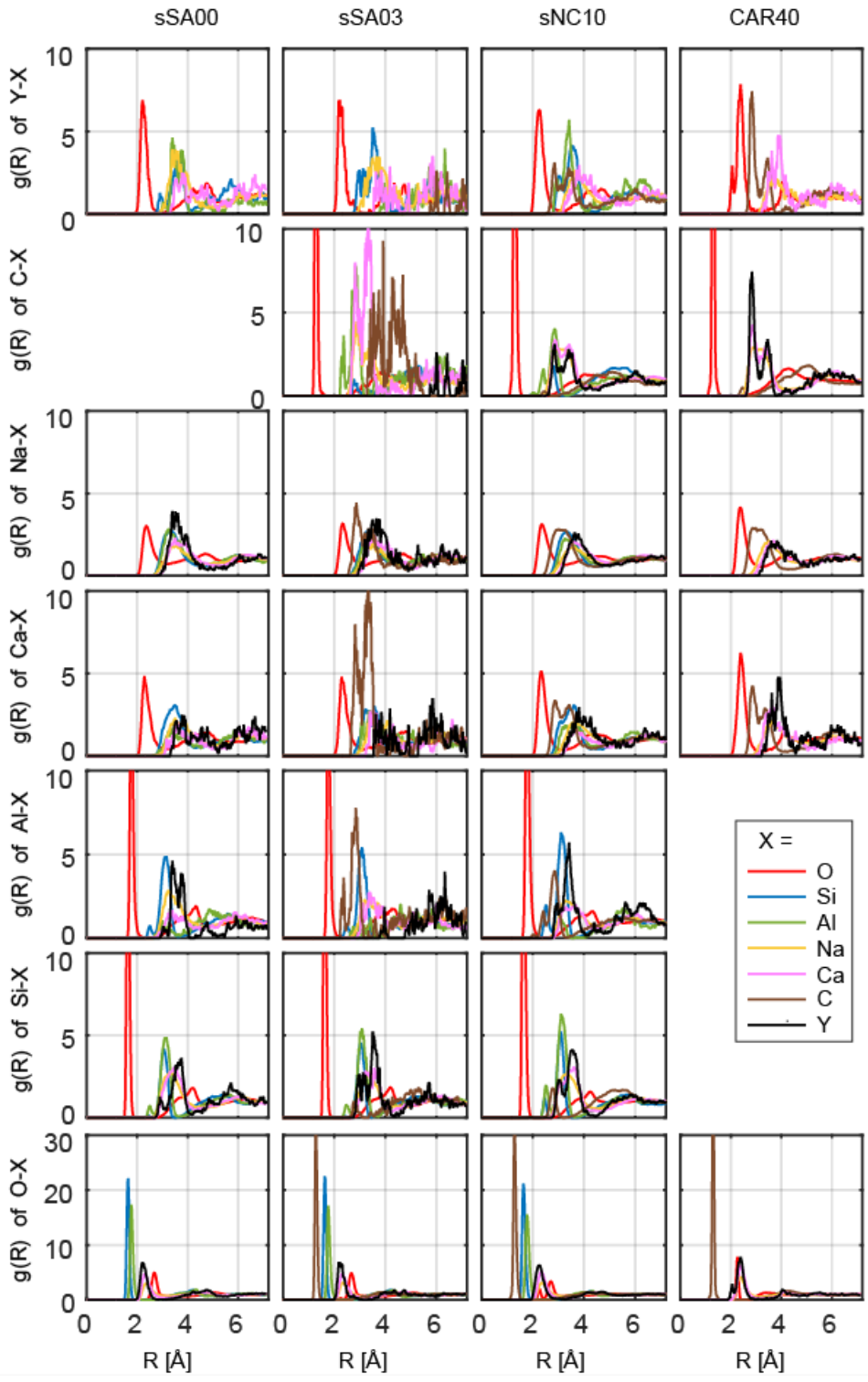

Figure A 1: Pair distribution functions of Y glasses from MD simulations.

3 Pair distribution functions of simulated Y melts

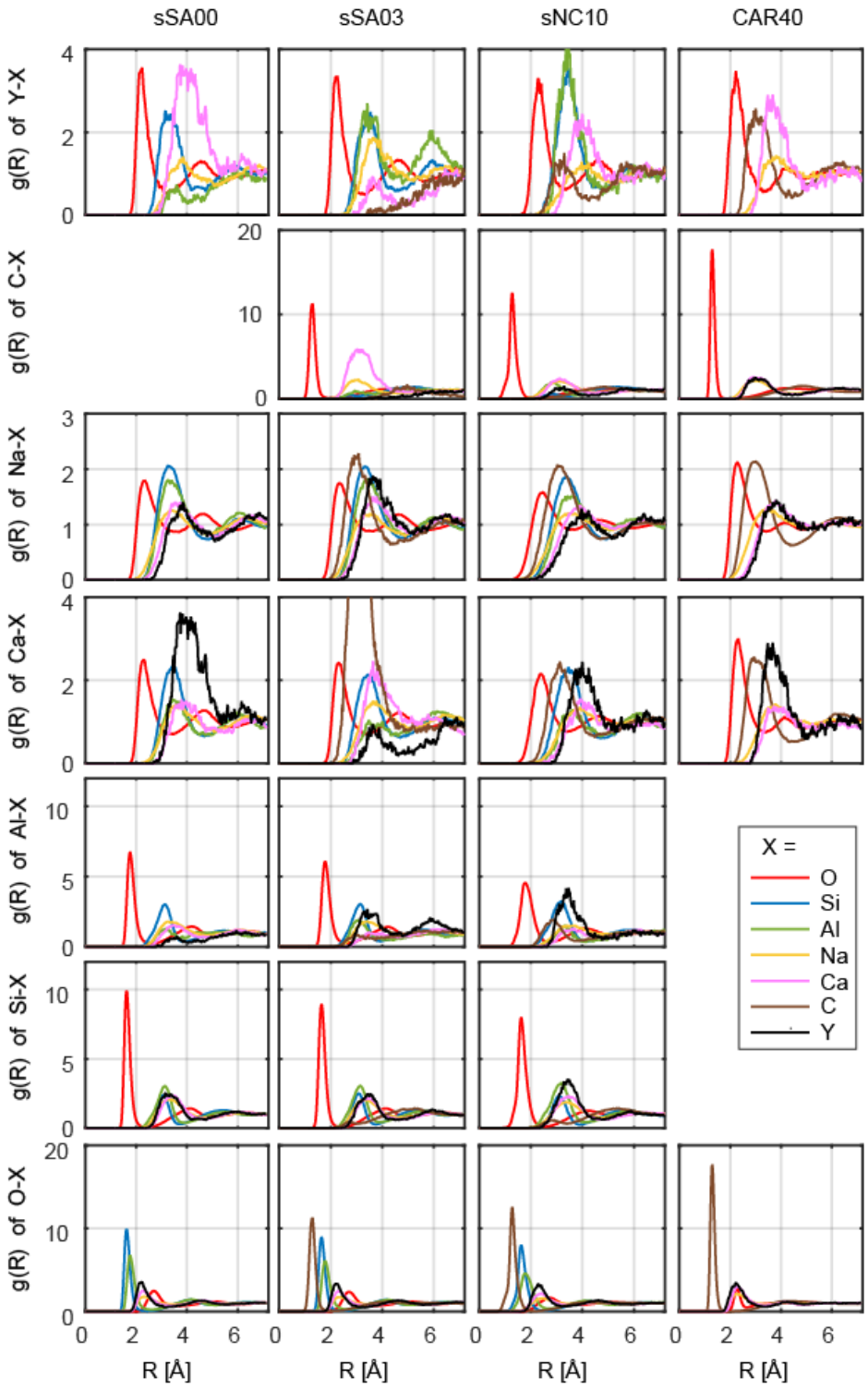

Figure A 2: Pair distribution functions of Y melts from MD simulations.

4 Pair distribution functions of simulated Sr melts

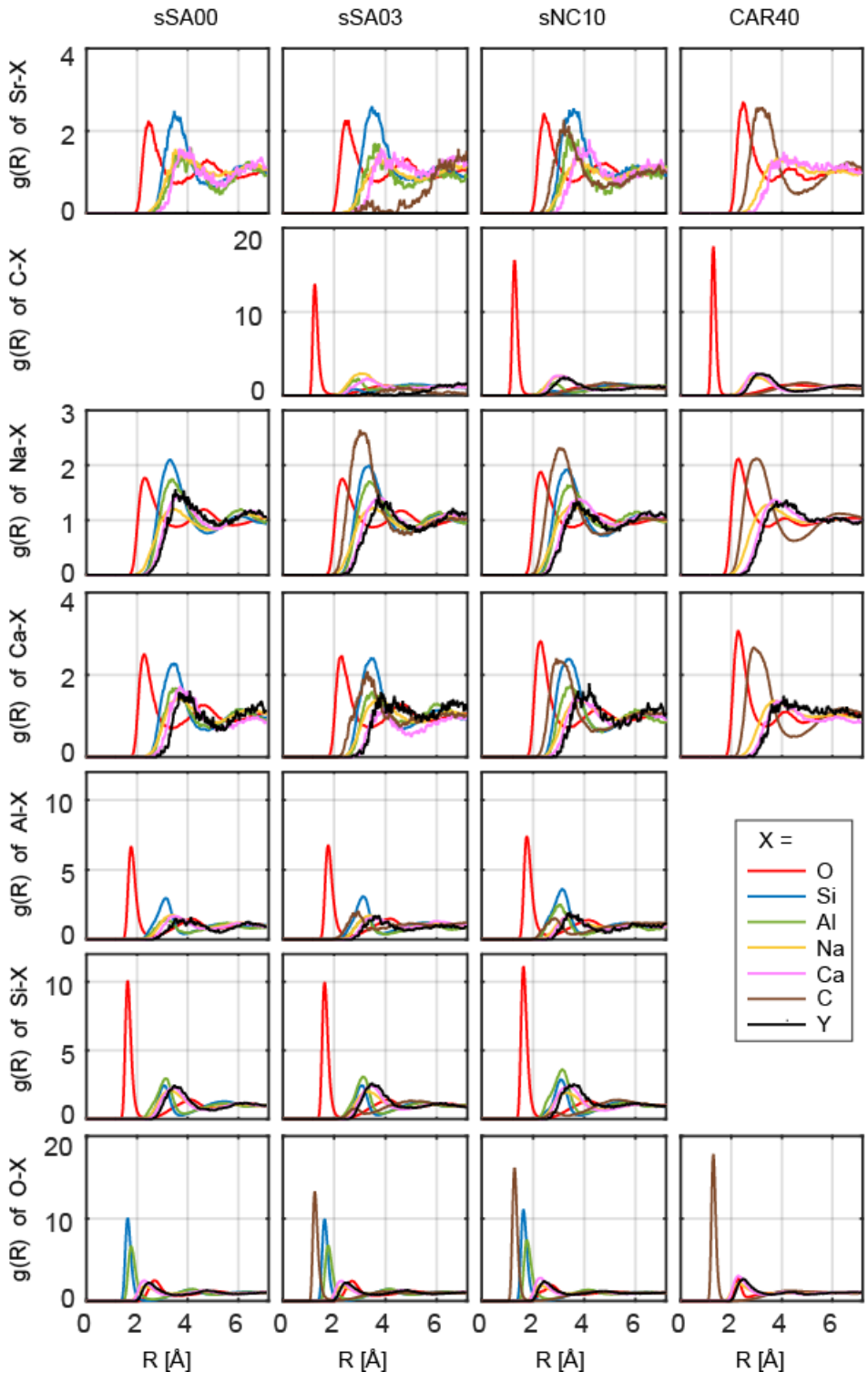

Figure A 3: Pair distribution functions of Sr melts from MD simulations.

5 Atom specific cut-off values used in the molecular dynamics simulations

Table A 3: Atom specific cut-off values r_{cut} for MD simulations.

[Å]	Y melt	Sr melt
r_{cut}^{SiO}	2.51	2.33
r_{cut}^{AlO}	2.70	2.65
r_{cut}^{NaO}	3.52	3.47
r_{cut}^{CaO}	3.37	3.38
r_{cut}^{CO}	1.96	2.01
$r_{cut}^{Y/SrO}$	3.31	3.57

6 Second shell environment of Y, Sr and C in simulated melts

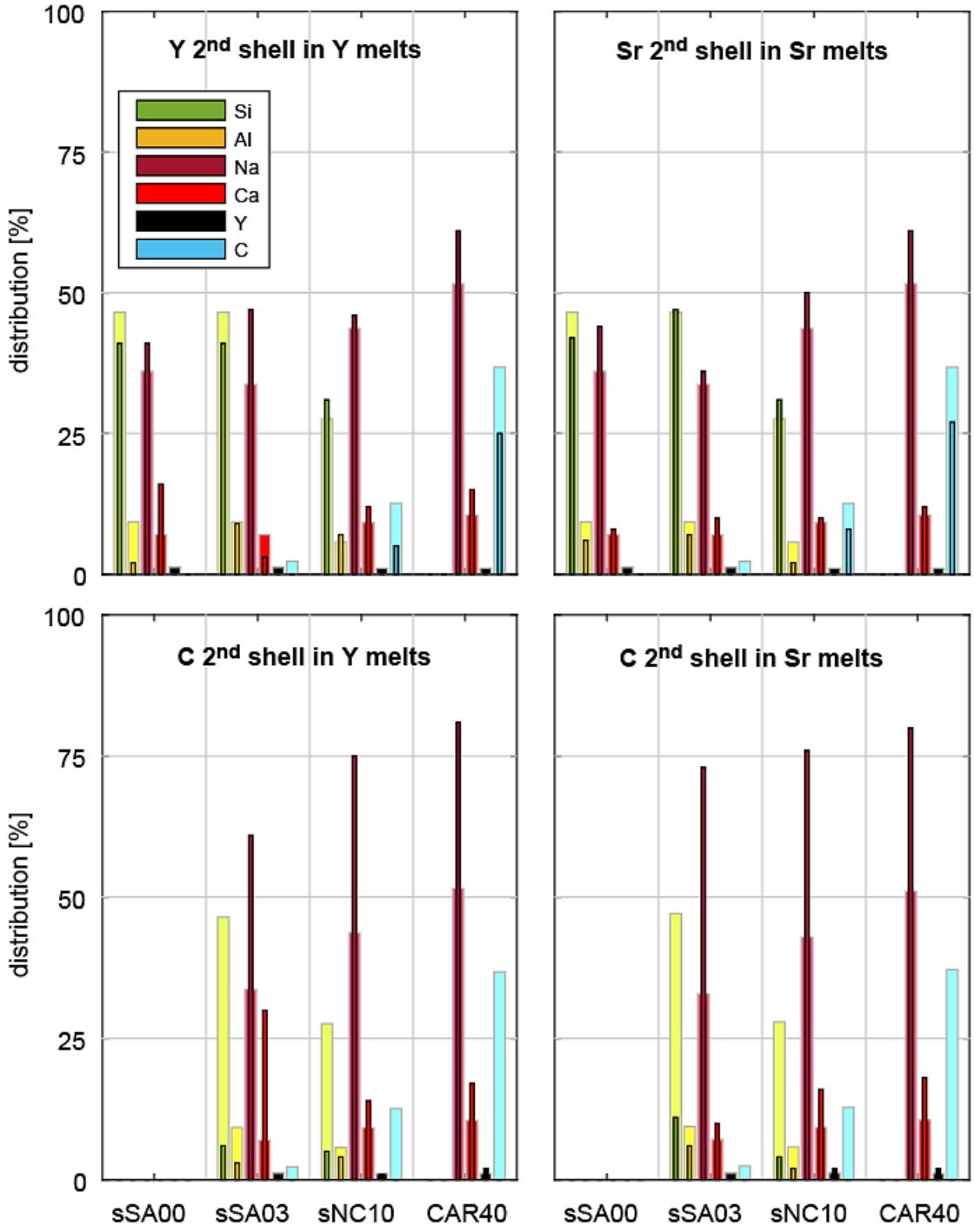

Figure A 4: Second shell environment of Y, Sr and C in glasses and melts in simulations. Dark narrow bars indicate the fraction of cations found in the 2nd shell around Y/Sr or C. Bright wide bars indicate the shares of cations in bulk composition of the respective sample.

7 Oxygen species in simulated melts and glasses

Table A 4: Oxygen species in melts and glasses of MD simulations.
For each simulation run are indicated the fractions of: free oxygen (FO), which do not interact with any network former (T); non-bridging oxygens (NBO), which belong to the coordination environment of either an Si (NBO_{Si}) or an $^{[4]}Al$ (NBO_{Al}) as network former; bridging oxygen (BO), which fulfill a bridging function between two network formers, either in between two Si ($BO_{Si\text{-}Si}$), one Si and one $^{[4]}Al$ ($BO_{Si\text{-}Al}$) or two $^{[4]}Al$ ($BO_{Al\text{-}Al}$); tri-cluster oxygen (TO) which belong to the coordination environment of three network formers. Additionally is given the structural parameter NBO/T a degree for the melt's polymerization.

	[%]	**FO**	**NBO**	NBO_{Si}		NBO_{Al}		**BO**	$BO_{Si\text{-}Si}$		$BO_{Si\text{-}Al}$		$BO_{Al\text{-}Al}$		**TO**	NBO/T
				tot%	*NBO%*	tot%	*NBO%*		tot%	*BO%*	tot%	*BO%*	tot%	*BO%*		
Y glasses	*sSA00*	**0.2**	**36.9**	35.5	*96.3*	1.4	*3.7*	**62.7**	40.8	*65.1*	21.6	*34.5*	0.2	*0.3*	**0.3**	*0.91*
	sSA03	**4.0**	**35.4**	33.7	*95.2*	1.7	*4.8*	**60.2**	41.5	*68.9*	18.6	*30.9*	0.1	*0.2*	**0.4**	*0.92*
	sNC10	**25.3**	**44.0**	40.0	*91.0*	3.9	*9.0*	**30.7**	20.0	*65.1*	10.5	*34.3*	0.2	*0.6*	**0.0**	*1.69*
Y melts	*sSA00*	**0.4**	**41.3**	40.2	*97.4*	1.1	*2.6*	**56.9**	41.0	*72.0*	15.5	*27.3*	0.4	*0.7*	**1.4**	*1.14*
	sSA03	**4.4**	**39.5**	38.7	*97.9*	0.8	*2.1*	**55.4**	40.9	*73.9*	14.1	*25.5*	0.3	*0.6*	**0.7**	*1.14*
	sNC10	**25.7**	**47.3**	44.6	*94.2*	2.7	*5.8*	**26.6**	18.6	*69.8*	7.9	*29.5*	0.2	*0.7*	**0.4**	*2.05*
Sr melts	*sSA00*	**0.2**	**42.1**	41.3	*98.2*	0.8	*1.8*	**56.8**	41.1	*72.5*	15.1	*26.6*	0.5	*0.9*	**0.9**	1.14
	sSA03	**3.6**	**38.2**	37.3	*97.5*	0.9	*2.5*	**57.3**	41.1	*71.7*	15.6	*27.3*	0.6	*1.0*	**0.9**	1.06
	sNC10	**27.2**	**43.2**	41.2	*95.4*	2.0	*4.6*	**29.2**	19.4	*66.5*	9.5	*32.5*	0.3	*1.0*	**0.5**	1.81

8 Coordination numbers and bond lengths in simulated melts and glasses

Table A 5: Coordination numbers and bond length in Y and Sr silicate to carbonate melts in MD simulations.

	Y glasses			Y melts					Sr melts			
	sSA00	*sSA03*	*sNC10*	*sSA00*	*sSA03*	*sNC10*	*CAR40*		*sSA00*	*sSA03*	*sNC10*	*CAR40*
Coordination number N												
Y-O	5.91	6.29	6.07	6.69	6.53	6.51	6.95	Sr-O	7.53	7.92	6.94	7.96
Na-O	6.96	6.77	6.20	7.11	7.18	6.38	7.04	Na-O	6.81	6.80	6.05	6.74
Ca-O	6.30	6.52	6.02	6.59	6.66	6.17	6.96	Ca-O	6.56	6.62	6.19	7.07
Al-O	4.15	4.24	4.21	4.34	4.46	4.38	-	Al-O	4.35	4.30	4.28	-
Si-O	4.01	4.01	4.00	4.05	4.06	3.99	-	Si-O	4.01	4.01	3.96	-
C-O	-	3.00	2.96	-	2.82	2.92	2.98	C-O	-	2.86	2.87	3.00
Average bond length $\bar{r}$												
Y-O	2.26	2.29	2.28	2.50	2.50	2.55	2.51	Sr-O	2.83	2.85	2.82	2.82
Na-O	2.48	2.46	2.48	2.78	2.79	2.79	2.75	Na-O	2.76	2.76	2.74	2.71
Ca-O	2.38	2.40	2.39	2.63	2.64	2.65	2.61	Ca-O	2.63	2.64	2.61	2.62
Al-O	1.78	1.79	1.79	1.90	1.92	1.96	-	Al-O	1.90	1.89	1.91	-
Si-O	1.64	1.65	1.65	1.70	1.71	1.73	-	Si-O	1.70	1.70	1.70	-
C-O	-	1.30	1.30	-	1.33	1.34	1.33	C-O	-	1.33	1.33	1.33
Most probable bond length $\hat{r}$												
Y-O	2.23	2.24	2.25	2.22	2.22	2.33	2.22	Sr-O	2.49	2.49	2.44	2.49
Na-O	2.37	2.34	2.35	2.33	2.33	2.41	2.28	Na-O	2.33	2.33	2.29	2.29
Ca-O	2.31	2.31	2.33	2.30	2.31	2.40	2.31	Ca-O	2.28	2.28	2.29	2.28
Al-O	1.77	1.78	1.78	1.77	1.78	1.78	-	Al-O	1.76	1.77	1.76	-
Si-O	1.64	1.64	1.64	1.62	1.63	1.62	-	Si-O	1.63	1.63	1.63	-
C-O	-	1.29	1.29	-	1.28	1.28	1.29	C-O	-	1.25	1.28	1.29

9 Distribution of coordination numbers in simulated melts

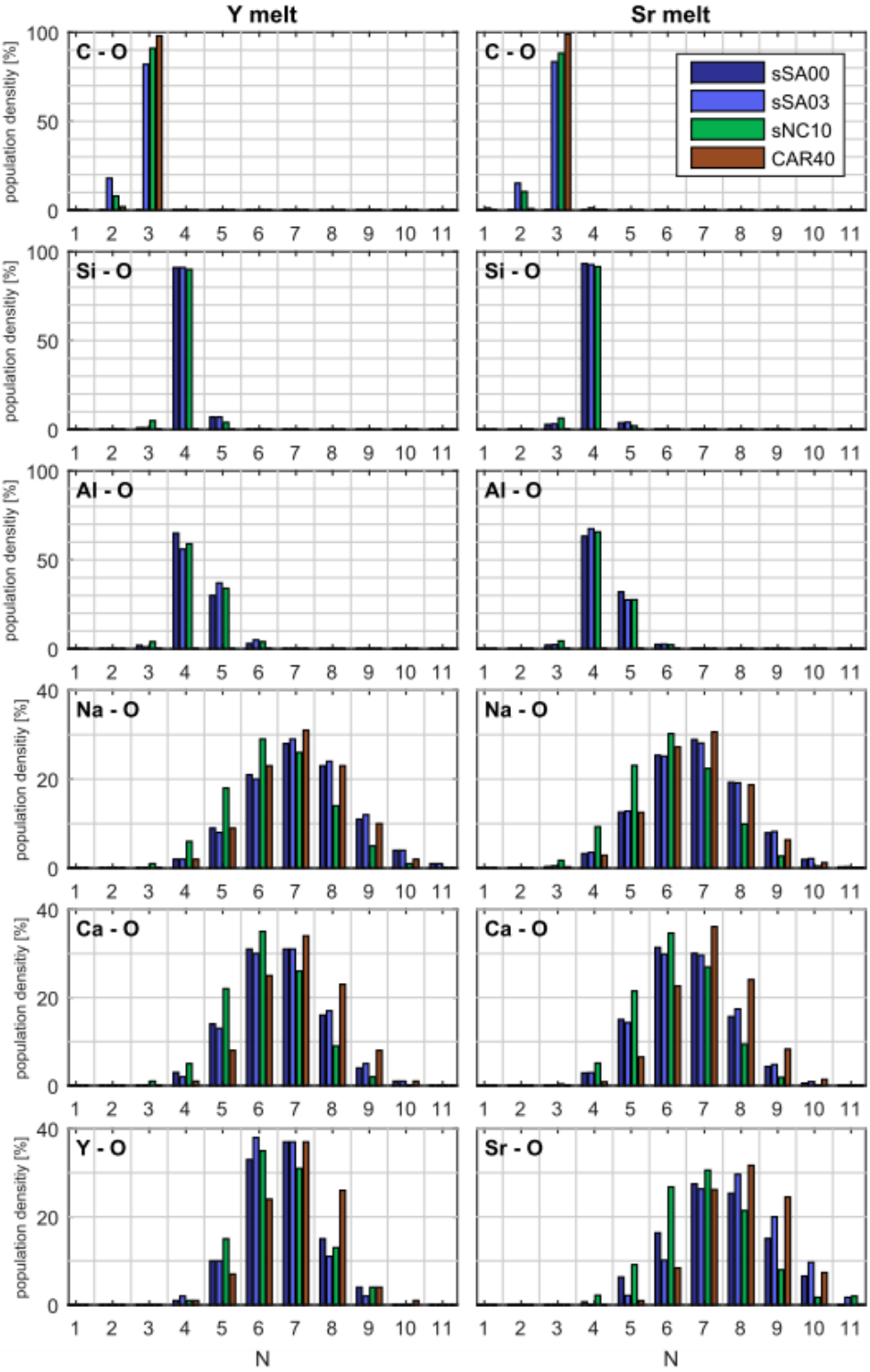

Figure A 5: Coordination number distribution in melts in MD simulations.

10 Local environment of Y in simulated glasses

Table A 6: Y-oxygen environment of glasses in MD simulations.
For each simulation run are indicated the fractions in % of: free oxygen (FO), non-bridging oxygens (NBO), which coordinate either an Si (NBO_{Si}) or an $^{[4]}Al$ (NBO_{Al}); bridging oxygen (BO), either in between two Si ($BO_{Si\text{-}Si}$), one Si and one $^{[4]}Al$ ($BO_{Si\text{-}Al}$) or two $^{[4]}Al$ ($BO_{Al\text{-}Al}$); tri-cluster oxygen (TO) which are shared by three network formers.

		Local structure of Y in glasses Probabilities [%]									
	N	**sum**	FO	NBO	NBO_{Si}	NBO_{Al}	BO	$BO_{Si\text{-}Si}$	$BO_{Si\text{-}Al}$	$BO_{Al\text{-}Al}$	TO
sSA00	4	**3.4**	0.5	2.9	*2.5*	*0.4*	0.0	*0.0*	*0.0*		
	5	**18.1**	0.2	17.2	*13.9*	*3.4*	0.8	*0.8*	*0.0*		
	6	**63.4**	0.6	60.0	*51.0*	*8.9*	2.8	*2.2*	*0.6*		
	7	**14.6**	0.4	12.4	*10.8*	*1.7*	1.8	*1.7*	*0.1*		
	8	**0.5**	0.0	0.3	*0.3*	*0.1*	0.2	*0.2*	*0.0*		
	9										
	10										
	11										
	sum		**1.6**	**92.8**	***78.5***	***14.4***	**5.5**	***4.8***	***0.7***		
sSA03	4										
	5	**6.8**	0.0	6.8	*6.8*	*0.0*	0.0	*0.0*	*0.0*		
	6	**57.5**	0.0	50.2	*50.2*	*0.0*	7.3	*7.3*	*0.0*		
	7	**35.7**	0.0	24.7	*24.7*	*0.0*	11.0	*9.8*	*1.2*		
	8										
	9										
	10										
	11										
	sum		**0.0**	**81.7**	***81.7***	***0.0***	**18.3**	***17.1***	***1.2***		
sNC10	4	**0.1**	0.0	0.1	*0.1*	*0.0*	0.0	*0.0*	*0.0*		
	5	**15.8**	3.2	12.5	*9.9*	*2.7*	0.1	*0.1*	*0.0*		
	6	**61.2**	19.4	39.3	*34.4*	*4.9*	2.5	*1.9*	*0.6*		
	7	**22.8**	5.7	14.5	*12.8*	*1.8*	2.6	*1.4*	*1.2*		
	8	**0.2**	0.0	0.1	*0.1*	*0.0*	0.0	*0.0*	*0.0*		
	9										
	10										
	11										
	sum		**28.3**	**66.6**	***57.2***	***9.3***	**5.1**	***3.3***	***1.8***		

11 Local environment of Y in simulated melts

Table A 7: Y-oxygen environment in melts in MD simulations.
For each simulation run are indicated the fractions in % of: free oxygen (FO), non-bridging oxygens (NBO), which coordinate either an Si (NBO_{Si}) or an $^{[4]}Al$ (NBO_{Al}); bridging oxygen (BO), either in between two Si ($BO_{Si\text{-}Si}$), one Si and one $^{[4]}Al$ ($BO_{Si\text{-}Al}$) or two $^{[4]}Al$ ($BO_{Al\text{-}Al}$); tri-cluster oxygen (TO) which are shared by three network formers.

			Local structure of Y in melts								
	N		Probabilities [%]								
		sum	FO	NBO	*NBO_{Si}*	*NBO_{Al}*	BO	*$BO_{Si\text{-}Si}$*	*$BO_{Si\text{-}Al}$*	*$BO_{Al\text{-}Al}$*	TO
sSA00	4	**0.8**	0.0	0.7	*0.7*	*0.0*	0.0	*0.0*	*0.0*		0.0
	5	**10.0**	0.2	8.9	*8.3*	*0.6*	0.9	*0.8*	*0.2*		0.0
	6	**33.0**	0.2	28.0	*27.1*	*0.8*	4.7	*4.0*	*0.8*		0.1
	7	**37.2**	0.1	29.0	*28.5*	*0.5*	8.0	*7.3*	*0.8*		0.1
	8	**14.5**	0.0	10.4	*10.3*	*0.1*	4.1	*3.8*	*0.3*		0.1
	9	**4.1**	0.0	2.7	*2.6*	*0.0*	1.4	*1.3*	*0.1*		0.0
	10										
	11										
	sum		**0.5**	**79.6**	***77.6***	***2.0***	**19.3**	***17.1***	***2.2***		**0.3**
sSA03	4	**1.6**	0.0	1.5	*1.5*	*0.0*	0.1	*0.1*	*0.0*	*0.0*	0.0
	5	**10.6**	0.2	9.0	*8.6*	*0.5*	1.3	*0.8*	*0.5*	*0.0*	0.0
	6	**38.3**	0.5	30.2	*29.1*	*1.2*	7.5	*4.5*	*3.0*	*0.0*	0.1
	7	**36.2**	0.6	26.0	*24.9*	*1.1*	9.5	*6.2*	*3.2*	*0.0*	0.2
	8	**10.8**	0.2	7.4	*7.1*	*0.3*	3.1	*2.1*	*1.0*	*0.0*	0.1
	9	**2.5**	0.1	1.5	*1.5*	*0.1*	0.8	*0.6*	*0.2*	*0.0*	0.0
	10										
	11										
	sum		**1.6**	**75.7**	***72.5***	***3.2***	**22.4**	***14.3***	***8.0***	***0.1***	**0.3**
sNC10	4	**1.6**	0.5	0.9	*0.8*	*0.1*	0.1	*0.1*	*0.0*		0.0
	5	**15.4**	3.4	10.4	*9.3*	*1.1*	1.5	*0.7*	*0.8*		0.0
	6	**35.2**	5.9	24.1	*21.1*	*3.0*	5.2	*2.9*	*2.3*		0.0
	7	**31.3**	4.6	20.1	*18.4*	*1.7*	6.6	*4.2*	*2.5*		0.0
	8	**12.1**	1.3	7.7	*7.1*	*0.6*	3.1	*2.1*	*1.0*		0.0
	9	**4.0**	0.4	2.3	*2.2*	*0.1*	1.2	*0.9*	*0.3*		0.0
	10	**0.4**	0.0	0.3	*0.3*	*0.0*	0.1	*0.1*	*0.0*		0.0
	11										
	sum		**16.2**	**65.8**	***59.1***	***6.7***	**18.0**	***11.0***	***7.0***		**0.1**
CAR40	4	**0.6**	0.6								
	5	**8.1**	8.1								
	6	**25.2**	25.2								
	7	**34.9**	34.9								
	8	**25.6**	25.6								
	9	**5.3**	5.3								
	10	**0.6**	0.6								
	11										
	sum		**100.0**								

12 Local environment of Sr in simulated melts

Table A 8: Sr-oxygen environment in melts in MD simulations.
For each simulation run are indicated the fractions in % of: free oxygen (FO), non-bridging oxygens (NBO), which coordinate either an Si (NBO_{Si}) or an $^{[4]}Al$ (NBO_{Al}); bridging oxygen (BO), either in between two Si ($BO_{Si\text{-}Si}$), one Si and one $^{[4]}Al$ ($BO_{Si\text{-}Al}$) or two $^{[4]}Al$ ($BO_{Al\text{-}Al}$); tri-cluster oxygen (TO) which are shared by three network formers.

	N	Local structure of Sr in melts Probabilities [%]									
		sum	FO	NBO	*NBO_{Si}*	*NBO_{Al}*	BO	*$BO_{Si\text{-}Si}$*	*$BO_{Si\text{-}Al}$*	*$BO_{Al\text{-}Al}$*	TO
sSA00	4	**0.7**	0.0	0.7	*0.7*	*0.0*	0.1	*0.0*	*0.0*	*0.0*	0.0
	5	**6.5**	0.0	5.0	*5.0*	*0.0*	1.5	*0.9*	*0.6*	*0.0*	0.0
	6	**16.8**	0.0	12.1	*12.1*	*0.0*	4.6	*3.1*	*1.6*	*0.0*	0.0
	7	**27.8**	0.0	18.0	*17.9*	*0.1*	9.7	*6.8*	*2.9*	*0.0*	0.0
	8	**25.0**	0.0	14.9	*14.9*	*0.0*	10.0	*7.7*	*2.3*	*0.0*	0.0
	9	**14.9**	0.0	8.1	*8.0*	*0.1*	6.7	*5.5*	*1.1*	*0.1*	0.0
	10	**6.3**	0.0	3.1	*3.0*	*0.1*	3.2	*2.6*	*0.5*	*0.1*	0.0
	11	**1.7**	0.0	0.8	*0.8*	*0.0*	0.8	*0.7*	*0.1*	*0.0*	0.0
	sum		**0.1**	**62.8**	***62.4***	***0.3***	**36.6**	***27.3***	***9.2***	***0.1***	**0.1**
sSA03	4										
	5	**2.1**	0.0	1.4	*1.4*	*0.0*	0.7	*0.4*	*0.3*	*0.0*	0.0
	6	**10.3**	0.0	6.5	*6.5*	*0.0*	3.8	*2.4*	*1.4*	*0.0*	0.0
	7	**27.1**	0.0	15.6	*15.6*	*0.0*	11.5	*7.9*	*3.6*	*0.0*	0.0
	8	**29.2**	0.0	15.8	*15.8*	*0.0*	13.4	*9.6*	*3.7*	*0.1*	0.0
	9	**19.7**	0.0	10.0	*10.0*	*0.0*	9.7	*7.3*	*2.3*	*0.0*	0.1
	10	**9.8**	0.0	4.8	*4.8*	*0.0*	4.9	*3.7*	*1.1*	*0.1*	0.0
	11	**1.7**	0.0	0.8	*0.8*	*0.0*	0.9	*0.7*	*0.2*	*0.0*	0.0
	sum		**0.0**	**54.9**	***54.9***	***0.0***	**44.8**	***32.0***	***12.6***	***0.2***	**0.2**
sNC10	4	**2.4**	0.5	1.8	*1.8*	*0.0*	0.1	*0.1*	*0.0*		0.0
	5	**9.3**	2.1	6.2	*6.2*	*0.0*	1.0	*0.8*	*0.1*		0.0
	6	**27.0**	6.7	16.3	*16.3*	*0.0*	4.0	*3.4*	*0.6*		0.0
	7	**30.1**	6.5	17.4	*17.4*	*0.0*	6.1	*5.1*	*1.1*		0.0
	8	**21.6**	4.4	11.8	*11.7*	*0.0*	5.5	*4.5*	*1.0*		0.0
	9	**7.5**	1.6	4.1	*4.1*	*0.0*	1.8	*1.5*	*0.3*		0.0
	10	**1.7**	0.3	0.8	*0.8*	*0.0*	0.6	*0.5*	*0.0*		0.0
	11	**0.2**	0.0	0.1	*0.1*	*0.0*	0.1	*0.1*	*0.0*		0.0
	sum		**22.2**	**58.4**	***58.4***	***0.1***	**19.2**	***16.0***	***3.2***		**0.1**
CAR40	4										
	5	**0.9**	0.9								
	6	**8.8**	8.8								
	7	**26.1**	26.1								
	8	**32.4**	32.4								
	9	**23.8**	23.8								
	10	**7.1**	7.1								
	11	**1.0**	1.0								
	sum		**100.0**								

13 C-oxygen environment in simulated melts and glasses

Table A 9: C oxygen environment in melts and glasses in MD simulations.
For each simulation run is indicated the fractions in % of: CO_2 dissolved as CO-, CO_2-, CO_3- or CO_4-group. Furthermore, FC indicates free carbonates, T–CO_3 indicates non-bridging carbonates (Si–CO_3 or $^{[4]}$Al–CO_3: either sharing one non-bridging oxygen with one Si or $^{[4]}$Al, $^{T}_{T}{=}\,CO_3$: sharing two oxygens with one Si or $^{[4]}$Al, $^{T}_{T}{-}CO_3$: associated with a bridging oxygen), T–CO_3–T indicates bridging carbonates between two respective network formers and $^{T}_{T}{-}CO_3^{-T}$ indicate bridging carbonates between three network formers.

	[%]	**CO**	**CO_2**			**CO_3**												**CO_4**
				T–CO_2	FC		T–CO_3–T	Si–CO_3–Si	Si–CO_3–$^{[4]}$Al	$^{[4]}$Al–CO_3–$^{[4]}$Al	$^{T}_{T}{-}CO_3^{-T}$	T–CO_3	Si–CO_3	$^{[4]}$Al–CO_3	$^{T}_{T}{-}CO_3$	$^{T}_{T}{=}\,CO_3$	FC	
Y glass	*sSA03*	**0.0**	**0.0**	0.0	0.0	**100.0**	8.3	*4.2*	*4.2*	*0.0*	*0.0*	54.0	*16.7*	*37.3*	*0.0*	*0.0*	*37.7*	**0.0**
	sNC10	**0.6**	**2.4**	0.0	2.4	**97.0**	6.6	*3.2*	*2.6*	*0.8*	*0.0*	43.9	*29.6*	*14.2*	*0.0*	*0.1*	*46.5*	**0.0**
Y melt	*sSA03*	**0.0**	**18.1**	1.2	16.9	**81.5**	3.2	*1.5*	*1.7*	*0.0*	*0.0*	31.9	*27.0*	*2.7*	*0.9*	*1.4*	*46.4*	**0.0**
	sNC10	**0.0**	**8.2**	0.3	7.9	**91.0**	3.2	*1.9*	*0.9*	*0.5*	*0.0*	40.1	*25.6*	*12.4*	*0.3*	*1.7*	*47.7*	**0.3**
	CAR40	**0.0**	**2.1**	0.0	2.1	**97.8**	0.0	*0.0*	*0.0*	*0.0*	*0.0*	0.0	*0.0*	*0.0*	*0.0*	*0.0*	*97.8*	**0.1**
Sr melt	*sSA03*	**0.0**	**15.2**	0.3	14.9	**83.4**	8.7	*3.3*	*2.8*	*2.0*	*0.6*	61.3	*47.7*	*11.1*	*0.7*	*1.8*	*13.4*	**1.2**
	sNC10	**1.2**	**10.4**	0.4	10.0	**87.9**	1.6	*1.0*	*0.6*	*0.0*	*0.0*	26.7	*19.6*	*6.5*	*0.2*	*0.3*	*59.6*	**0.1**
	CAR40	**0.0**	**0.9**	0.0	0.9	**99.0**	0.0	*0.0*	*0.0*	*0.0*	*0.0*	0.0	*0.0*	*0.0*	*0.0*	*0.0*	*99.0*	**0.1**